Modeling Forest Canopy Distribution from Ground-based Laser Scanner Data

By

Jason G. Henning

Dissertation submitted to the faculty of the
Virginia Polytechnic Institute and State University
in partial fulfillment of the requirements for the degree of

Doctor of Philosophy
In
Forestry

Dr. Philip J. Radtke, Chariman
Dr. Harold E. Burkhart
Dr. Stephen P. Prisley
Dr. Marion R. Reynolds Jr.

July 25, 2005
Blacksburg, VA

Keywords: range image, registration, lidar, canopy structure, stem map, terrestrial laser scanning

Modeling Forest Canopy Distribution from Ground-based Laser Scanner Data

By

Jason G. Henning

Abstract

A commercially available, tripod mounted, ground-based laser scanner was used to assess forest canopies and measure individual tree parameters. The instrument is comparable to scanning airborne light detection and ranging (lidar) technology but gathers data at higher resolution over a more limited scale. The raw data consist of a series of range measurements to visible surfaces taken at known angles relative to the scanner. Data were translated into three dimensional (3D) point clouds with points corresponding to surfaces visible from the scanner vantage point. A 20 m × 40 m permanent plot located in upland deciduous forest at Coweeta, NC was assessed with 41 and 45 scans gathered during periods of leaf-on and leaf-off, respectively. Data management and summary needs were addressed, focusing on the development of registration methods to align point clouds collected from multiple vantage points and minimize the volume of the plot canopy occluded from the scanner's view. Automated algorithms were developed to extract points representing tree bole surfaces, bole centers and ground surfaces. The extracted points served as the control surfaces necessary for registration. Occlusion was minimized by combining aligned point clouds captured from multiple vantage points with 0.1% and 0.34% of the volume scanned being occluded from view under leaf-off and leaf-on conditions, respectively. The point cloud data were summarized to estimate individual tree parameters including diameter at breast height (dbh), upper stem diameters, branch heights and XY positions of trees on the plot. Estimated tree positions were, on average, within 0.4 m of tree positions measured independently on the plot. Canopy height models, digital terrain models and 3D maps of the density of canopy surfaces were created using aligned point cloud data. Finally spatially explicit models of the horizontal and vertical distribution of plant area index (PAI) and leaf area index (LAI) were generated as examples of useful data summaries that cannot be practically collected using existing methods.

Acknowledgements

First, I would like to thank my advisor, Dr. Phil Radtke, who provided me with the freedom to explore my interests and guidance that ensured a successful end to my endeavors. I would also like to thank the rest of my committee, including Dr. Harold Burkhart, Dr. Stephen Prisley and Dr. Marion Reynolds, whose patient and thoughtful consideration of my work was greatly appreciated.

A special thanks goes to my fellow graduate students, especially to those chronically misunderstood biometricians who were uniquely qualified consultants and commiserators. I would also like to acknowledge the larger Virginia Tech community, and the faculty and staff of the Departments of Forestry, for making my experience here as rewarding and enjoyable as I could have hoped for.

To my entire family, and especially my parents, Pat and Greg, and my brother Jess, your unwavering support and encouragement throughout my academic career has always amazed me and has been the foundation of much of my success. To the friends I have made here in Blacksburg and those I grew up with in King of Prussia, the distractions and humor you provided kept me sane. Lastly, to Katie Keane, who has shared in all the highs and lows of this experience, you provided me with more support than I ever could have asked for and I cannot wait to do the same for you.

Table of Contents

List of Figures

List of Tables

1 Introduction

Assessing variation in tree growth and determining the factors that affect a tree's growth have been subjects of great interest for those who study forests and forest ecosystems. To this end countless empirical and process-based models have been developed (Korzukhin et al. 1996). Examples range in complexity from simple yield tables to more involved statistical regression models to computer models of mechanistic or physiological processes. Regardless of their complexity, any such models may be intended to explain relationships between observable predictors and the ways that trees or forests grow in relation to those predictors. Many forest growth models have adopted increasingly complex formulations or algorithmic structures, to address increasingly complex research questions. These approaches are made possible by the increased availability of tools for formulating complex models. For example, recent efforts focused on characterizing the spatial heterogeneity of resources and the influence of this heterogeneity on tree growth (Brunner 1998, Canham et al. 1994). Light is often considered a key resource for tree growth and has been shown to be highly variable in both space and time (Canham et al. 1994). A number of models incorporate this heterogeneity either empirically, through competition indexes and gap light indexes, or using mechanistic approaches to represent light interception and utilization in forest canopies (Dai 1996, Brunner 1998).

1.1 Canopy Structure and the Light Environment

Significant efforts aimed at assessing the spatial and temporal heterogeneity of light resources have involved the characterization of canopy gaps or openings (Canham et al. 1994). Canopy gaps are widely considered the key means by which light reaches the forest understory and are therefore considered key controls of species diversity and seedling growth (Canham et al. 1994, Dai 1996 and Pacala et al. 1994). A number of studies have found that even small canopy openings and sunflecks are key elements of tree growth (Canham et al. 1990, Chazdon and Pearcy 1991).

Various gap light indexes (GLI) have been developed to assess available light related to openings in forest canopies (Comeau et al. 1998, Dai 1996, Canham et al. 1994). These indexes generally depend on analysis of fixed-location, instantaneous measures from quantum sensors or

analysis of hemispherical photographs (Comeau et al. 1998, Wang et al. 2000). The use of quantum sensors is often limited by the fact that they provide one-time instantaneous measures and, in general, provide no information about the spatial or temporal distribution of available light (Stadt et al. 1997, Gendron et al. 1998). Hemispherical photographs have been regarded as "one of the most effective methods for estimating long-term average light levels" (Gendron et al. 1998); however, GLIs derived from hemispherical photographs generally make use of simplifying assumptions about the spatial distributions of leaves in forest canopies in order to translate the two-dimensional (2D) photographic representations into the three-dimensional (3D) domain of canopy models. A number of authors have observed inaccuracies in GLI estimates derived from hemispherical photography, likely due to violations of their simplifying assumptions about how foliage is distributed throughout the canopy. Inaccuracies notwithstanding, point measures of canopy light conditions or 2D measures of foliage distributions are incomplete in their representation of the spatial heterogeneity of forest canopies (Chen et al. 1991, Chen and Cihlar 1995, Parker et al. 2002, Smith et al. 1993).

A number of studies have found that the shape and relative location of gaps in the forest canopy can have a major impact on how much light reaches any one tree (Urban et al. 1991, Weishampel and Urban 1996). Canham (1988) points out that, "there is substantial spatial variation in understory light levels as a result of the geometry of shading by canopy trees adjacent to a gap, so that gap size is inadequate as an index of the amount of light received by plants at different locations in or around a gap." Even very small canopy openings and difficult-to-recognize canopy light pathways can be important to measure and assess spatially (Chazdon and Pearcy 1991). In one study Canham et al. (1990) found that sunflecks—small ephemeral light patches lasting only minutes—contribute 36%-68% of photosynthetically active radiation for understory trees and plants.

The heterogeneous nature of light distribution in the forest is linked to differences in growth of individual trees. As such, capturing this spatial variability has been a goal of a number of researchers (Wang et al. 2000, Comeau et al. 1993). Gap light indexes (GLIs) were created to address the spatial heterogeneity of light and its influence on individual trees or locations in the forest. GLIs focus on canopy gaps as the key cause of heterogeneity in light availability (Dai 1996, Yoshida et al. 1998).

The methods for obtaining a GLI and related available light measures vary widely. Some depend on measurement of gaps with tape measures, while others rely on optical measurement devices (such as densiometers and computer analyzed hemispherical photographs) or quantum measurement devices (such as ceptometers, the LAI-2000 plant canopy analyzer from LiCOR and the TRAC developed by the Canada Centre for Remote Sensing), (Beaudet and Messier 2002, Chen 1996, Chen and Cihlar 1995, Comeau et al. 1998, Dai 1996). Other methods rely on complex computer simulations (Gendron et al. 1998, Yoshida et al. 1998). A complete review of all the literature involving the methods to summarize canopy openness and resultant light availability is not presented here. However, a brief review of some common concerns and problems relevant to this study follows.

Light can reach any point in the forest at any point in time in one of three ways: directly through the atmosphere as incident light, reflected from other objects, or transferred directly through leaves in the canopy above (Brunner 1998). A number of studies seek to include reflected and transferred light in their estimates of available light (Chen et al. 1991, Chandrasekhar 1960). Many recent researchers ignore such factors because they represent only a minimal amount of the light available to trees (Brunner 1998). Brunner (1998) points out that for a single leaf reflected and transmitted light is generally less than 20% of the incident light intercepted. The relative contributions of reflected and transmitted light are also considerably less than incident light for whole canopies due to multiple reflection, transmittance and absorption (Canham et al. 1994).

The radiation that reaches foliage directly from the atmosphere can be either direct or diffuse, with direct radiation originating from the sun or solar disk and diffuse radiation being scattered by the earth's atmosphere (Stadt et al. 1997). Some studies explicitly calculate diffuse radiation or use it alone to estimate light availability (Parent and Messier 1996). Authors of these studies argue that cloudy days can result in incident light originating more or less uniformly from the entire sky rather than from the solar disk (Parent and Messier 1996, Comeau et al. 1998). There are questions about this approach with Dai (1996) submitting that, "diffuse light is only a small portion of the total radiation and can hardly represent total light conditions." Dai (1996) addresses the problem by including direct and diffuse radiation in proportions dictated by growing season percent cloudiness obtained from a local weather measuring station. Stadt et al.

(1997) noted that this approach may wrongly assume "that the spatial distribution of the sky view in the canopy is unimportant;" implying that it is important to consider the directional orientation of canopy openings relative to subject trees.

Studies that use hemispherical photographs to generate GLIs and other measures of available light often consider only light that passes through canopy gaps or areas deemed to be open (Yoshida et al. 1998). However, there is a large body of research that deals with estimating light that is transmitted through leaves and how light is attenuated through the forest canopy. This work is often concerned with leaf area index (LAI)—the ratio of leaf area to ground area—and makes use of Beer's law to estimate the amount of light passing through forest canopies (van Gardingen et al. 1999, Montieth and Unsworth 1990).

Warren Wilson (1959 and 1963) and Warren Wilson and Reeve (1960 and 1963) put forth some of the first methods for estimating LAI and foliage distribution without destructive sampling. Subsequent advances in LAI estimation made by MacArthur and Horn (1969) have facilitated the development of many of the devices and methods currently used to assess foliage distribution. Such research often relies on a number of assumptions such as, uniform foliage distribution, uniform leaf angle distribution and adequate amounts of data (Chen and Cihlar 1995). Larsen and Kershaw (1996) evaluated the effect of these assumptions in the application of Beer's law and concluded that while these assumptions may have little effect on canopy level estimates of available light they need to be reevaluated in regards to the light available to individual trees. Other researchers have investigated the different amount of light transmitted through different species of trees; an issue not often addressed in previous research (Canham et al. 1994).

Models relating light attenuation to LAI are often validated through measurements of leaf area that involve the collection of fallen leaves (Chen et al. 1991 and Smith et al. 1993). The estimates of available light based on LAI are generally instantaneous measurements and contain no means to account for the way in which the spatially heterogeneous distribution of foliage results in temporal variation in available light (Canham 1990, Nicotra et al. 1999)

As Comeau et al. (1998) point out "Light conditions beneath a forest canopy are dynamic because of interaction between the positions of the sun, sky conditions, and the locations of canopy gaps." Other authors concur with Comeau et al. (1998). As a result some computer

models seek to empirically simulate the structure of the forest canopy and resulting light availability (Dai 1996, Yoshida et al. 1998). These models often make predictions that are well correlated with field measurements but they are difficult to parameterize and validate for different populations because, as Yoshida et al. (1998) point out, "much data are necessary to reconstruct three-dimensional canopy structure. Current prediction methods are complicated and do not lend themselves to practical use."

Most spatially explicit gap-based indexes are validated with instantaneous or continuous measures made with quantum sensors (Parent and Messier 1996). These validations are based on a limited number of specific locations where the quantum sensors are established during a restricted time period, but the indexes are generally applied to the entire forest over the whole growing season (Dai 1996). This application of indexes beyond the spatial and temporal range for which they have been validated, while necessitated by the limitations of quantum sensors, may yield questionable results (Dai 1996).

Models and indexes of canopy gaps have led to attempts to model not only the amount of light entering the forest but also the amount of light captured by individual trees (e.g. Brunner 1998, de Castro and Fetcher 1998, Hatch et al. 1975, MacFarlane et al. 2003). Such models use simulations of tree canopies based on empirical relationships, and calculate intercepted radiation using models of seasonal changes in the sun's position (Brunner 1998). Light interception models are generally validated through the relationship between estimated intercepted light and individual tree growth (Brunner 1998). In these models there is generally no attempt made to validate the simulated canopies because there is almost never adequate data available to perform such validations (Brunner 1998).

A class of spatially explicit forest models has been developed to estimate the light captured by individual trees in 3D (Brunner 1998, MacFarlane et al. 2003). These models are explicitly formulated to account for the spatial distribution of canopy elements – leaves and branches – and resultant variability in light available to individual trees (Brunner 1998). Accurately measuring and accounting for canopy elements in an explicit 3D manner is difficult and time consuming. As a result, most light capture models depend on crude generalizations of real world tree canopies (Brunner 1998). In order to test these generalizations or develop more

accurate models, detailed 3D measurements of the canopy are necessary (MacFarlane et al. 2003, Gersonde et al., 2004).

In order to continue the exploration of the relationship between forest canopy structure and tree growth, large scale, high resolution, spatially explicit data are necessary (Brunner 1998, Dai 1996 and Chen et al. 2003). These data are necessary for validation of current methods as well as the development of spatially explicit models in the future.

1.2 Lidar and Laser Scanning

The research presented here is concerned with the development and testing of methods that make use of a new kind of instrument for measuring forest canopies. The instrument, called a laser scanner, gathers 3D data corresponding to the surfaces of nearby solid objects. Measurements made with a laser scanner should be sufficiently detailed to address questions about forest canopy interactions with the light environment. Laser scanners belong to a class of tools that gather measurements by light-detecting and ranging (lidar), a principle that has been employed for several decades in assessing forest attributes from aerial surveys (Lefsky et al. 1999, Nelson et al. 1988b). More recently, researchers have begun to use ground-based lidar instruments, including laser scanners, for measuring forest canopies (Lovell et al. 2003, Parker et al. 2004, Radtke and Bolstad 2001). The instruments typically operate by emitting laser pulses aimed at nearby objects to be measured, such as trees, branches or foliage in forest canopies. Because they rely on projected light with special, known properties rather than ambient light, lidar instruments are known as “active” or “structured” light sensing devices. Light pulses that strike the objects are reflected back to the instruments, which sense the returned pulses and calculate ranges based on pulse time of flight and the known speed of light. A simple application of lidar in forest measurements is the electronic distance measuring device (EDM), or rangefinder. When used in conjunction with electronic inclinometers, ocular reticles, compasses or horizontal angle encoders, laser EDMs have been used for tasks ranging from dendrometry to mapping (Liu 1995, Peet et al. 1997, Skovsgaard et al. 1998, Wing et al. 2004).

When multiple vertical range measurements are taken within the bounds of a plot area the relative surface area and vertical distribution of canopy elements over the plot can be estimated (Lovell et al. 2003). If the horizontal position of each measurement is recorded, or if the

instrument operates continuously while being moved along a horizontal transect at a steady pace, crude 3D profiles of canopy structure can be obtained (Parker et al. 2004). It has been suggested that, with some methodological adjustments, laser rangefinders could be used to estimate canopy structural attributes related to canopy light conditions, such as leaf inclination angles, plant area index (PAI) or leaf area index (LAI), gap fraction, or canopy heights; however, numerous technical details may complicate such efforts (Radtke and Bolstad 2001).

Tanaka et al. (2004 and 1998) developed a 3D laser imaging device for measuring forest canopy structure using a rotating visible laser light source set apart from a stationary charged coupled device (CCD) digital video camera. The camera recorded the intercepted location of the laser as it illuminated nearby tree surfaces. Their scanning instrument generated 3D range data using triangulation geometry rather than pulse return times (Curless 1999). Among the attributes Tanaka et al. (2004 and 1998) measured were stem positions and diameters, and LAI.

A few studies have used commercially available laser scanners to assess forest canopy structural attributes (Hopkinson et al. 2004 and Thies et al. 2004). These scanners are tripod-mounted lidar instruments that employ servo-controlled pan-tilt mechanisms or finely calibrated rotating mirrors to aim laser pulses in a systematic "scan" over nearby objects or scenes in their fields of view. In contrast to the *triangulation* approach used by Tanaka et al. (2004 and 1998), the instruments used by Hopkinson et al. (2004), Thies et al. (2004) and Watt and Donoghue (2005) employed *time of flight* scanning. Typically, laser pulses originate from one point in space corresponding to the scanner's vantage point or origin, and pulse returns are sensed at the same point. Range is determined by time of flight. The scanner records the angles at which pulses are aimed with respect to an internal or *native* coordinate system. Depending on how one orients the scanner, the coordinate axes can be roughly oriented to match some external reference system. For example, a practical orientation might orient the scanner X- and Y-axes to lie in a plane horizontal to the ground, with the Z-axis pointing skyward. Scanners generally have a limited field of view of the surrounding space, often measured as angles in two directions, width and height. Fields of view vary greatly among commercially available scanners, from those with relatively narrow views of 40° × 40° to those with nearly spherical 360° × 150° views (http://www.riegl.com/; http://hds.leica-geosystems.com/; http://www.optech.ca/; http://www.zf-laser.com).

Other scanning technologies might be useful for field or remote sensing of forest measurements, including *amplitude modulating* (AM) lidar, which employs a continuous light beam whose power is modulated systematically over time. Ranges are determined by interpreting the power modulations of the returned light in relation to the time phase of the emitted light's modulation (Mullen et al. 2004). In contrast, "waveform" devices use standard laser pulse time-of-flight technology, but provide information on the distribution of backscattered light rather than a single range value per emitted pulse (Drake et al. 2002 and Parker et al. 2001). Another class of laser scanner called a "digitizing camera" or "depth camera" emits a plane of light and uses an array of sensors to obtain 3D imagery nearly instantaneously (Curless 1999). Cameras that gather range information along with information on visible light are known as RGBZ or RGBD cameras (e.g., http://www.3dvsystems.com/products/zcam.html).

Scanners collect 3D data representing the surfaces of physical objects or scenes. Each surface point is mapped to the physical location where a precisely aimed laser pulse intercepted an object surface and was reflected back to the sensor. Surface point collections are often viewed in 2D as "range images" (Hoppe et al., 1992), where regularly spaced pulses originating from a single viewpoint are mapped to image pixel rows and columns. Different color values, shades or intensities denote the range at which each pulse intersected a surface in the scan. Pulses not intercepted by any object within a certain maximum range designate empty space, often denoted as black or white pixels in range images. Surfaces or objects occluded from view by other surfaces nearer to the viewpoint are not visible in range images.

Another representation of 3D surfaces is the "point cloud." Point clouds are collections of unstructured X,Y,Z coordinates, often rendered on a computer as rotating scatterplots. Point clouds do not require regular ray spacing or a single vantage point; rather, they may be constructed from data compiled from one or more stationary scans, from non-stationary scans, or those involving moving targets. In non-stationary scans the scanner vantage point moves systematically, possibly in conjunction with or as an alternative to mirror or pan-tilt scanning. Moving-target scans are generally acquired from a fixed vantage point, but with the target object passing by the scanner at a controlled rate. Point clouds are able to represent surface points that may be occluded or hidden from one vantage point but visible from another. Both range images

and point clouds are generally considered “raw” representations of 3D scanner data sets (Curless 1999).

Although range images and point clouds often look appealing and interesting to the eye, most applications require extraction of some essential information from the raw data to answer a particular question of interest. Such information typically includes measurements of the dimensions and shapes of objects being scanned. In practice, information acquired from laser scan data involves any number of purposes: monitoring deformities or damage to turbine blades, industrial tanks, pipelines, bridges or overhead cables; measuring volumes of irregular objects such as mine faces, refuse piles, sinkholes or caverns; high-precision surveying applications for contour and feature mapping, bearing and angle measurement, and clearance determination; reverse-engineering for computer-aided design and analysis, legacy part duplication, copy milling, and rescaling; documentation of unique natural objects, buildings, and works of art; computer modeling of human subjects; and a rapidly increasing list of other applications.

1.3 Range Image Segmentation and Surface Reconstruction

Range image or point cloud *segmentation* is a process of partitioning raw scanner data into regions that decompose the scanned objects into a set of surfaces, each of which may be represented by an appropriate combination of geometric primitives. Its main goal is to divide an image into parts that match objects or features in the real world. Primitives generally include simple shapes such as planes, points, lines, curves, cylinders, spheres, or other relatively simple geometric representations. Considerable attention has been given to problems involving automatic segmentation of range images. These methods often take advantage of the structured nature of range images to detect surface edges based on differences in range values between adjacent pixels. The difference is compared to a threshold value that may depend on the angle of the surface being scanned with respect to the scanner pulse orientations. *Edge-based* segmentation has certain limitations, including the difficulty in detecting edges of surfaces that slope away from the scanner, i.e. those surfaces that are nearly parallel to laser pulses. Further, finding edges in noisy or dense range images can be difficult. Advantages to edge-based segmentation include the relative computational speed with which edges can be detected, and the suitability of the problem to parallel processing, since edges in one part of a scene can be

identified independently of those in other parts of the scene (Hetzel et al. 2001, Hoffman and Jain 1987).

In contrast, *region-based* segmentation aims to search for homogeneous portions of a range image, expanding or growing a segmented region outward from a start point or seed. Various criteria can be used to define "homogeneous", including color, shape or surface reflectivity. Region-based segmentation is often iterative and therefore much slower than edge-based segmentation procedures. Results may be sensitive to the choice of the initial seed region, and be subject to over- or under-segmentation. Advantages include robustness in dense and noisy data sets, and their ability to always produce closed regions or surfaces. Since region growing and edge detection are complementary processes, the two methods are often used in conjunction (Fitzgibbon et al. 1997 and Khalifa et al. 2003).

Surface reconstruction is used to develop a surface approximation from range image or point cloud data of the surface of some unknown object in the real world. The approximation may be nonparametric, such as with mesh networks, space envelopes or voxelization (Hoover et al. 1998, Kaufman et al. 1993, Sun et al., 2001). Alternatively, the approximation may employ one or more functional models including planes, curves, spheres, or other regular shapes. Surface reconstruction may be carried out in conjunction with segmentation, or following it in sequence. Whether nonparametric or functional reconstruction is needed depends on the goal of modeling. For instance, digitization of artworks or heritage objects may seek to merely preserve a record of certain artifacts, while industrial applications may require precise mathematical representations of objects being scanned. Both approaches aim to extract essential surface information from scan data, with a substantial reduction in data resulting. Modeled surfaces may be used subsequently in applications ranging from heritage archiving to virtual reality, and from reverse engineering to manipulation of large objects by robots (Beraldin et al. 2000, Fitzgibbon et al. 1997, Hoppe et al. 1992).

1.4 Registration

Often scanning is carried out from more than one vantage point so that parts of an object hidden from one vantage point can be viewed from another. Some scanning systems are capable of changing vantage points in a carefully measured reference frame, so that the scanner origin

and orientation are precisely known at all times. Knowing the relative positions and orientations, or pose, of the scanner allows data from different scans to be aligned with each other. The pose of a scanner determines the directions of its coordinate system X-, Y- and Z-axes. Denoting a surface point from coordinate system 1 as $\tilde{\mathbf{p}}_1$ and a matched or paired surface point from coordinate system 2 as $\tilde{\mathbf{p}}_2$ the distance between points is given by the norm of their differences.

$$d = \left|\tilde{\mathbf{p}}_1 - \tilde{\mathbf{p}}_2\right| \qquad [1]$$

In its simplest form, alignment, or registration, is a process of transforming point cloud data from one scan to match the coordinate system of another so that the distance between matched points is minimized. The transformation involves a 3D rotation and translation of XYZ surface data from the scanner's native coordinate system to a target or global coordinate system.

$$T\left(\tilde{\mathbf{p}}\right) = \mathbf{A}\tilde{\mathbf{p}} + \tilde{\mathbf{b}} \qquad [2]$$

Where:

$T\left(\tilde{\mathbf{p}}\right)$ = transformed (registered) surface point

$\mathbf{A}$ = 3 x 3 rotation matrix

$\tilde{\mathbf{p}}$ = untransformed surface point 3-vector from scanner point cloud

$\tilde{\mathbf{b}}$ = translation 3-vector

In the absence of errors, if the transformation in [2] aligns data from coordinate system 2 to coordinate system 1 then $\tilde{\mathbf{p}}_1 = \mathbf{A}\tilde{\mathbf{p}}_2 + \tilde{\mathbf{b}}$. Further, under an error-free transformation the distance between matched points Equation [1] would be zero.

When relative scanner poses are precisely known, determination of $\mathbf{A}$ and $\tilde{\mathbf{b}}$ is straightforward. In the absence of detailed pose information accurate registration of range images generally depends on the extraction and matching of common surfaces or intentionally placed artificial control points in overlapping, unregistered scenes. The common surfaces or control points are then used to find $\mathbf{A}$ and $\tilde{\mathbf{b}}$; thus, segmentation can play an important role in range image registration when it is used to extract object surfaces used as control points. Segmentation

can also play a role in how well control surfaces match between range images. Incorrect matching of surfaces generally makes accurate registration impossible.

1.5 Range Image Errors

Image registration, segmentation and surface reconstruction are often highly interrelated procedures, all of which are affected by errors or "noise" in range images. Noise refers to pulse returns from nuisance surfaces, or to inaccurate measurements of a surface of interest due to range or angle measurement errors. Inaccuracies result from limits on the precision of angle measurements or aiming mechanisms, variance in pulse-based range measurements plus distance-dependent variances, target reflectivity and incidence angle between pulse and target, issues related to beam and ray divergence, and any uncontrolled movement of a scanner or its targets.

The magnitudes of aiming inaccuracies are generally small relative to other range image errors, typically < 0.01°, which translates to position errors < 0.02% of range. Range measurement errors are instrument-dependent. Eye-safe lasers using near-infrared wavelengths result in somewhat larger range measurement variances than other non-commercial scanners that rely on high-powered (non eye-safe) lasers. Short-range scanners have smaller range measurement errors. For example, range standard deviations of 15 mm could be expected for scanners with operating ranges of 10 to 1000 m, standard deviations of 5 mm are typical for scanners with ranges between 1 and 200 m, and standard deviations < 1 mm are typical for scanners with operating ranges < 10 m. In addition, distance-dependent range errors contribute a small error component; however, they are generally small enough to be reported in parts per million (ppm), where 1 ppm corresponds to a range error of 1 mm at 1 km range. Some manufacturers report "position" errors of 6 mm in scanner operating ranges of 1.5 m to 50 m (http://www.mensi.com/; http://www.riegl.com/; http://www.iqvolution.com/; http://hds.leica-geosystems.com/).

Color, texture, reflectivity and incidence angle of scanned surfaces all affect errors in range measurements. As an example, Clark and Robson (2004) describe the case of scanning a large grey airplane with a black stripe painted on its side. The point cloud showed a false indentation 2-3 mm deep along the region of the stripe. They tested a scanner that showed range

measurements were sensitive to surface color when the incidence angles between scanner pulses and object surfaces were non-normal. For single colored surfaces, Clark and Robson (2004) noted the variance of range measurements was actually smallest for pulse incidence angles 60° from normal; however, a trade-off was noted because point density is reduced on surfaces that slope away from a scanner. For any particular scanner it may be possible to develop correction factors to account for surface features and incidence angles.

Another type of noise in range images is related to beam width and divergence. Scanner laser beams typically exit the instrument with diameters of several mm and diverge at constant rates generally reported as 1-3 milliradians (mrad). One mrad corresponds to a beam width of 10 cm at a distance of 100 m. Parker et al. (2004) noted that when laser pulses overlapped the edge of a surface inaccurate range measurements resulted. They also noted the effect could be mitigated by averaging multiple pulse returns, either as a function of the instrument or in post-processing. Uncontrolled movement of a scanner or its targets causes obvious distortions in range images, often exhibited as linear striae extending perpendicular to the direction of movement. To avoid this type of noise in forest or tree measurements, care must be taken to conduct scanning only during calm wind conditions.

While noise and other errors can be quantified in range images by simple verification procedures, the effects of such errors on surface reconstruction, segmentation and registration tend to accumulate non-linearly. Quantifying such errors requires a degree of sophistication since it involves comparisons of modeled surfaces or edges with independent measurements of real-world objects. Such errors accumulate during data processing, for example, when inaccurate segmentation edges or regions are used as controls for subsequent point cloud registration. When object modeling and segmentation are iterated as additional range images are aligned in a global data set, a trade off occurs between the increased availability of surface points for modeling and the possible errors in registration.

1.6 Laser Scanning for Tree and Forest Measurements

Numerous solutions for acquisition, segmentation, modeling and alignment of laser scanning imagery have become available in recent years, all of them at considerable cost in terms of capital, time, effort and expertise required to achieve them. Literature available from

commercial providers confirms that the majority of turnkey laser scanning solutions are tailored to engineering, industry, architecture, surveying, heritage preservation, and digital graphics applications. Trees and other vegetation are typically regarded as nuisance objects to be avoided in laser scanning. Costs of laser scanning are relatively high, especially for custom applications. Hardware and software costs typically exceed $100,000 for laser scanning systems, and $10,000 for data processing software. Even at these costs, the level of expertise needed to operate commercially available hardware and software is high. For example, Hopkinson et al. (2004) and Thies et al. (2004) employed professional surveying firms to perform laser scanning and subsequent data processing.

While the costs of hardware and software may decrease over time, at present a need exists for demonstrating the utility of laser scanning technology in forest measurement and modeling applications. This need seems especially evident given recent advancements in modeling forest canopy structure in relation to the light environment; yet, reliable data for parameterizing such models are lacking. Further needs include the development of practical techniques for segmentation, modeling and alignment of range images of forests and trees. Knowledge of optimal scanner configurations for data acquisition is needed along with information on the errors associated with laser scanning in forested settings. Advances in these areas will make a significant contribution to the emergence of ground-based laser scanning as a tool for investigating relationships between canopy structure and forest ecosystem interactions with the environment.

1.7 Objectives

The objective of this work is to examine the practicality and utility of assessing 3D forest canopy structure with a ground-based laser scanner. Reaching this objective will require the creation of methods to collect, segment and register the laser scanner data at an appropriate scale and resolution. The following specific goals will be addressed:

- Develop tools for image segmentation, tree-surface modeling, and aligning scans made from different vantage points.
- Determine the volume of space occluded from view in any or all of the range images.
- Identify the forest floor and top of the canopy as constraints for maps of canopy structure.
- Estimate individual tree parameters and relative positions.
- Re-classify range images into cubes resulting in 3D maps of intercepted canopy surfaces.
- Estimate horizontal and vertical distributions of canopy structure.

Optimizing the methods and addressing the research objectives will require decisions on how best to use the range image data for the stated goals. These types of decisions may be useful for future research involving ground-based laser scanners and will help to determine the overall utility of the research. The following paragraphs describe some details of ancillary objectives and tasks that will be addressed in meeting the research objectives stated above.

Examine the role of occlusion in registered and unregistered range images

In range images of the forest there will be areas that are blocked from the view of the imaging device. It is necessary to determine the extent of these occluded areas and the degree to which they can be reduced by registering range images obtained from different vantage points. The results of this examination will determine the need to devise a means to interpolate or otherwise address occluded areas.

Determine an appropriate cell size for reclassification of range images into maps of intercepted canopy surfaces.

There will be an appropriate cell size for capturing the spatial heterogeneity of the forest canopy as represented in the range images. Initial work will be performed using a range of cell sizes to determine the size that fully exploits the data and results in a resolution representative of the distribution of canopy structure. Cell size will be further evaluated based on computing time, the overall accuracy of the registered scanner data and the needs of specific applications.

Evaluate the use of range images obtained in periods of leaf-on versus leaf-off

With deciduous trees being prevalent on the study site the information obtained from range images when trees have leaves may be very different from that obtained after leaf-off. The proposed research will require an understanding of the likely reduction in occluded space possible with leaf-off range images versus the potentially more accurate assessment of canopy surface distribution from leaf-on range images.

Determine the utility of registration in reducing occlusion

In order to obtain optimal information about the 3D distribution of canopy structure occlusion will need to be minimized. Occlusion will be minimized through registration of laser scanner data obtained from multiple vantage points. The role of registration in reducing occlusion will help determine the utility of laser scanners for gathering 3D canopy structure data.

Create methods to automate point cloud segmentation

The registration of scanner data will be greatly aided by the development of an automated algorithm that provides surfaces to serve as registration control points. The features used as control surfaces for registration will also be used to validate the registrations. Further, the segmented data will provide information about the 3D distribution of the selected surfaces within the forest.

Determine the appropriate surfaces to serve as control points in registration

Determining which surfaces can be most accurately segmented and matched between range images will directly determine the accuracy of the registration. Surfaces will be selected that facilitate automated segmentation and matching. The surfaces selected will also provide a

basis for evaluating the registration through comparison to the distribution of those surfaces from independent data sources.

Create methods to summarize point cloud data

The unstructured data in registered point clouds will be summarized to create data sets of a manageable size, to capture the 3D distribution of canopy structure. Current applications that involve 3D canopy structure will be used to direct the type of data summary. The ability to summarize the data into useful formats will help to determine the immediate utility of the scanner in addressing current data needs.

Generate canopy height models

Canopy height models are analogous to digital terrain models but instead of representing the ground surface they represent the surface of the top of the canopy. Surface models of the relative elevation of the top of the canopy and the height of the canopy above ground are valuable tools in research involving relative crown positions and overall canopy structure. A large body of research employs remote sensing derived canopy height models to estimate tree and plot level parameters such as number of stems, individual tree height, stand volume, average tree height and stand biomass (Popescu et al 2002 and. 2004, Nelson et al. 1988b, Holmgren et al. 2003).

Generate estimates of plant and leaf area index from maps of intercepted canopy surfaces

Leaf-area is a common measurement used in models that consider canopy structure. The amount of plant area and leaf area in forest canopies is a determining factor of the influence of canopy structure on tree growth, while also being a controlling factor of how much light makes it to the lower reaches of the canopy. Estimates of leaf area made from canopy structure maps will be compared to measurements of leaf area at nearby study sites (Vose et al. 1995 and Bolstad et al. 2001).

These tasks are necessary to complete the proposed research but also provide insight into future applications of the ground-based laser scanner.

1.8 Hypotheses

The above tools and tasks will support the evaluations of the following hypotheses.

1. Tripod mounted laser scanners provide a practical means to make useful measurements of forest features.
2. Registration of laser scanner data obtained from multiple vantage points will minimize the effects of occlusion and provide a complete assessment of the 3D distribution surfaces within the forest.
3. Data gathered with a laser scanner will further current understanding of the relationships between 3D canopy distribution and forest development by providing data not available with current methods (i.e. gap fraction, quantum sensor measurements and simulation-based light-interception models).

Laser scanners are just emerging as possible tools for forest mensuration. Currently they are limited largely by the knowledge necessary to manage and apply the data. The exact nature of the data and unforeseen challenges in using the data need to be explored. Hypothesis 1 addresses this initial exploration of the data. Evaluation of this hypothesis will include consideration of the time and effort necessary to create useful measurements from the laser scanner data as well as the accuracy of those measurements.

Hypothesis 2 addresses the major limitation of the laser scanner in gathering "complete" 3D forest data. The accuracy of the registration procedure will be addressed by comparison to the relative positions of features measured independently in the scanner data and in the real world. The amount of occlusion in raw range images and the relative reduction in occlusion through the registration and combining of multiple scans will be used to evaluate Hypothesis 2.

Evaluation of Hypothesis 3 will assess, as directly as possible, the utility of the laser scanner for meeting the need to gather spatially explicit 3D data about the forest canopy. Gathering of information related to the distribution of foliage in the forest canopy is limited by the expense and difficulty of mapping the location of these elements *in situ* (MacFarlane et al. 2003). Evidence in support of Hypothesis 3 will support the utility of laser scanning as a tool for gathering canopy structure data to be used in forest ecosystem modeling.

2 Methods

The methods to be described here include: a basic description of the study site; methods of acquiring laser range images, including a description of the laser scanning instrument used; details of range image registration; methods for summarizing the laser scan data; and finally, development of applications to use the point cloud data in quantifying 3D canopy structure distribution.

2.1 Data

2.1.1 Study site

Field data were obtained at the Coweeta Hydrologic Laboratory (35º 03' N, 83º 26' W) in the southern Appalachian Mountains of western North Carolina, USA. The study site was chosen to coincide with part of a long-term ecological study called the "Coweeta terrestrial gradient tree growth survey." Fieldwork was conducted on a permanent 80 m × 80 m research plot denoted terrestrial gradient plot 2, watershed 18, i.e. "plot 218," one of five plots in the terrestrial gradient tree growth study at Coweeta. Plot 218 was initially established in 1993 under a second-growth hardwood forest canopy at an elevation of 801 m with a slope of 21º. The original plot layout was 20 m × 40 m; however, the plot boundaries were expanded around the original plot to 80 m × 80 m in 1996 and have been maintained at the expanded size since then.

Stems ≥ 1 cm within the plot boundaries are permanently marked by numbered metal tags. Stem X, Y rectangular coordinates (meters from a marked corner of the plot) are recorded for each tree in a publicly available database. Plastic tubes driven into the ground on a regular 10 m × 10 m grid mark corners of .01 ha square subsections of the plot. Stem breast height diameters (dbh) measurements were made on live trees prior to leaf-out before growing seasons in 1993, 1995, 1996, 1998, 2002, and 2004.

Major species on the plot include *Acer rubrum* L., *Liriodendron tulipifera* L., and *Carya glabra* (Mill.), several species of oak (*Quercus coccinea* Muenchh., *Q. prinus* L., *Q. rubra* L., and *Q. velutina* Lam.), and *Robinia pseudoacacia* L.. Notable understory tree species include

Betula lenta L., *Cornus florida* L., *Oxydendrum arboreum* (L.) DC., and *Nyssa sylvatica* Marsh. Basal area of about 30 m^2/ha has been observed during the most recent gradient plot tree surveys of plot 218.

2.1.2 Ground-based laser scanning system

Range images were acquired using a model LMS-Z210 motorized 3D laser-imaging sensor, manufactured by Riegl USA Inc. (Orlando, FL). The LMS-Z210 scanner is a cylindrical-shaped apparatus weighing roughly 13 kg, and is designed to be operated while mounted on a surveyor's tripod. One half of the cylinder remains stationary, mounted to the tripod, while the scanner operates. The other half rotates slowly clockwise and counterclockwise around a central axis, never rotating more than 333° before reversing its direction. The instrument is powered by 12-volt DC power source, typically a deep-cycle marine battery when operating in field conditions. Data are transferred to a laptop computer via serial connection, and logged to the computer's disk drive using proprietary software (3D-Riscan v. 2.25.0.25) provided by the manufacturer.

Range images acquired with the LMS-Z210 use a spherical coordinate system illustrated in Figure 2.1A. Spherical coordinates consisting of an azimuth angle, a polar angle, and a range are assigned for each datum in the range image. Azimuth angle is defined as the clockwise angle between the positive X-axis and the point, in the XY-plane, bounded between 0° and 360°. Polar angle is the angle from the point to the positive Z-axis, between 0° and 180°. The range is the distance (m) from the scanner origin to the point where the pulse reflected off of a solid object. The scanner's polar angle range is limited by the width of a glass aperture called the scanning pane, behind which the laser mechanism operates (Figure 2.1B). The scanning pane allows a maximum polar angle of 80°. The azimuth angle range is limited by the rotation of the cylinder. Thus, the field of view for range imaging is limited to 80° × 333°. For all scans used in this research the scanner was mounted in a prone position, as in Figure 2.1B, with the scanner's Z-axis horizontal and the scanner's positive X-direction aimed vertically down, roughly plumb to the earth. The scanner was mounted in this position on a standard surveyor's tripod and leveled to ensure that the Z-axis was nearly horizontal and the X-axis nearly plumb.

A triangular prism-shaped mirror rotates rapidly inside the scanner, behind the scanning pane, directing laser pulses at known polar angles Figure 2.1B. The sweeping series of pulses covering the polar range is analogous to a scan line in scanning aerial lidar applications. Laser pulse azimuthal directions are controlled by the slow rotation of the scanner cylinder. The range measurement for each combination of known azimuth and polar angles is determined using the time of flight principle. A sensor behind the scanning pane measures the reflected pulses. Coordinates for a point are defined relative to an origin located inside the instrument. The origin is offset from the tripod mount bracket by a small distance provided in the instrument's operation manual.

The LMS-Z210 has a maximum field of view limited to polar angles between 50º and 130º and an azimuth angle between 13.5º and 346.5º (see Figure 2.1B). With the scanner in the prone position the azimuth limits restrict the scanner from being able to see straight down, which, for the purposes of this research, is of little consequence because interest lies in the distribution of the canopy overhead. However, the limited polar angle required that at least three scans be gathered from one location in order to capture a completely hemispherical view from that location.

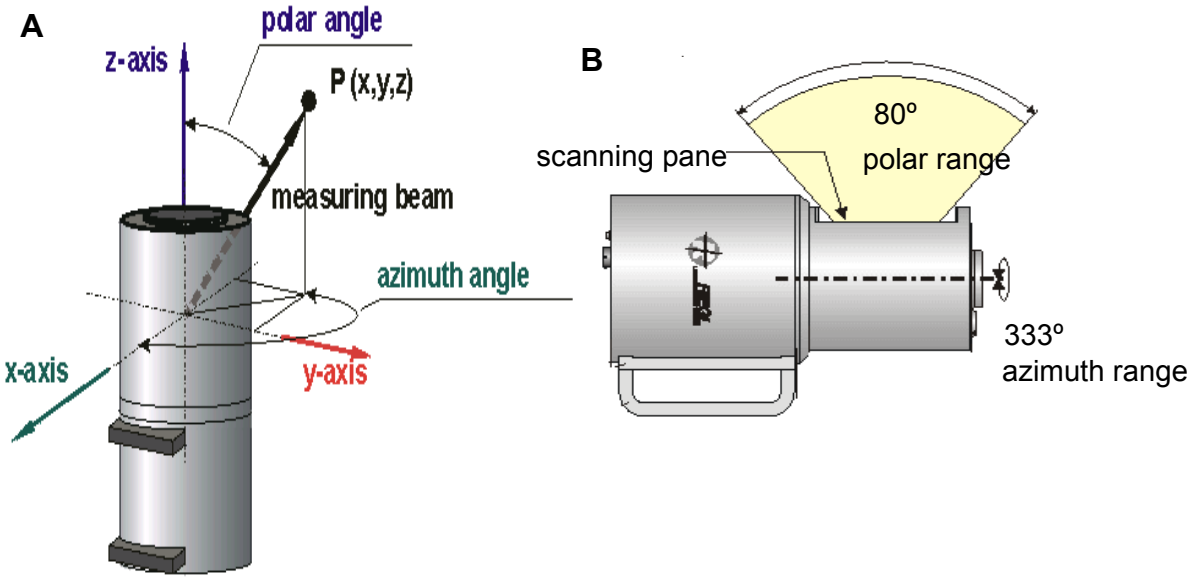

Figure 2.1. Description of the axes for the scanner data (A). The coordinates of all data obtained by the scanner are in reference to these axes with the scanner as the origin. The scanner was typically used in prone position (B).

The data acquisition software also translates spherical coordinates for each range measurement into XYZ Cartesian coordinates. The Cartesian coordinates were used in most data processing and the spherical coordinates were used when it was necessary to know the path of the laser pulse. The spherical coordinates were also used to determine the direction of pulses that passed through the canopy without being intercepted. Such pulses have no range measurement and therefore could not be translated into Cartesian coordinates. Unlike range images a number of familiar software programs are available to manipulate and graph Cartesian data. SAS® Interactive Data Analysis (© SAS Institute Inc., Cary, NC, USA), Microsoft® Office Excel (© Microsoft Corporation, USA) and SigmaPlot® (© SPSS Inc., Chicago, IL) software packages were used to view and manipulate the scanner data in point cloud form.

The scanner also collected color from visible light in red, green and blue (RGB) brightness values ranging from 0 to 255. Intensity of laser returns were generated simultaneously by the instrument and recorded as brightness values ranging from 0 to 255. Neither RGB nor return intensity data were used here; however, viewing range images color-coded by return intensity values in the data acquisition software sometimes aided the operator in verifying that the instrument was acquiring data correctly, or helped the operator orient himself to the scene

being acquired. However, color and intensity were not used in data processing. Only spherical and Cartesian coordinates were exported from 3D-Riscan in ASCII delimited text files to minimize the size of those files.

2.1.3 Laser scanner data acquisition

Laser-scanner data were acquired on December 18, 2001 and August 21, 2002 corresponding to periods of leaf-off and leaf-on, respectively. The scanner was positioned over the nodes of the marked 10 m × 10 m grid points within and around the 20 m × 40 m interior plot, resulting in a total of 15 scanner locations (Figure 2.2). The positioning of the scanner was intended to provide a relatively complete survey of the forest canopy volume over the interior plot. The tripod height was recorded for each scan. Where it was not possible to place the scanner directly over a grid node due to obstruction by trees or other objects, the scanner was placed a measured distance within 1m of the node marker in a manner to minimize the portion of the forest scene blocked from the scanner view by the obstruction.

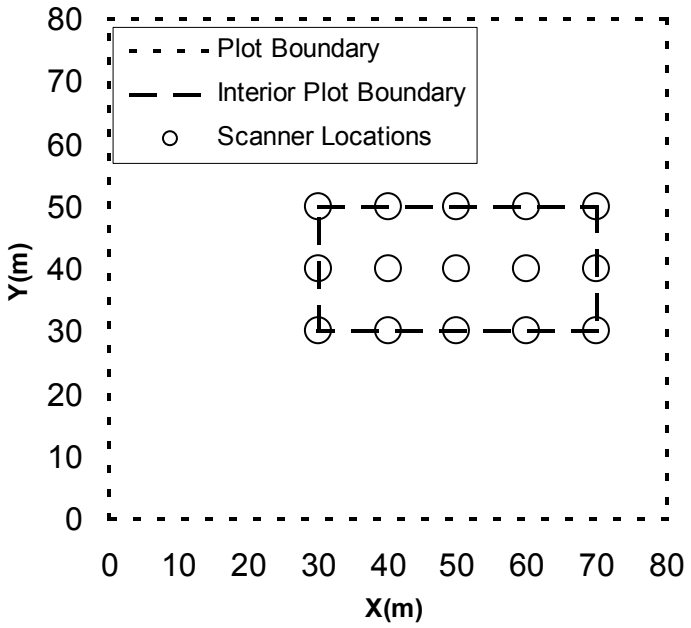

Figure 2.2. Scanner locations in the 80 m × 80 m terrestrial gradient tree survey plot 218 at Coweeta.

Although range imaging was carried out at the same plot nodes in both winter (leaf-off) and summer (leaf-on) field surveys, modest changes in scan acquisition protocols were made between the two surveys. Leaf-off scans acquired along the interior plot boundaries (Figure 2.2) were made at a relatively narrow angular stepwidth of 0.144° (0.16 gon) in both the polar and azimuth directions. This resolution resulted in roughly 48 range measurements collected in every 1° × 1° sector in the scanner's field of view, each with a corresponding footprint of 2.5 cm × 2.5 cm at a 10 m distance from the scanner. At such a resolution, scans made at the instrument's maximum field of view, 80° × 333°, would have comprised 1.28 million range measurements. Scan acquisition times averaged 14 minutes per 1 million data points. Including positioning and moving the apparatus, the average time needed to acquire full hemispherical coverage from a location, i.e. three maximum field-of-view scans, was approximately one hour.

To reduce the time spent acquiring high resolution imagery, the azimuthal extents and orientations of scans made around the interior plot boundaries were limited to exclude areas outside the plot boundaries. Limiting the field of view to areas inside the plot boundaries resulted in scans of 80° × 172° comprised of 662,196 range measurements per tripod location at nodes around the plot's border. Focusing on the interior plot resulted in only two scans being needed at the plot corner nodes with three scans required at all other nodes (Figure 2.3). For scans from the three interior grid nodes (plot coordinates (40, 40), (50, 40) and (60, 40), see Figure 2.2), the scan resolution was set to 0.18° (0.20 gon). This resolution resulted in roughly 31 range measurements collected in every 1° × 1° sector in the scanner's field of view, each with a corresponding footprint of 3 cm × 3 cm at a 10 m distance from the scanner. At such a resolution, scans made at the instrument's maximum field of view comprised 821,400 range measurements. 41 scans were obtained during the leaf-off data collection.

Summer (leaf-on) scans at all nodes were acquired using an angular resolution of 0.18°, with three overlapping scans comprising a complete hemispherical coverage above each node marker (Figure 2.3). The scanner field of view was limited to 80° × 270°, which minimized scanning of the ground directly below scanner and resulted in 666,000 range measurements being obtained in each scan. By using the lower angular resolution and limited field of view, the time needed to acquire complete coverage at all nodes, both interior and along plot boundaries, was not prohibitive. 45 scans were obtained during the leaf-on data collection.

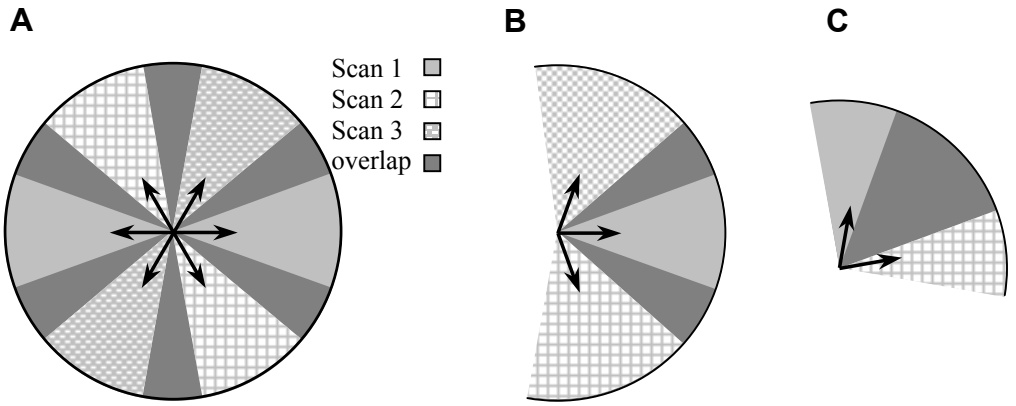

Figure 2.3. Scanner arrangements and orientations for full hemispherical coverage (A), coverage for scans made along plot boundaries during leaf-off (B) and at plot corners (C). In A and B scans 2 and 3 were obtained by rotating the scanner 60° clockwise and counter-clockwise, respectively, from the scan 1 position. In C a 40° clockwise rotation was used.

2.2 Range image registration

Unlike many remote-sensing technologies, range imaging is not generally subject to non-affine distortions that necessitate complex orthorectification procedures. As described in Equation [2], registration here required only a 3D rotation and translation, or shift, of XYZ point cloud data from the scanner's unregistered or "raw" coordinate system to a target or "global" coordinate system.

All points obtained in one laser scan are registered with the same rotation matrix ($\mathbf{A}$) and translation or "shift" vector ($\tilde{\mathbf{b}}$). A unique $\mathbf{A}$, $\tilde{\mathbf{b}}$ transformation is needed for each scan to register it to the global coordinate system. The goal of registration was to align all scans to the Coweeta terrestrial gradient plot 218 XY coordinates (Figure 2.2), which served as the designated global coordinate system. To account for sloping terrain, global coordinates defined Z as the vertical distance (m) above a horizontal reference plane at the same elevation as the central plot node at XY coordinates (50, 40). Vertical measurements were made in reference to distances above or below this horizontal plane.

Accurate registration of scans generally depends on the extraction and matching of common surfaces or control points in overlapping, unregistered scenes. The common surfaces or control points are then used to find $\mathbf{A}$ and $\tilde{\mathbf{b}}$ that give optimal alignment. Artificial control

points, such as reflective targets, were not used here for several reasons related to the complexity of working with range images of natural scenes. First, it was difficult to find positions where targets would be visible from various scanner vantage points. Second, the number of targets needed to ensure a sufficient number of control points in each overlapping scene was prohibitive. Third, to ensure accurate registration points high in the canopy would have required the placement of targets well above ground level. To avoid these difficulties, positions derived from tree stem surfaces were used as control points in scene registration. The following sections explain details of the algorithm developed and used to extract control points and subsequently register the range images acquired at Coweeta.

All registration methods were performed using the Cartesian point cloud XYZ data, but final registrations were applied to both Cartesian and spherical coordinates. The registration algorithm involved a first-pass, coarse registration, of scans based on field notes recording scanner positions and orientations. A second pass, fine registration relied on an automated detection and extraction of surfaces representing sections of tree boles in the 3D point-clouds. The tree boles in one scan were matched to corresponding tree bole sections in other scans. Common surfaces were established and the iterative closest point (ICP) method of Besl and McKay (1992) was used to find rotation matrices and translation vectors to register the scans to a common coordinate system. Finally, the registered scans were aligned to the global (field plot) coordinate system by adjustments to account for sloping terrain and the grid node locations. The following sections elaborate on these basic steps and present parameters used in the registration algorithms applied here.

2.2.1 Coarse registration

Coarse registration was performed for all scans based on the arrangement and pose of the scanner in relation to the plot coordinate system, as recorded in the field. This involved an initial transformation of raw scanner data so the XY-plane was horizontal and the Z-axis was vertical. This step was necessary because in the scanner's native coordinate system, the Y- and Z-axes define a horizontal plane (Figure 2.1B). Point clouds were translated; shifting their origins to match the node coordinates at which each scan was acquired. Each scan was then rotated about its Z-axis to roughly align it with other scans made from the same plot node (Figure 2.3). For

example, data from scan 2 at a particular plot node (Figure 2.3A) were roughly aligned to the coordinate system of scan 1 from the same plot node by a clockwise rotation of 60° about the vertical axis. Because instrument orientation and positions were not measured to a high degree of accuracy in the field, such adjustments were approximate; however, the coarse registration was helpful in expediting further, more accurate registrations based on matching bole surfaces and control points.

2.2.2 Locating and extracting bole sections

Numerous tree bole sections were identified and extracted to serve as a database of potential control points in scans to be registered. Bole sections were a logical choice of features to match in a forested scene because they were relatively easy to find and have relatively predictable upright, tapered, cylindrical forms. Computer software with 2D and 3D graphing and manipulation capabilities, such as 3D-Riscan (RIEGL Laser Measurement Systems GmbH), SAS® Interactive Data Analysis (© SAS Institute Inc., Cary, NC, USA) and Microsoft® Office Excel (© Microsoft Corporation, USA) were used to expedite selection and manual extraction of trees and bole sections. Manual extraction of trees and bole sections involved visual inspection of range images and point clouds using the software tools listed. Selection of points to be extracted was carried out using mouse-controlled graphical user interface features, filters, and "gate" functions of the various software packages.

Typically, the process employed working with truncated sections of a particular range-image. For example, a 10 m × 10 m horizontal gate was often employed to limit the extent of the point cloud being examined. Within such a gated area, one or more prominent stems could usually be identified in the range image. In most cases the gate was shifted, expanded or reduced to center on and fully encompass the tree of interest. Selection tools were then used in conjunction with various marginal 2D views and rotated scatterplot views to highlight nuisance points from the ground or vegetation surrounding the tree of interest. Such nuisance points were deleted from the image in an iterative fashion, expanding the image's view size after each deletion to increase the point cloud scale for greater ease of selecting further nuisance points. No minimum limit was placed on the sizes of trees to be identified or their distances from the

scanner. In general, trees were targeted that were clearly visible in a range image and showed the characteristic tapered cylindrical form commonly associated with tree boles.

To the degree possible, delineations between adjacent tree crowns were made by visual inspection. Once completely extracted from its surroundings, the data set of points comprising the target tree was given a unique identifier and saved electronically. A second truncation was made to extract only the points representing the main bole of each target tree, excluding branches or leaves well above the base of the live crown. Data points representing small branches protruding from the main stem were deleted from a position as close to the bole as possible. Bole sections were cropped at the height of the first major branch, where cylindrical nature of the bole surface was no longer evident due to its small size or a defect in form, or where interfering vegetation made it impossible to clearly view the bole. In some cases it was possible to extract a full bole section from ground to the height of the first major branch. In other cases only a partial section of the bole was clearly visible or otherwise suitable for extraction. In a few cases two separate sections of the main bole could be extracted with an intermediate section occluded by nuisance vegetation. At this point it was not necessary to link the tree and bole section identifiers to the tree tag numbers used in the Coweeta field measurements. This step was accomplished following the registration of range images to the field plot's global coordinate system.

2.2.2.1 Method for automated bole section location and extraction

To overcome the labor-intensive process of isolating and extracting individual tree boles for range image registration, an algorithm was developed to automate the procedure. As noted earlier, the goal of extracting trees and bole sections was to provide control points and surfaces for image registration. Identification of individual trees was also seen as a useful capability for other applications of laser scanning in forested settings, such as stem mapping and measuring tree dimensions from point clouds.

The search space for locating bole sections was restricted to a 40 m × 40 m horizontal gated area around the scanner, i.e. restricting the search space to $\{-20 \leq X \leq 20\}$ and $\{-20 \leq Y \leq 20\}$ with respect to the scanner. No vertical boundary was placed on the search space as point clouds were bounded by the ground and the top of the canopy. Beyond the 40 m horizontal limits surface point densities and visibility were generally insufficient to identify bole sections reliably.

Each individual point cloud was sectioned into a regular lattice of equal-sized cubes, and an algorithm was developed to search within and among cubes for data patterns representing tree bole surfaces (Figure 2.4a). One meter cube divisions were used, slightly larger than the largest stem diameters of trees on the plot. Several assumptions were made regarding the way tree bole sections give rise to patterns in point clouds: 1) Point densities are relatively high on bole surfaces compared to other vegetative structures such as leaves or branches; 2) Tree boles are roughly vertical over a significant portion of their length so that a section of bole occurring in one cube is likely to occur in several cubes immediately above or below; 3) No more than one tree bole will occupy a vertical column 1 m × 1 m wide; 4) Bole sections terminate at the ground on their lower end, but the upper limit may vary among trees.

To avoid difficulties of interpreting data points representing the ground surface, a 1 m buffer of points with the smallest Z values in each column were deleted. Next, the number of laser points intersecting surfaces within each cube was calculated. In each vertical column, the cube containing the greatest number of points was identified as the cube of maximum density (shaded cells, Figure 2.4b). Of all the maximum density cubes, only those containing fewer than 30% of the column's data points were selected as "seed" cubes, i.e. those most likely to include a viable bole section based on the assumptions used. Restricting the seed cubes to enclose a relatively small fraction of the total number of data points in a column ensured that the vertical distribution of data points was relatively uniform in the column. Such would be the case if a bole section were present.

A further restriction on seed cubes required them to contain at least 25 data points. This minimum point density was employed to exclude columns containing trees too small in diameter to be useful for scene registration, eliminate trees too far from the scanner to be reliably identified, and to reduce the total number of trees found by the search algorithm. The selection of seed cubes reduced the region on which the search for recognizable bole sections continued.

a)

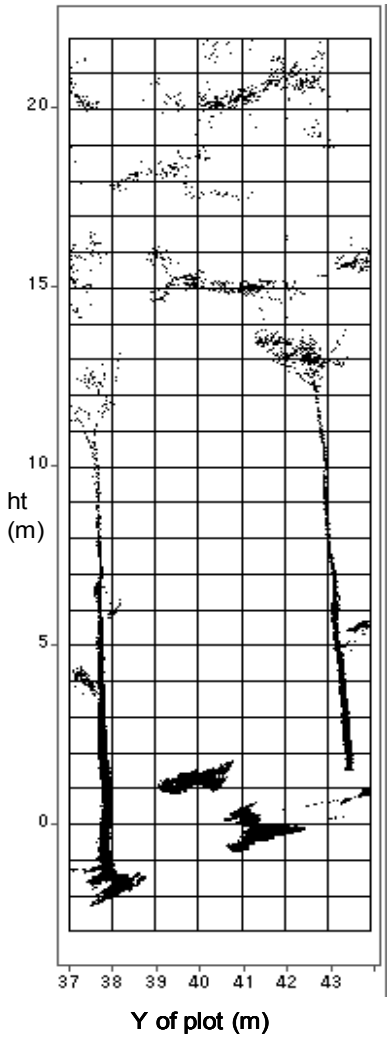

b)

Column lower bound (m)							Row height
37	38	39	40	41	42	43	lower bound
0.0	0.0	0.0	0.2	0.4	4.6	0.0	21
0.3	0.0	0.3	1.2	1.5	11.7	0.0	20
0.0	0.0	0.0	0.1	0.1	2.1	0.0	19
0.0	0.4	0.5	0.1	0.0	0.2	0.0	18
0.0	0.3	0.1	0.2	0.1	0.0	0.0	17
0.1	0.0	0.1	0.0	0.0	0.5	0.1	16
0.2	0.2	1.0	0.4	1.2	2.0	2.3	15
0.1	0.1	0.2	0.2	0.8	2.4	0.0	14
0.0	0.0	0.0	0.0	1.8	21.2	0.3	13
0.2	0.1	0.0	0.0	0.1	20.0	0.3	12
0.2	0.0	0.0	0.0	0.0	5.6	0.0	11
0.2	0.0	0.0	0.0	0.0	7.1	0.0	10
0.2	0.0	0.0	0.0	0.0	8.3	0.0	9
0.3	0.0	0.0	0.0	0.0	10.6	0.2	8
0.4	0.0	0.0	0.0	0.0	1.7	3.3	7
1.0	0.1	0.0	0.0	0.0	0.0	4.9	6
1.2	0.1	0.0	0.0	0.0	0.0	11.0	5
2.5	0.0	0.0	0.0	0.0	0.0	12.1	4
4.1	0.0	0.0	0.0	0.0	0.0	18.2	3
7.0	0.0	0.0	0.0	0.0	0.0	29.9	2
13.3	0.0	97.9	89.3	0.0	0.0	17.1	1
24.6	0.3	0.0	8.3	94.0	2.0	0.0	0
25.6	0.0	0.0	0.0	0.0	0.0	0.0	-1
18.5	98.2	0.0	0.0	0.0	0.0	0.0	-2
0.0	0.0	0.0	0.0	0.0	0.0	0.0	-3
18178	5506	12965	13364	18854	1088	4201	Total Points

Figure 2.4. An example of section divisions used to identify bole sections within a 1 m × 7 m × 25 m subset of a point cloud acquired from field plot node (40, 40) (a). The figure represents a marginal view of data points with X-coordinates between 40 m and 41 m (based on coarse registration to the field plot coordinate system.) Numbers in the table (b) represent the percentage of the total points in a column that fell into the corresponding 1 m cube divisions. Highlighted values are cells with the maximum number of points in each column. Circled values indicate seed cubes used to extract potential bole sections.

Because the initial lattice was fixed with no regard to actual stem locations, many viable bole sections were likely bisected by column boundaries. To address this possibility, horizontal repositioning, so as to enclose the maximum number of surface points within each cube, independently optimized the positions of seed cubes. Repositioning distances were limited to one half of the lattice grid cell size (or 0.5 m). The cubes were shifted horizontally creating new

boundaries centered on ($\bar{x}$, $\bar{y}$) of the points within the cube. The repositioning was repeated iteratively until the center of the cubes moved less than 5 cm between iterations. If re-centered seed cubes contained fewer than 100 data points they were eliminated from further consideration.

Once the viable seed cubes were repositioned, the original lattice was abandoned, and a new column of cubes was established above and below each seed cube, ranging from the ground buffer to the canopy top. So that leaning trees could be detected, every cube in the column was independently repositioned by the optimization method used for seed cubes, but relaxing the minimum required number of data points in each cube to 25. Although the cube repositioning was carried out independently among cubes in a column, it was expected that cubes would generally be horizontally repositioned within a limited distance of their neighbors above and below. The maximum allowable horizontal offset between consecutive vertical cubes was therefore limited to 0.5 m, corresponding to a maximum tree lean angle of 26.5º from vertical. The upper limit of viable bole sections was determined to be the height at which cubes no longer contained $\geq$ 25 data points.

The extraction of the bole section data sets was performed over the vertical range of the available data and therefore contained data points corresponding to the ground and/or overtopping vegetation. The extracted bole sections (EBSs) were trimmed vertically based on how quickly the number of points in vertically adjacent 0.5 m slices diminished. If a slice had fewer than 10 points or had a number of points that was fewer then 10% of the previous three slices the top or bottom of the bole section had been reached. Bole sections were limited to points between these end slices with an extra 0.5 m trimmed off both the top and bottom to ensure exclusion of the ground or overtopping vegetation from the bole section.

Bole sections could be selected more than once if they crossed a boundary between 2 or more columns, as was the case with the tree occupying the columns labeled 42 and 43 in Figure 2.4. Elimination of duplicate bole section was accomplished by checking whether, for any given height, the centers of cubes from different potential bole sections were within 1 m of each other. It was noted that the algorithm sometimes incorrectly classified areas of dense foliage or branches as bole sections, especially at heights above 10 m. To reduce such errors, potential bole section datasets containing fewer than 250 total points, or those consisting entirely of points above a height of 10 m, were eliminated from further consideration.

Surface points in a vertical series of repositioned cubes meeting the criteria listed above were assumed to correspond, potentially, to bole surface sections. The potential bole sections extracted from point clouds were assigned unique identifiers and stored electronically.

2.2.3 Matching bole sections between scans

Co-registration of a pair of scans required the matching of bole sections visible in both scans. This step was greatly aided by the coarse registration, which ensured that bole section XY coordinates approximately matched the corresponding trees' field plot coordinates (Figure 2.5). Inspection of bole section diameters, vertical extents, positions relative to other trees, and stem characteristics such as sweep, lean, crook or branching were used to verify bole section pairs suitable for use as control surfaces for image co-registration. Verification of bole sections' correspondence was sometimes aided by rescaling X and Z to exaggerate stem features (Figure 2.5B).

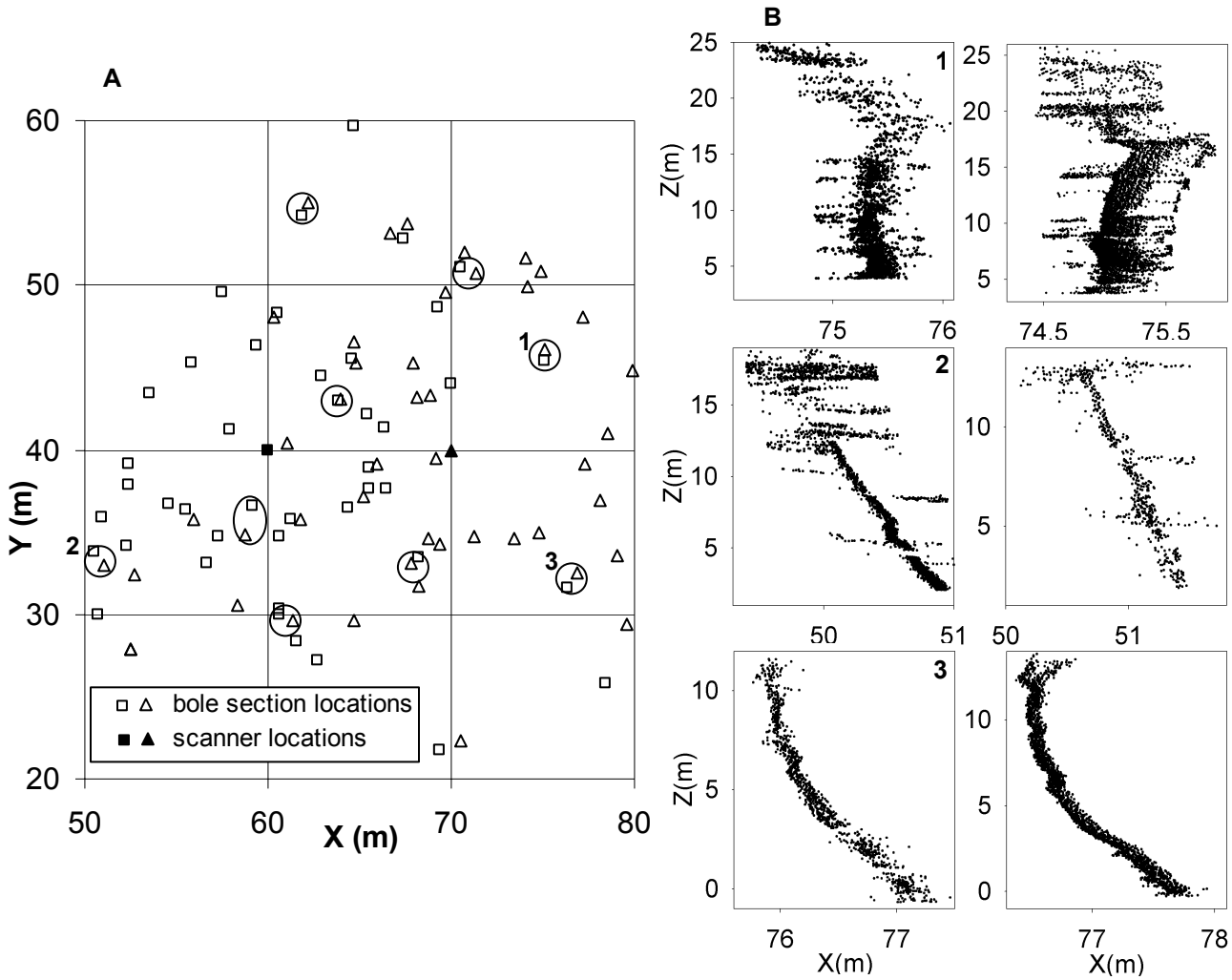

Figure 2.5. Bole section locations in the XY-plane from scanners located at nodes (60, 40) and (70, 40) with potential tree matches circled (A). Potential bole section pairs from circles labeled 1, 2, and 3 in (A) are compared in marginal XZ profiles (B).

The EBSs were subjected to a systematic analysis that selected matched bole section pairs with greater efficiency than could be accomplished by visual examination of graphs like those shown in Figure 2.5. The analysis primarily matched bole section pairs having close horizontal proximity across the coarsely registered coordinate systems. Similarity in section length served as a secondary matching criterion if many bole sections were in close horizontal proximity. Once the analysis identified bole section pairs, 2D and 3D scatterplots like those shown in Figure 2.5B were inspected to verify that the same trees were indeed selected from both scans. In general, 2 to 5 trees were selected for registering each pair of scans. The accuracy of the registration was greatly improved if the data for matched trees covered nearly the same vertical range of the scanned trees. Pairs of matched bole sections were selected to meet this

criterion when possible. Otherwise, the vertical extent of one bole section was cropped to better match the extent of its paired partner.

To facilitate evaluation of the bole section extraction algorithm distinctions were made between *potential* and *actual* bole sections. The potential bole sections were the output of the extraction algorithm, while actual bole sections were the subset of this output that were definitively identifiable as bole sections from visual examination of the individual EBS point clouds.

2.2.4 Iterative closest point method

The iterative closest point (ICP) algorithm of Besl and McKay (1992) was used to determine optimal parameters $\mathbf{A}$ and $\tilde{\mathbf{b}}$ for point cloud registration. ICP determined a set of "closest" points from the EBS point clouds, matching each point in one data set to the closest point (in Euclidian space) in the other. The ICP algorithm iteratively recomputed transformation parameters, re-determining closest point pairs and computing their distances at each iteration. When the change in mean closest-point distance fell below a specified threshold from one iteration to the next, the transformation parameters provided by ICP were considered optimal.

A requirement of the ICP algorithm is that one set of the paired point clouds to be aligned comprises a subset of the surfaces represented by data in the other, i.e., "inclusive segmentation" (Besl and McKay, 1992). Bole section extraction and matching provided the means of segmenting scenes for use as input to the ICP to algorithm. Inclusive segmentation posed no substantial challenge for range images obtained at a common node (Figure 2.3) because the overlapping regions of such scans contained data from a common viewpoint. (Note: the chief difference in scans 1, 2 and 3 made at a given plot node was a 60° azimuth rotation between the scans.) For example, if a tree were visible in the overlapping region of scans 1 and 2 from a given plot node, the same extent and distinguishing features of the tree bole would be visible in both scans. Such a tree would be an ideal candidate for bole surface segmentation and matching for use in the ICP registration algorithm.

In contrast, scans taken at different nodes acquired range data from different vantage points. This attribute made inclusive segmentation considerably more difficult to carry out with

any degree of reliability. For example, even though two range images acquired data characterizing the same tree, their respective point clouds represent different faces of the tree's bole surface. In the extreme, for a tree positioned directly between two plot nodes, the scans would characterize exact opposite sides of the tree's bole surface, making inclusive segmentation impossible. To overcome this difficulty, bole centers were estimated over the vertical extent of EBSs using the procedure described in section 2.2.7, Bole section center estimation.

The ultimate goal of registration was to register all scans to a single, global coordinate system. In contrast, ICP determines optimal transformation parameters only for point cloud pairs. Thus, additional processing was needed to register the dozens of images acquired to a single coordinate system. As previously noted, ICP segmentation requirements for scans from a common node were different than those to be aligned from different nodes. The following sections expand on the methods used to register all scans into a single coordinate system that matched the layout of the terrestrial gradient tree survey plot 218 at Coweeta.

2.2.5 Registration of scans from a common node

Following the coarse registration procedures described in section 2.2.1, a series of fine registration steps were carried out. The first step required "within-node" alignment of the two or three scans taken from a given node to a single coordinate system centered on the node at which the scans were made. Accomplishing this task resulted in a merged point cloud from each node that characterized the canopy space around the node location. This alignment required a single step for nodes at which two scans were made. Data sets comprised of the matched bole sections from both scans were supplied to the ICP algorithm, which then produced estimates of the transformation parameters $\mathbf{A}$ and $\tilde{\mathbf{b}}$ that gave the optimal alignment. A second alignment procedure was required for nodes at which three scans were made. A typical course of registering three scans, labeled 1, 2 and 3, acquired above a single plot node was conducted as follows. First, paired bole section data from scans 1 and 2 were provided as input to the ICP algorithm, which produced transformation parameters $\mathbf{A}_{2\to1}$ and $\tilde{\mathbf{b}}_{2\to1}$, where the subscript $2\to1$ indicates that the transformation aligned points from scan 2 with the scan 1 coordinate system. Second, paired bole section data from scans 3 and 1 were provided as input to the ICP algorithm, which produced

transformation parameters $\mathbf{A}_{3\to1}$ and $\tilde{\mathbf{b}}_{3\to1}$. All data points from scan 2, denoted as $\tilde{\mathbf{p}}_2$, were transformed using the transformation $T_{2\to1}(\tilde{\mathbf{p}}_2) = \mathbf{A}_{2\to1}\tilde{\mathbf{p}}_2 + \tilde{\mathbf{b}}_{2\to1}$ (cf. Eq. [1]). Similarly, data points from scan 3, denoted as $\tilde{\mathbf{p}}_3$, were transformed using the transformation $T_{3\to1}(\tilde{\mathbf{p}}_3) = \mathbf{A}_{3\to1}\tilde{\mathbf{p}}_3 + \tilde{\mathbf{b}}_{3\to1}$ (Eq. [1]). The resulting transformed data $T_{2\to1}(\tilde{\mathbf{p}}_2)$ and $T_{3\to1}(\tilde{\mathbf{p}}_3)$, now aligned with the scan 1 coordinate system, were merged with data points from scan 1, denoted $\tilde{\mathbf{p}}_1$, to generate a complete node-level point cloud characterizing the aboveground vegetation around the node.

It should be noted that the scan 1 coordinate system at this point had only been crudely aligned to the plot X-, Y-axes based on field notes. Further, no efforts had yet been made to align Z coordinates to a global reference elevation. Therefore, because the transformations $T_{2\to1}(\tilde{\mathbf{p}}_2)$ and $T_{3\to1}(\tilde{\mathbf{p}}_3)$ were both aligned with the scan 1 data, they were not yet globally registered. Additional registration step necessary to accomplish global alignment will be described below.

Originally it was intended that all registrations be performed using stem centers but it was determined that too few center points could be estimated for bole section pairs from leaf-on data. The leaf-on within node registrations were performed using bole section surfaces while the leaf-off within node registrations were performed using bole section centers.

2.2.6 Registration of data from different nodes

The "between node" registration of point clouds from different plot nodes required addressing several details not faced when registering scans from a common node. Bole section matching was considerably more challenging for a number of reasons. First, stem profiles varied in appearance from different vantage points, which hindered visual matching of bole section surfaces. Second, trees visible from one vantage point were, in many cases, partially or completely hidden from another vantage point by interfering vegetation. Third, point densities on a particular tree's bole surface were invariably higher when scanned from one vantage point or another, depending on the tree's distance from the respective scanner positions. Fourth, as noted previously, inclusive segmentation of bole surfaces was generally not feasible since different faces were characterized in point clouds acquired from different vantage points.

Between node registration proceeded using the merged node-level point cloud data sets. The merged point clouds were treated as units for between node registration, i.e. a unique transformation involving $\mathbf{A}$ and $\tilde{\mathbf{b}}$ was needed to align one node-level (merged) point-cloud to another. As in the "within-node" registrations, between node alignments were carried out in pairs. Figure 2.6 illustrates the progression of pair-wise registrations, with arrows indicating the directions of transformations. For example, the merged point clouds from the plot's leftmost nodes (30, 30), (30, 40), and (30, 50) were all transformed, one at a time, to the coordinate system of node (40, 40). In turn, the node (40, 40) point cloud was registered to the plot's central node (50, 40) coordinate system. Thus, aligning the leftmost nodes' point clouds to the central node's coordinate system required primary and secondary transformations applied in series. The registration scheme (Figure 2.6) meant that primary and secondary transformations would be necessary for the smallest number of scans, thereby minimizing the potential for registration errors to propagate (Blais and Levine 1995, Bergevin et al. 1996).

Prior to the between node alignment, the bole section extraction algorithm was reapplied to each node-level point cloud, with the expectation that the merged point-clouds from each node would yield a greater number of bole sections for use in between node registration than any of the individual scans. Further, because of the difficulties in achieving inclusive segmentation with scans acquired from different vantage points, bole section surfaces could not be used directly in the ICP algorithm. Instead, collections of points representing the geometric centers of boles at numerous points up the stem were estimated to serve as control points for ICP alignment.

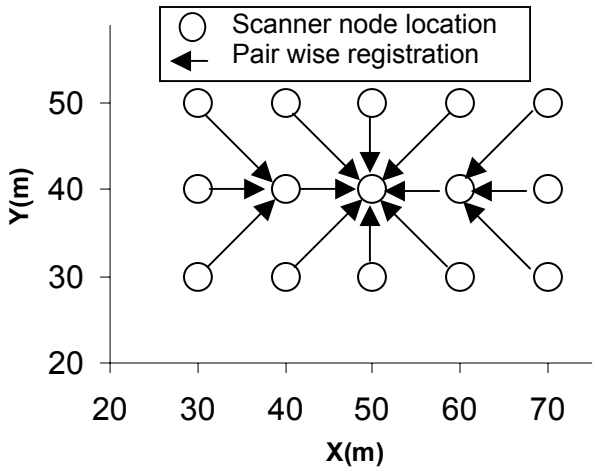

Figure 2.6. Direction of pair wise registration for node-level datasets comprised of two or three registered scans per node.

2.2.7 Bole section center estimation

Assuming that tree boles are approximately circular in cross-section, it was possible to identify the geometric centers of tree cross-sections at various heights above ground. For range data spanning relatively thin horizontal layers, tree cross-sections appeared as arcs with convex surfaces facing the scanner. For example, the arc shown in Figure 2.7 is comprised of 100 range measurements from a single scan that intercepted a bole in a horizontal band roughly 1 cm thick and 0.5 m above the ground. Such data are referred to as “bole-slice surface data”.

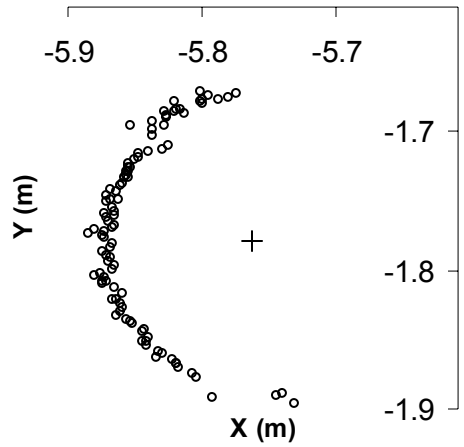

Figure 2.7. Point cloud data for a 1 cm bole cross-section [0.5 m ≤ z ≤ 0.51 m] of a tree in the Coweeta field plot. Coordinates shown are relative to the scanner origin, and the estimated arc center is marked by a (+).

To estimate the geometric centers of bole slices the following procedure was automated:

1. Extract a slice of bole data consisting of an initial number, n_s, of surface points $\{x_i, y_i, z_i\}$, where $i = 1, 2, \ldots, n_s$;

2. Estimate the arc center (x_c, y_c) that gives a minimum VAR(d) where:

$$d_i = 2\left(\left(x_i - x_c\right)^2 + \left(y_i - y_c\right)^2\right)^{1/2} \quad [3]$$

3. Check whether $\sqrt{VAR(d)} \leq \varepsilon$ or $n_s \leq n_{min}$, where ε is a tolerance parameter generally set between 1 and 5 mm, and n_{min} defines the minimum number of surface points that could adequately represent an arc-shaped bole slice surface.

    a. If neither condition is met, proceed to step 4

    b. If $n_s \leq n_{min}$, discard slice, proceed to step 5

    c. If $\sqrt{VAR(d)} \leq \varepsilon$ store (x_c, y_c), $\bar{d}$, and VAR(d) information, proceed to step 5;

4. Remove the sample point d_i with maximum $\left|d_i - \bar{d}\right|$, decrement n_s by 1, and proceed to step 2;

5. Move up stem to next potential slice, proceed to step 1.

To accomplish step 1 the set of possible tree surface points were sorted in order of ascending height (Z). The procedure started at the lower end of a given bole section and proceeded upward. A variable slice thickness was used, setting the initial $n_s = 100$ to ensure adequate representation of arcs along the stem. As point density decreased up the stem, i.e. further from the scanner, slices included a larger range of Z coordinates to achieve the same initial n_s for all slices. In some bole slice sections $\sqrt{VAR(d)}$ was relatively large, e.g., ≥ 5 cm. This generally indicated the presence of foliage, branches, deformities or other interference preventing precise extraction of an arc-shaped cross-sectional slice. Center estimates from such sections were not used for image registration.

Center points (x_c, y_c) in step 1 were found by computing the Euclidean distance between the *i*-th point in the arc (x_i, y_i) and the arc center, then finding the center coordinates (x_c, y_c) that minimized the variance VAR(d). For the cross-section illustrated in Figure 2.7, the standard deviation of d for the estimated center (-5.763, -1.779) was 4.8 mm, with an average arc diameter $\bar{d}$ = 21.8 cm. It was often useful to remove data points with d_i that varied considerably from $\bar{d}$ to improve the precision of arc center estimates (step 4). Doing so reduced errors due to instrument inaccuracies and stem defects. It also eliminated points representing objects apart from the main stem including branches or foliage. This "noise reduction" step sequentially removed the points that deviated most from a fitted arc until $\sqrt{VAR(d)} \leq \varepsilon$. Setting ε to a small value, such as ε = 1 mm, generally ensured that the reduced set of arc points represented bole measurements not affected by obvious deformities or instrument errors. A slice was discarded when a suitable center could not be found after reducing the number of sample points to n_{min} (step 3), which was generally set to 20. The algorithm continued processing non-overlapping slice sections up the bole until no further suitable slices could be identified.

2.2.7.1 Interpolation of stem center data

The use of stem centers greatly reduced the number of control points to be used for ICP registration. The collections of center points provided a convenient "surface" common to both point clouds. Further, it was assumed the center points would be relatively unaffected by which bole face was used to estimate their positions. Inclusive segmentation was impeded, however, when center points could not be estimated consistently over the vertical extents of bole sections in different scenes. Among the reasons for such inconsistencies were obstructions of bole surfaces by interfering vegetation, and branches or defects occurring on only one side of a tree stem. Differing surface point densities due to differences in scanner positions relative to target trees also limited precise matching of surfaces. To ensure inclusive segmentation in such cases, additional bole center points were generated in both data sets by linear interpolation of the estimated center point XY positions. The interpolations were at 1 cm vertical intervals and covered a Z-range of –5 m to 30 m.

Interpolated points were estimated using least squares linear regression, when multiple center points were present in a 1cm slice centered at the height of interpolation. Otherwise, interpolated coordinates were placed on a line connecting the nearest stem centers above and below the height of interpolation. The interpolation was extended beyond the vertical ranges of most extracted bole-sections to span the full range of bole-section lengths observed. Points extending above and below the observed bole sections' centers were assigned the XY coordinates of the nearest stem center-point in the vertical direction.

2.2.8 Application of ICP to bole centers

Registrations were performed by aligning a collection of non-interpolated stem centers from one node to a collection of interpolated stem centers from another node. As with the within-node registrations, analyses were carried out to verify that the collections of stem centers did, in fact, represent matched sets from identical trees characterized in the different point clouds. Together, these steps insured that the required condition of inclusive segmentation was satisfied.

For each pair of node-level point clouds to be registered, two alignment solutions were possible, depending on which of the center-point collections was subjected to the interpolation procedure. Both were calculated and the transformation with the smaller mean distance between closest points – a summary statistic provided by the ICP algorithm – was chosen as the optimal registration for that pair of nodes. In cases where the optimal registration transformation followed a path opposite the plan established in Figure 2.6, the inverse transformation $T^{-1}\left(\tilde{\mathbf{p}}\right)$ was applied to reverse the direction of alignment.

$$T^{-1}\left(\tilde{\mathbf{p}}\right) = \mathbf{A}^{-1}\left(\tilde{\mathbf{p}} - \tilde{\mathbf{b}}\right) \qquad [4]$$

The interpolation procedure allowed each stem center point in one point cloud to be paired with a center point in the other point cloud, even when center points were not found at identical vertical positions along the bole.

2.2.9 Ground surface registration

ICP was vulnerable to convergence on transformation parameter estimates that gave locally, rather than globally, optimal solutions (Besl and McKay 1992, Chen and Medioni 1992). Coarse registration and the spatial dispersion of bole sections generally prevented this type of registration error in X- and Y-directions; however, such errors in the Z-direction were sometimes noted. A simplified example of this phenomenon would be encountered in registering one cylinder to a cylinder that is taller in height. In this case a number of different registrations could be calculated that resulted in the same final mean distance between closest points but resulted in the shorter cylinder being situated at a number of different heights relative to the taller cylinder. Bole sections are not perfect cylinders, having defects and taper, but by using stem centers the taper of the tree surface is not included and the defects are minimized resulting in mismatching of the vertical position of one scan relative to another.

Following the scan and node-level registrations some inconsistencies in ground elevations were noted that were the result of slight tilting of one node-level point cloud relative to the others. Given the limitations of the tripod leveling system, such tilting seemed likely to have occurred. Thus, the inconsistencies increased with increasing distance from the scanner. The tilting and vertical position errors were mitigated by a final ground surface registration step.

The first step in performing the registration using the ground surface was to estimate the ground height around each node. The methods used to estimate the ground height were later expanded to create a digital terrain model (see section 2.3.1). Methods used to estimate ground height from scanner data are often used to create terrain models and generally involve the creation of a raster type data set by summarizing and filtering the point cloud data (Thies et al. 2004). In general these methods begin by dividing the area of interest into a regular grid and establishing the ground as the lowest point in the Z-direction in each cell, with filters being applied to ensure that only points representing actual ground returns are used.

For ground surface registration a raster data set was created using a 1 m × 1 m grid cell size. This cell size was chosen to ensure that ground surface returns were available in an adequate number of cells to facilitate registration. For each node the area of interest was a square area, 30 m on each side, centered on the node coordinates. This area for the node-level DTMs

was selected to provide adequate overlap between the node-level DTMs while focusing on the areas closest to the scanner where the greatest density of returns are located. The unfiltered node DTMs consisted of 900 cells.

A filter was applied to the point cloud data to eliminate points obtained near the scanners' azimuth limits. The scan margins in the azimuth direction can have a low point density and points scanned in these margins had a relatively low likelihood of representing a return from an interception with the ground surface. Initial estimates of the ground height were created with each cell being assigned the Z-value of the lowest point from the node point clouds that fell within that cell.

An initial cone filter was applied to the ground height estimates to eliminate inaccurate heights (Thies et al. 2004). The cone originated from the center of the cell with the lowest overall height value for a given node. This value was assumed to be an accurate representation of the relative elevation of the terrain at that particular XY location. The cone was defined as the volume above a 75% slope from the center of this cell. Any ground height values falling within this cone were removed from the data set.

In viewing the DTMs at this stage it was possible there were still a number of inaccurate cell heights well above the surrounding terrain. It is likely that occlusion by foliage or tree stems prohibited the ground from being visible from the scanner's vantage point. Planes fit to the 30 m × 30 m ground height data sets were used in a final filter. This type of filter assumes a uniform slope and eliminates points not within a certain range of this plane. For each node an equation to estimate the height of the plane ($\hat{Z}$) was determined. The equations were fit using the XY coordinates and the height (Z) of each cell. Linear least squares regression was used to estimate parameters of Eq. [5] for each node-level DTM:

$$\hat{Z} = b_0 + b_1 X + b_2 Y \qquad [5]$$

The residuals and standard error were calculated from the fitted regression. Only points with positive residuals > 1 standard error, meaning they were above the estimated plane, were considered to be misrepresentations of the ground surface and were eliminated from the node DTM. Points below the plane were ignored because it was assumed that no cell height values were obtained that were lower than the actual ground. The planes were refit with the reduced

data sets, iteratively eliminating data until the maximum residual for a plane was < 2 standard errors above the plane, or the standard error was < 1.5 m. A standard error of 1.5 m means that the average cell had a value that was 1.5 m from the fitted plane. The overall terrain on the plot was convex meaning that this threshold had to be higher than it would be for flat terrain.

The final node-level DTMs had a number of cells with no height data. To ensure inclusive segmentation for the ground registrations the matched data sets consisted of the cells having estimated height values for the same XY-values in the ground height data sets from both nodes. The matching of the leaf-off ground height data sets proved problematic due to the limits of the scanner coverage. It was determined that too few ground surface cells were matched between nodes and ground registration of the leaf-off scans was not possible. However, the tilting problem was not as common or pronounced using the leaf-off data likely due to the higher resolution and reduced occlusion of the leaf-off scan data facilitating more accurate registration in previous steps.

The ground registrations were performed for the leaf-on scans by converting the matched raster data sets into XYZ point clouds where the X- and Y-values were the cell centers and the Z-values were the heights assigned to each cell. The ICP algorithm was then applied using the matched ground height point clouds to estimate the registration parameters. The order of node-level ground registrations were the same as that used in the between node registrations (Figure 2.6).

2.2.10 Registration to plot coordinates

Upon completion of the full sequence of pair-wise registrations, all of the individual scans point clouds were aligned to the coarsely registered scan 1 acquired from the field plot center node (50, 40). A diagnostic was necessary to determine the accuracy of the coarse registration of this scan and evaluate the need for adjustments to align the scanner locations and node locations. Scanner and node locations were nominally aligned during data collection, so XY scatterplots of field plot node locations and scanner locations from the registered data sets served as the alignment diagnostic. If adjustments in alignment were deemed necessary, horizontal translations and/or rotations about (50, 40) were calculated that minimized the

distance between scanner locations in the registered data and the node locations. The adjustments were applied to the collections of registered leaf-on and leaf-off point clouds.

2.3 Summarizing point cloud data

It would be possible to combine all the registered scans from December (leaf-off) and August (leaf-on) respectively into plot-level point clouds comprised of 3D range measurements of the aboveground structure within the 20 m x 40 m field plot. However, these data sets would be difficult to manage, each consisting of nearly 30 million range data points and requiring nearly 2 gigabytes of computer storage space. Combining the data sets into these plot level point clouds would also eliminate the information provided by knowing where the pulses corresponding to each point originated.

Summaries were needed to reduce the computational burden of working with all the data at once, and to extract meaningful information for interpretation and comparison to objects and surfaces in the real world. The summaries incorporate information about the location and orientation of the scanner from which each point was captured. The following procedures were developed to summarize the registered point cloud data.

2.3.1 Creating a digital terrain model

A model of the local terrain elevation was needed to establish the lower limit of aboveground vegetation, and for calculating heights above ground of the various canopy elements, including tree and canopy heights. Previous research has demonstrated the utility of generating digital terrain models (DTMs) from airborne and ground-based lidar measurement instruments (Popescu et al. 2002, Thies et al. 2004). Here these models will serve as vertical boundaries for the distribution of canopy surfaces.

The DTM for plot 218 was developed using the method described in section 2.2.9, Ground surface registration, with minor changes to facilitate the use of data from multiple scans and to ensure elevation estimates were available over the entire extent of the plot. A relatively fine grid size of 0.25 m × 0.25 m was made possible by the large number of available points

characterizing the ground surface in the merged data sets. The lowest Z-value in each grid cell from any scan was established as the ground elevation within that cell.

A cone filter was applied, in this case originating from the lowest cell within the plot and using the same 75% slope limit as described previously. Plane filters using Equation [5] were fitted to the grid data characterizing 5 m × 5 m subsections, or panes, of the plot. The panes were non-overlapping and completely covered the plot area. Cells with residual values greater than 1 standard deviation of the residuals were eliminated and the equation for each pane was refitted. As in the previous application, this refitting procedure continued iteratively until the maximum residual for a pane was less than 2 standard errors, or when the standard error was less than 1.5 m. This threshold value reflects the curved nature of the terrain, which was evident in plots of the residuals.

Following filtering, any missing grid cell values were assigned the average elevations of the nearest eight grid cells. The high density of the point cloud from all cells resulted in less than 25 cells requiring the elevation assignment. The resulting DTM consisted of elevation values for all grid cells within the field plot, and a buffer extending 5 m beyond the plot boundary for the leaf-off scans. The buffer extended 10 m for leaf-on scans. Because buffer zones characterized ground surfaces targeted by fewer scans than the plot interior, they provided a means of evaluating the number and resolution of scans needed to accurately create DTMs.

2.3.2 Creating a canopy height model

Spatially explicitly canopy height models (CHM) have proven useful in a number of forest ecosystem research applications. CHMs are often produced from airborne lidar acquisitions (e.g., Popescu et al. 2002, Næsset 1997). Typically a CHM is estimated as the difference between a canopy top surface model (CTSM) and a DTM (Popescu et al. 2002). The CTSM in this case was computed from the largest vertical measurements over a regular grid of 0.25 m × 0.25 m to match the DTM resolution. Buffers were extended 5 m and 10 m outside the plot boundaries to match the leaf-off and leaf-on DTMs, respectively.

An initial CTSM, computed using the maximum Z-values in each grid cell, revealed a small number of cells with pulse returns that occurred well above the surrounding canopy. The

problem was more evident in the leaf-on scan data, where approximately 5-10 such points were noted. The false returns were eliminated from the point-clouds used to calculate the CTSM. The final CHM was computed as the difference between CTSM and DTM elevations over each grid cell within the plot and surrounding buffers.

2.3.3 Reclassifying point clouds into cubes

A straightforward method of summarizing the global point cloud was to divide the scan space into a regular lattice of 3D cells – in this case cells were specified as cubes – counting the number of points intercepting vegetation surfaces within each cube. Recognizing that such a summary would discount a great deal of the information contained in the point cloud, additional information was compiled and preserved for each cube. The directional nature of laser scan range measurements implies that no vegetation resided at any point along the line of sight between the scanner and the pulse's point of interception; accordingly the point cloud contained a great deal of information about open spaces in the canopy. The open space information was preserved by noting, for each cube, 1) the number of pulses that passed completely through the cube, 2) the number of pulses that were intercepted within the cube, and 3) the number of pulses that did not pass through the cube because they were intercepted at a range short of it. Pulses subject to condition (1), (2) and (3) were classified, respectively, as "pass-through," "intercepted," and "obstructed" pulses.

Five-meter buffers around the interior plot were maintained. The volume of cubes analyzed consisted of the space bounded by the outer-edges of 5 m buffer strips, with vertical limits defined by the DTMs and CTSMs. In order to determine the number of intercepted, pass-through and obstructed pulses for any cube it was necessary to know the points of origin and interception of each data point. Points of interception were extracted directly from the global point cloud, while points of origin were defined by the scanner position, registered in the global coordinate system. Pass-through counts included pulses that were not intercepted by determining their path from the spherical coordinate data.

Scanner positions, the point cloud of intercepted pulses, the CTSM and the DTM were provided as input to an algorithm that calculated the number of pass-through, intercepted, and obstructed pulses for cubes in the canopy space. This was accomplished using a straight-line ray

tracing technique that connected the origin and interception point of each laser pulse. Rays were extended beyond their interception points to the height of the CTSM or plot boundary in order to determine and count the number of obstructed pulses represented in each cube.

Cube summaries were stored electronically as a set of globally-registered XYZ coordinates indicating the geometric center of each cube, i.e. cube position, and the number of pulses classified as pass-through, intercepted, and obstructed for each cube. Alternative cube sizes of 1 m, 0.5 m and 0.25 m on a side were compared to assess their utility in 3D maps of canopy structure, to assess how measurement and registration errors might affect the utility of the method, and to evaluate the computational requirements of each alternative.

2.3.4 Spatially explicit plant area and leaf area index estimates

Once the leaf-on and leaf-off collections of registered point clouds had been summarized into cubes, estimates of plant area index (PAI, m^2/m^2) were created for each cube using the methods of MacArthur and Horn (1969) and subsequently described gap fraction inversion methods (Gardingen et al. 1999). To estimate the PAI of any cubic cell Equation [6] was used.

$$PAI = -\ln(P/(P + I)) \quad [6]$$

Where:

P = the number of pulses passing through the cube

I = the number of pulses intercepted within the cube

Plant area index was calculated for each cube using Equation [6]. For cubes that were completely obstructed it was not possible to estimate PAI. The PAI was summarized in different manners to quantify the horizontal and vertical distribution of PAI. Estimation of PAI by cube assumed that PAI was homogenous within cubes. This assumption was more accurate with decreasing cube size. However, any cubes that were completely occluded resulted in underestimation of plot-level PAI. The appropriate cube size used to calculate PAI was evaluated based on the amount of occlusion per cube. Leaf area index (LAI m^2/m^2) estimates were obtained by subtracting the leaf-off PAI estimates from the leaf-on PAI estimate for each cube.

Horizontal distributions of PAI and LAI were obtained for the plot by summing the values obtained for each cube across columns, resulting in an estimate for each vertical column of cubes. Vertical distributions of PAI and LAI were obtained for the plot by averaging the values obtained at each height above ground. Those values were weighted by the proportion cubes sampled (i.e. containing intercepted or pass-through pulses) at that height relative to the maximum number of cubes in a height layer.

2.3.5 Stem map creation

The bole section extraction algorithm and the stem center estimation algorithm (sections 2.2.2 and 2.2.7, respectively) provided information that could be summarized as stem maps created from scanner data. A stem map was seen as a useful intermediate result. Comparing the scanner-derived stem positions to the Coweeta tree survey coordinates provided a way to verify the accuracy of registrations and point-cloud derived stem-mapping. Further, information on stem positions and diameters would be useful for creating a model of the potential light environment around individual trees.

The set of all bole sections used in the within node and between node registration procedures were assumed to represent actual trees and provided the information used to create the stem maps. The stem center estimates of these bole sections at an elevation of 1.37 m above the DTM provided measures of tree positions and estimates of diameters at breast height.

Each tree was represented by bole sections extracted from multiple scan- and node-level point clouds, with the alignments typically subject to some degree of inaccuracy. The average position of all bole sections representing a tree served as the “best” estimate of that tree’s XY-position. “Best” estimate diameters for each tree were determined from the breast-height slice from any of the extracted bole sections based on the greatest number of scan points. A single slice was used to estimate the diameter because many bole sections did not have slices at or near breast height.

3 Submitted manuscript: *Detailed Stem Measurements from Ground-based Lidar*

The following chapter is a complete manuscript titled, *Detailed Stem Measurements from Ground-based Lidar*, which was submitted in its entirety to *Forest Science* on February 12, 2005. The manuscript is currently in review. It is presented as an example application of ground-based laser scanning and includes applications of the stem center finder and registration algorithms used here. The results and methods regarding registration, stem center finding and measurement of individual tree parameters are directly relevant to the larger scope of this work.

Detailed Stem Measurements of Standing Trees from Ground-based Scanning Lidar

By: Jason G. Henning and Philip J. Radtke

Abstract:

A commercially available pan and tilt mount laser scanner was used to acquire data for subsequent 3D modeling and measurement of standing forest trees. Methods were developed for identifying trees in range images and co-registering range images acquired from different vantage points. Upper-stem stem diameters and branch heights derived from the range images were compared to measurements made following the felling of a small number of loblolly pine (*Pinus taeda* L.) trees. Tree identification assumed bole cross-sections were circular, estimating their geometric centers at successive heights up the stem. Tree center estimates at multiple heights were then used to co-register images made from different vantage points. Co-registration (X, Y) errors did not exceed 2.1 cm in any of the 18 pairwise registrations carried out. Results showed excellent agreement (average error < 1 cm) between the lidar-derived diameter estimates and caliper measurements for bole sections below the base of live crown. Less-accurate estimates (< 2 cm) were obtained for stem heights up to 13 m. Results indicated the potential for accurate assessment of branch or whorl heights using ground-based scanning lidar, with the greatest accuracy likely to be realized for branches near the base of the live crown and below it.

3.1 INTRODUCTION

Applications for object detection and modeling from range images have become widespread in fields as diverse as architecture, engineering, medicine, and military science (Besl et al. 1992; Fitzgibbon et al. 1997; Eggert et al. 1998; Stevens et al. 2000; Zhilkin et al. 2000; DeKruger et al. 2001; Huber et al. 2003). The interest in such applications is due, in large part, to the development and increased availability of three-dimensional (3D) scanning and imaging technologies. Laser scanning, also known as laser imaging, ladar (laser radar e.g., (DeKruger et al. 2001)) or lidar (light detection and ranging) scanning or imaging, is among the most common of these technologies in fields outside of medicine. With few exceptions, 3D object modeling from lidar imagery has dealt mainly with human-made objects and structures. Natural objects, especially trees and other vegetation, sometimes occlude objects or scenes of interest; thus, they are ignored or avoided. In some cases methods have been developed to filter vegetation and other natural materials from lidar scenes to gain better view of objects of interest (Hardie et al. 1998).

In contrast, our interests lie in the modeling and measurement of forest trees using ground-based lidar. While a variety of tree measurements can be readily obtained using existing nondestructive tools and techniques, there are some attributes that are exceedingly difficult to measure directly without employing labor-intensive or destructive methods. Among these are the accurate and detailed measurement of individual trees' upper stems and crowns (Clark et al. 2000). Detailed stem measurements provide a means of assessing volume content as well as understanding relationships involving tree growth, allometry, stem mechanics, and canopy structure (Dean 2004).

Our goal here was to adapt existing 3D imaging technology and methods for the measurement and modeling of forest trees. Emphasis was placed on the methods of tree identification in range images, co-registration of range images and subsequent measurement of stem diameters along tree boles. Our specific goals included 1) acquisition and merging of range images acquired from adjacent locations to provide 3D characterization of individual trees, 2) measurement of tree attributes from range images, and 3) comparison of lidar-estimated tree attributes with direct measurements made following felling of a small number of trees.

3.2 MATERIALS AND METHODS

a. Data acquisition

Data were acquired on May 28 and 29, 2003 in a 20-year-old loblolly pine (*Pinus taeda* L.) research plantation in the Appomattox-Buckingham State Forest (37° 23' N, 78° 38' W) in the Appalachian Piedmont of central Virginia, USA. Data collection efforts were coordinated with a harvesting operation so that destructive measurements of tree stems could be compared to measurements made with lidar images or "scans" obtained immediately prior to felling subject trees. Trees in the plantation had been planted in rows at regular spacings from 1.2 m to 3.7 m apart, allowing several stems to be captured in a single range image. Nine subject trees were marked with reflective tape for subsequent identification in range images. The scanner was placed at various positions around the targeted trees at distances of 2-7 m. Understory vegetation had been chemically controlled during the previous experimental treatments making the target trees highly visible. Scanning proceeded so that multiple marked trees were visible in every scan (Figure 3.1) Trees numbered 1-3 were scanned from four positions labeled A-D (Figure 3.1). Three other sets of scans were made using similar scanner arrangements around pairs of trees numbered 4-5, 6-7, and 8-9, respectively. The target trees' total heights, measured from tip to base with a tape after felling, ranged from roughly 16 m to 20 m, and their stem diameters, measured outside the bark at breast height (1.4 m), ranged from 13 cm to 30 cm.

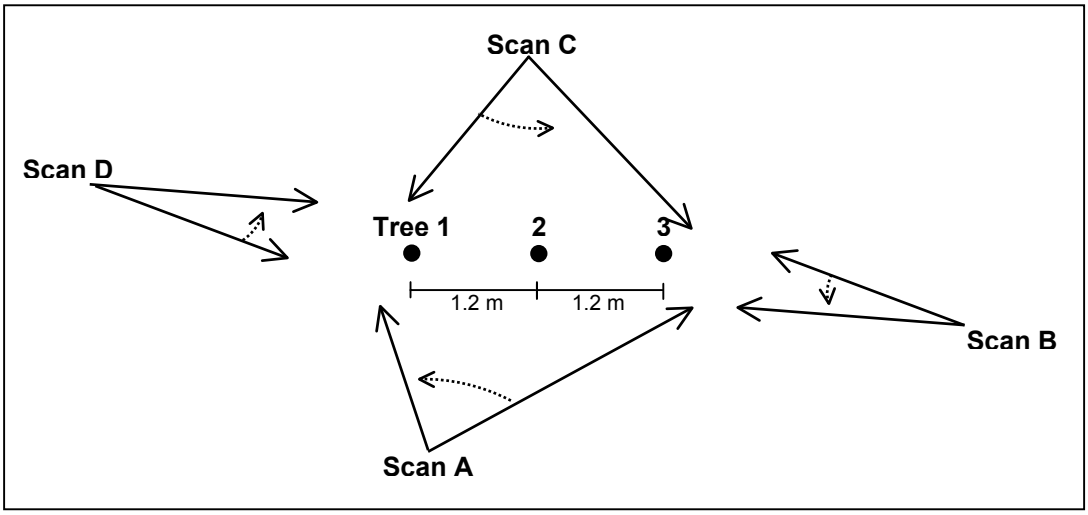

Figure 3.1. Arrangement of range image scans A, B, C and D with respect to subject trees 1-3. Solid arrows indicate angular extents of scans and dashed arrows indicate scan directions.

Figure 3.2. Scan C (Figure 3.1) laser pulse return intensity from three target trees in the foreground and a forest edge in the scene background. Tree movement due to light winds is indicated by vertical striae, especially high in the canopy where movement is greatest (left). Under calm conditions distortions are less apparent (right).

A motorized pan and tilt mount laser scanner model LPM-25HA distributed by Riegl USA Inc. (Orlando, FL) was used to acquire lidar images. The instrument was mounted on a standard surveyors' tripod at positions around subject trees as shown in Figure 3.1. Angular stepwidths of 0.054° (0.06 gon) in polar and azimuthal directions were used, corresponding to a scan footprint of roughly 8.5 x 8.5 mm at a distance 10 m from the scanner. For several hours during the afternoon, light winds caused visible distortions in the range images (Figure 3.2).

Additional scans were acquired after winds calmed in the evening to minimize wind effects on image quality. We continued collecting data after sunset because atmospheric conditions were ideal and the instrument required no ambient light to operate.

Since our interest involved only the target trees, we generally limited the extent of scans to include only the space immediately surrounding the target trees' stems. Doing so expedited acquisition of the range images. For example, the scene in Figure 3.2 ranged 36° in azimuth and 95° in the polar direction, with an angle step size of 0.054°, resulting in nearly 1.2 million range measurements. To further reduce the time needed for scan acquisition, we increased the angular step size by a factor of 1.6 (from 0.054° to 0.09°) when scanning target trees 6-9. Individual scan times varied, but generally required about 14-45 minutes per 1 million range measurements in a range image or "point-cloud" (LPM-25HA specifications at http://www.riegl.com/).

Stem diameter at breast height (dbh) was measured before felling the target trees. After felling, we made caliper measurements of stem cross-sectional diameter, outside bark, along two perpendicular axes at 1 m intervals up the stem. Total height was measured on the felled trees. Heights from the base of the trees to the first several live branches were recorded.

b. Data registration and analysis

Image registration is a process of transforming point-cloud data from individual scans, e.g., scans A-D in Figure 3.1, into a single Cartesian coordinate system. Registration is carried out by a 3D rotation and translation of point-cloud X,Y,Z surface data from the scanner's unregistered or "native" coordinate system to a target or "global" coordinate system.

$$T(\tilde{\mathbf{p}}) = \mathbf{A}\tilde{\mathbf{p}} + \tilde{\mathbf{b}} \qquad [7]$$

where

$T(\tilde{\mathbf{p}})$ = transformed (registered) surface point

$\mathbf{A}$ = 3 x 3 rotation matrix

$\tilde{\mathbf{p}}$ = untransformed surface point 3-vector from scanner point cloud

$\tilde{\mathbf{b}}$ = translation 3-vector

All surface points obtained in one range image are transformed by the same rotation matrix ($\mathbf{A}$) and translation vector ($\tilde{\mathbf{b}}$); thus, a unique $\mathbf{A}$, $\tilde{\mathbf{b}}$ transformation is needed for each

image to be registered. For this application it was not necessary to georeference point clouds to a real-world coordinate system. When mounted on the tripod, the scanner's Z axis was normal to the horizontal plane. Since the ground was level at the study site, any of the scans obtained could serve as a suitable target coordinate system for registration.

Accurate registration of lidar images generally depends on the extraction and matching of common surfaces or artificial control points in overlapping, unregistered scenes. The common surfaces or control points are then used to find $\mathbf{A}$ and $\tilde{\mathbf{b}}$. The extraction of common features is generally referred to as segmentation (Jokinen et al. 1998; Hetzel et al. 2001). Use of artificial control points, such as reflective targets, was deemed impractical here. To ensure accurate registration of surface points high in the canopy would have required the placement of targets several meters above ground. To avoid the difficulties of placing artificial targets we used tree stems as natural targets for use in scene co-registration, noting that the accuracy of the segmenting and matching of features would directly affect the accuracy of any registration based on such features (Besl et al. 1992).

Locating tree centers in range images

Stem surface matching was not possible, e.g., between scans A and C, because surface points were recorded from opposite sides of the main stems, or boles, of each tree (Figure 3.1). Instead we used the relationship between tree bole surfaces and their geometric centers to extract sets of control points for co-registration. We assumed that tree boles were approximately circular in cross-section and identified the geometric centers of bole cross-sections at various heights above ground. For range data spanning relatively thin horizontal layers, tree cross-sections appeared as arcs with convex surfaces facing the scanner. For example, the arc shown in Figure 3.3 is comprised of 130 range measurements extracted from a single scan that intercepted a bole in a horizontal band roughly 2 cm thick at a height 1.37 m aboveground. We refer to such data as "bole slice surface data".

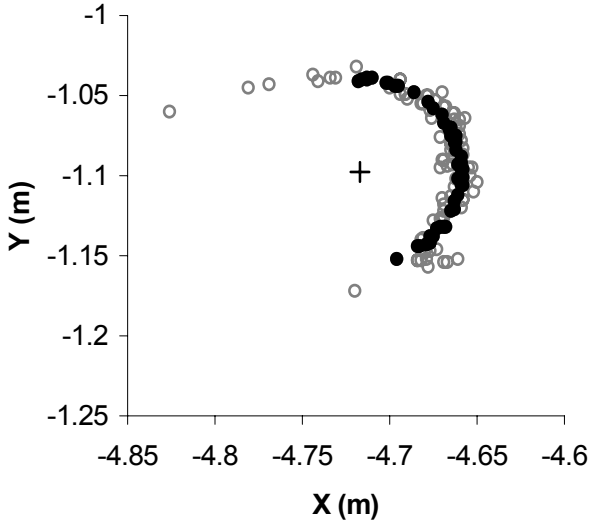

Figure 3.3. Surface data for a 1 cm bole cross section [1.36 ≤ z ≤ 1.38 m] for tree 2, scan B (Figure 3.1). The estimated arc center is marked by a (+). Solid symbols denote points used for arc-center estimation.

To estimate the geometric centers of bole slices the following procedure was automated:

1) Extract a slice of bole data consisting of an initial number of surface points, n_s, where $i = 1, 2, \ldots, n_s$;
2) Estimate the arc center (x_c, y_c) that gives a minimum variance VAR(d), where according to [8];

$$d_i = 2\left(\left(x_i - x_c\right)^2 + \left(y_i - y_c\right)^2\right)^{1/2} \qquad [8]$$

3) Check whether $\sqrt{\text{VAR(d)}} \leq \varepsilon$ or $n_s \leq n_{min}$, where ε is a tolerance parameter generally set between 1 and 5 mm, and n_{min} defines the minimum number of surface points that could adequately represent an arc-shaped bole slice surface.
    a. If neither condition is met, proceed to step 4
    b. If $n_s \leq n_{min}$, discard slice, proceed to step 5
    c. If $\sqrt{\text{VAR(d)}} \leq \varepsilon$ record (x_c, y_c), $\bar{d}$, and VAR(d) information, proceed to step 5;
4) Remove the sample point d_i with maximum $\left|d_i - \bar{d}\right|$, decrementing n_s by 1, and proceed to step 2;
5) Move up stem to next potential slice, proceed to step 1.

To accomplish step 1 we sorted the set of possible tree surface points in order of ascending height (Z) and started with points at the base of the tree. We used a variable slice thickness and initial n_s typically $100 \le n_s \le 150$ to ensure an adequate number of surface points for representing arcs along the stem. As point density decreased up the stem, i.e. further from the scanner, slices included a larger range of Z coordinates to maintain the same initial n_s for all slices. In some bole slice sections $\sqrt{\text{VAR(d)}}$ was relatively large, e.g., ≥ 5 cm. This generally indicated the presence of foliage, branches, deformities or other interference preventing precise extraction of an arc-shaped cross-section surface. Such slices were not used for image registration.

We found (x_c, y_c) in step (2) by computing the Euclidean distance between the arc's *i*-th point (x_i, y_i) and its center, then finding the center coordinates (x_c, y_c), by numerical optimization, that minimized the variance VAR(d). For the cross-section shown in Figure 3.3, the standard deviation of d for the estimated center (-4.717, -1.098) was 7.6 mm, with an average arc diameter $\bar{d}$ = 6.0 cm (open symbols). We often found it useful to remove data points with d_i that varied considerably from $\bar{d}$ to improve the precision of arc center estimates (step 4. Doing so reduced errors due to instrument inaccuracies and stem defects. It also eliminated measurements of objects apart from the main stem including branches or foliage. This "noise reduction" step sequentially removed the points that deviated most from a fitted arc until $\sqrt{\text{VAR(d)}} \le \varepsilon$. We found that setting ε to a small value, such as ε = 1 mm, generally ensured that the reduced set of arc points represented bole measurements not affected by obvious deformities, obstructions, or instrument errors. Bole-slice analysis following the noise reduction procedure resulted in an average arc diameter $\bar{d}$ = 5.8 cm for the data shown in Figure 3.3 (filled symbols). A slice was discarded when a suitable center could not be found after reducing the number of sample points to n_{min} (step 3b), which we generally made as large as practical based on trial values ranging from n_{min} = 10 to n_{min} = 55. The algorithm continued processing non-overlapping slice sections up the bole until no further suitable slices could be identified. Algorithm output consisted of scanner native X,Y,Z coordinates for the center of each slice analyzed, a Z coordinate estimated as the slice average surface-point height, the estimated stem slice diameter, and the n_s of each slice at convergence (step 3c).

ICP pair wise registration

The iterative closest point (ICP) algorithm of Besl and McKay (1992) was used to determine optimal transformation parameters $\mathbf{A}$ and $\tilde{\mathbf{b}}$ for point cloud co-registrations. Two data sets, one consisting of a tree's bole-slice center points from one scan and the other consisting of the same tree's bole-slice center points from a different scan, were input to the ICP algorithm along with starting values for the transformation parameters. ICP matched each center point in one data set to the closest center point (in Euclidian space) from the other, identifying the set of "closest" matching points between the two data sets. The ICP algorithm iteratively recomputed transformation parameters, evaluating the change in mean closest-point mean distance at each iteration. When the change in mean distance fell below a specified threshold, the transformation parameters were assumed to be optimal.

ICP was vulnerable to convergence upon transformation parameter estimates that attained local, rather than global, minimum mean distances between closest points (Besl and McKay 1992, Chen and Medioni 1992). Setting initial values for the transformation parameters based on reflective tape affixed to the stems at breast height (Figure 3.2) generally prevented this type of registration error in X and Y directions; however, such errors in the Z-direction were sometimes noted. We adjusted the vertical alignment of ICP-registered point clouds, where necessary, by comparing elevations (Z) of ground surface points in the scans at common X-Y locations.

ICP co-registration transformed one point cloud in the pair to match its partner point-cloud's coordinate system. Since georeferencing was not required for this application, the point cloud with the highest density of points on the tree of interest was chosen as the target coordinate system. Thus, pair wise ICP co-registrations aligning scans B $\rightarrow$ A, C $\rightarrow$ A and D $\rightarrow$ A would have effectively aligned all four scans of a tree to the scan A coordinate system.

3.3 RESULTS

Although four scans were made around each group of trees, one scan from each group was discarded due to obvious wind-caused distortions. To expedite work after sunset, we did not repeat all scans that had been affected by windy conditions earlier in the day. As a result only three useable scans were available for each of the nine trees; however, we retained the scan

labels A-D to indicate the scanner positions relative to target trees (Figure 3.1). Surface data set sizes for scans A-D and trees 1-9 varied due to the different scan angle stepwidths used, the different tree sizes, and differences in the distances between scanner and tree positions. Horizontal distance from the scanner to tree bole surface ranged from 2.5 to 7 m (Table 3.1). For 2 m long bole sections between 1 and 3 m above ground, the number of lidar sample points on each tree ranged from under 5,000 to nearly 78,000 (Table 3.2). On average, it required over 300 surface points to estimate each bole slice center in these bole sections. While we typically specified an initial $n_s = 125$ in the center-finding algorithm, fewer than half the slices resulted in useable center estimates based on acceptance criteria $\varepsilon = 1$ mm and $n_{min} = 55$.

Table 3.1. Scanner stepwidth (degrees), tree dbh (cm), height to live crown (HLC, m) and range from scanner to stem (m) for nine trees surveyed by a laser scanner placed at positions A-D around the trees.

Stepwidth	Tree	DBH	HLC	A	B	C	D
0.054	1	20	10.7	-	3.5	4.2	2.8
0.054	2	13.5	11.1	-	4.8	3.5	3.9
0.054	3	14.5	12.2	-	5.9	3.4	5.1
0.054	4	28.6	11.1	3	7	-	2.7
0.054	5	19.5	-	3.6	4.8	-	5
0.09	6	13.5	10.5	2.6	3.8	2.5	-
0.09	7	17.4	9.7	3.8	2.5	3.2	-
0.09	8	25	11.6	4.6	4.5	-	3.7
0.09	9	11.5	8.8	4.6	3.7	-	4.5

- denotes measurement not made or not used due to wind interference

Table 3.2. Numbers of surface points on 2 m long bole sections between 1-3 m aboveground and corresponding numbers of center points (ε = 1 mm, n_{min} = 55) for each bole section for trees 1-9 by laser scan position (A-D).

		Surface Points				Center Points			
Group	Tree	A	B	C	D	A	B	C	D
1	1	-	12,776	24,221	48,117	-	52	96	209
1	2	-	12,485	22,751	20,076	-	52	96	90
1	3	-	24,611	28,643	12,807	-	110	105	48
2	4	23,448	12,988	-	77,931	51	34	-	195
2	5	12,192	19,991	-	18,045	45	22	-	2
3	6	16,071	8,137	17,281	-	43	31	56	-
3	7	9,497	21,992	14,750	-	32	66	47	-
4	8	9,162	9,566	-	14,096	9	22	-	25
4	9	4,832	7,552	-	4,944	7	31	-	10

The n_{min} parameter provided a useful criterion for limiting the magnitudes of errors in bole slice center estimates. Similarly, the value of n_s at the completion of the center-finding algorithm provided a diagnostic for assessing the quality of the bole slice center and diameter estimates. Inspection of bole slices prior to and after culling of scan points in step 4 of the tree center finding algorithm indicated a correlation between final n_s and the reliability of center points (Figure 3.4). The examples illustrated in Figure 3.4 were based on a starting n_s = 125 and resulted in the n_s values listed in Table 3.3 following data point removals to reduce arc diameter standard deviations to ε = 1 mm. Comparison of final n_s values for many slices we examined indicated that the largest departures from caliper stem diameter measurements occurred when slice n_s was relatively small, e.g., $n_s \leq 30$ (Figure 3.4B). Increasing n_{min} had the effect of eliminating grossly inaccurate arc diameter estimates, but also reduced the number of estimated bole center points available for subsequent ICP registration. For example, the numbers of center points reported in Table 3.2 would have increased by about 1.5 times had they been based on a less restrictive threshold n_{min} = 25.

Table 3.3. Center-finding algorithm accuracy diagnostic (n_s) and comparisons of scanner arc and caliper diameter measurements (cm) at various stem heights from the four bole-slice cross sections of tree 5 from scan D shown in Figure 3.4.

Height (m)	n_s	Arc	Caliper	Error (cm)
1.32	37	16.8	19.5	-2.7
3.49	30	35.3	18.4	16.9
6.84	53	17.3	16.3	1
11.14	75	14.4	12.6	1.8

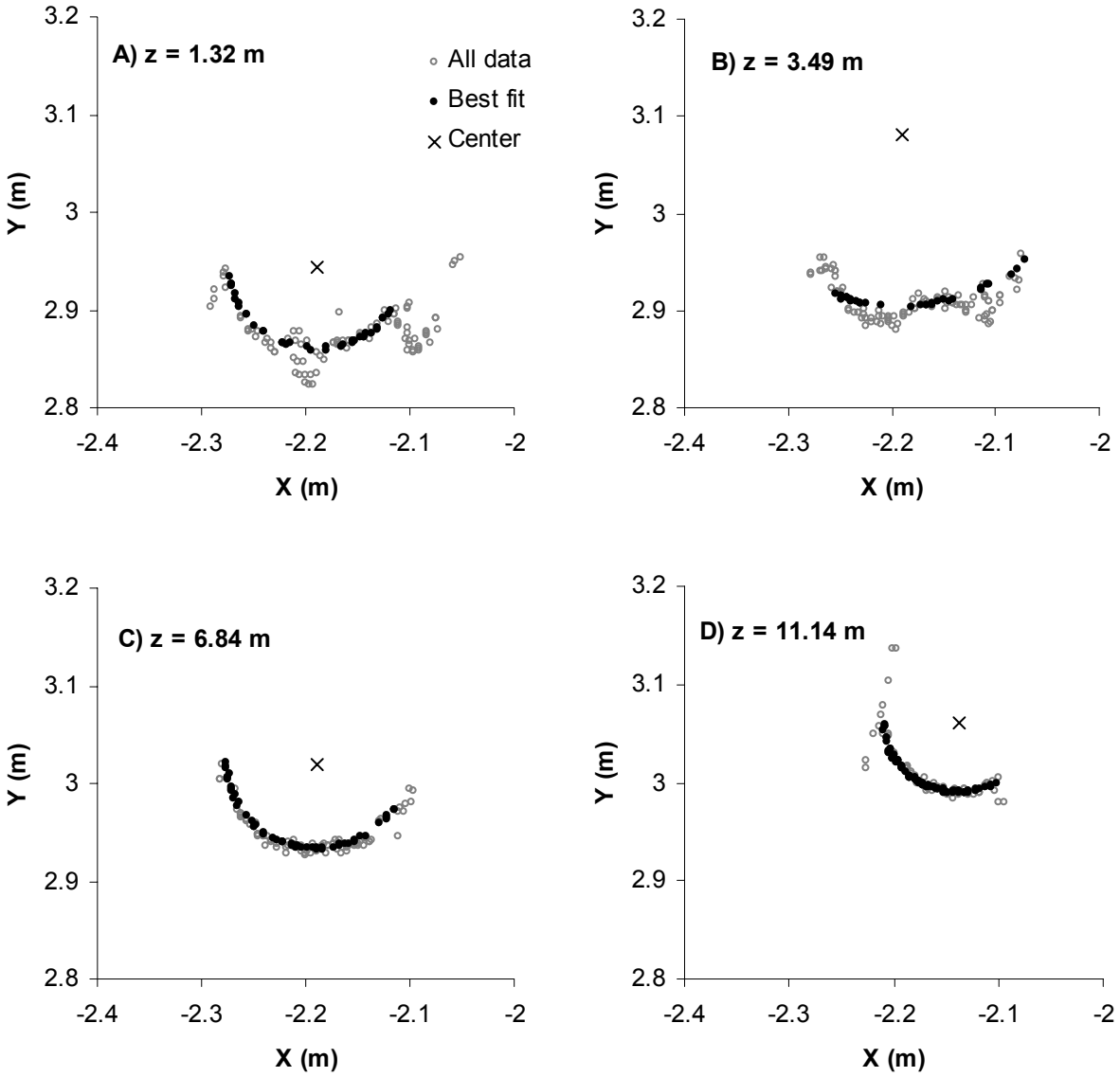

Figure 3.4. Bole slice data from four slices of tree 5 scan D and their corresponding center estimates. Surface points departing from an assumed arc-shaped cross-section were removed to find the center of "best fit."

Center points and stem diameters estimated by the center-finding algorithm showed general agreement with caliper measurements when the relatively strict criterion $n_{min} = 55$ was used (Figure 3.5). The n_{min} restriction left certain bole sections poorly represented in some scans. For example, the bole section between 1 and 3 m in scan D of tree 5 had only 2 estimated center points and none between 3 and 4 m (cf. Table 3.2, Figure 3.5). However, the goal in choosing center points restrictively at this stage of the analysis was to provide collections of center points

from each scan for use in the ICP range image co-registration. As the accuracy of ICP registrations was limited by the accuracy of center point estimates, registration accuracy was notably improved by choosing a large threshold for n_{min}.

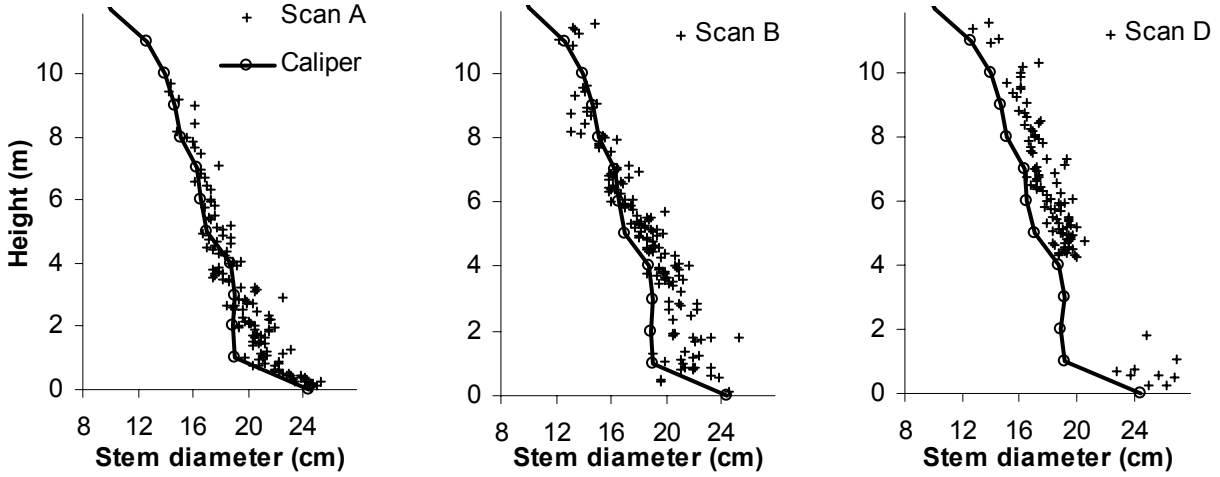

Figure 3.5. Stem diameter measurements from bole slices and calipers for tree 5, scans A, B and D.

For comparison, a value of $n_{min} = 10$ was used to estimate tree centers for the 27 scan-tree combinations. This threshold was sufficiently small so that almost all estimated center points resulted in a final $n_s \geq n_{min}$. Specifically, 11 of the 6,526 slices used resulted in final $n_s = 10$ and fewer than 2% resulted in $n_s < 35$. This "non-restricted" set of center point estimates was used to co-register scan pairs in what were in relatively inaccurate alignments (Table 3.4). In contrast, when the more restrictive threshold $n_{min} = 55$ was used, only 4,359 slices resulted in center estimates satisfying $n_s \geq n_{min}$. Although fewer in number, these center points were deemed to be more accurate and thus resulted in comparatively accurate ICP co-registrations.

Table 3.4. Co-registration statistics comparing unrestricted (n_{min} = 10) and restricted (n_{min} = 55) center point estimates for image co-registration: mean ($\overline{\delta}$) and standard deviation (s_δ) of post-registration tree-center paired point distances.

		Scan	Unrestricted		Restricted	
Group	Tree	Pair	$\overline{\delta}$ (cm)	s_δ (cm)	$\overline{\delta}$ (cm)	s_δ (cm)
1	1	B, C	1.5	1.5	0.9	0.7
1	1	B, D	1.3	1.0	1.0	1.4
1	2	B, C	2.0	2.6	1.5	1.4
1	2	B, D	3.6	12.1	1.3	0.9
1	3	B, C	2.7	3.4	0.7	0.4
1	3	B, D	1.6	2.1	0.8	0.6
2	4	A, B	2.2	1.6	1.0	0.5
2	4	A, D	1.5	1.1	1.1	0.9
2	5	A, B	4.9	2.4	0.7	0.7
2	5	A, D	2.5	1.5	0.7	0.6
3	6	A, B	2.4	1.8	1.0	1.2
3	6	B, C	1.2	1.4	1.0	1.1
3	7	A, B	3.2	3.4	1.2	0.6
3	7	B, C	1.2	1.4	0.8	0.5
4	8	A, B	1.0	0.6	0.9	0.5
4	8	A, D	1.1	0.9	1.0	0.6
4	9	A, B	2.8	4.2	0.9	1.1
4	9	A, D	2.2	2.4	2.1	2.9

To test the gain in registration accuracy achieved by eliminating the 33% of center points deemed least reliable according to the final n_s diagnostic, we computed a mean distance coefficient, $\overline{\delta}$, following ICP registration of bole-center data set pairs. To compute δ, a center point **p** from one data set was paired with the center point **p'** in its co-registered partner data set having the closest Z-value, i.e. points were paired that had approximately equal heights up the stem. The δ coefficient for the i^{th} tree center-point was computed as

$$\delta_i = \sqrt{\left(x_i - x_i^{'}\right) + \left(y_i - y_i^{'}\right)} \qquad [9]$$

where

x_i, $x_i^{'}$ = X-coordinates for paired tree center points **p** and **p'** in co-registered scans.

y_i, $y_i^{'}$ = Y-coordinates for paired tree center points **p** and **p'** in co-registered scans.

Restricting the center point data sets used for co-registration based on n_{min} = 55 reduced $\overline{\delta}$ following ICP registration by an average of 43%, with a similar magnitude in the reduction of

the standard deviation of δ, s_δ (Table 3.4). Graphical inspection using 2D and 3D scatter plots of co-registered tree centers and registered bole slices confirmed that registrations were in most cases slightly but adversely affected by inaccurately estimated center points.

The $\mathbf{A}$, $\tilde{\mathbf{b}}$ transformations for each scan pair listed in Table 3.4 were applied to the entire set of surface points characterizing the respective trees. For example, the transformation parameters $\mathbf{A} = \begin{pmatrix} 0.4520, -0.8919, -0.0106 \\ 0.8920, 0.4520, 0.0063 \\ -0.0008, -0.0123, 0.9999 \end{pmatrix}$ and $\tilde{\mathbf{b}} = \begin{pmatrix} -5.3712 \\ 2.4641 \\ 0.1927 \end{pmatrix}$ were used to register surface points from tree 1, scan C to the coordinate system of tree 1, scan B. Another transformation was applied to register tree 1 surface points from scan D to the scan B coordinate system. Complete 3D surface scans for each tree were thus obtained. The number of surface points in combined, registered datasets for trees 1-9 varied considerably from a minimum of fewer than 60,000 to nearly 346,000 (Table 3.5).

Table 3.5. Numbers of surface points and estimated center points from 3 combined, registered scans per tree (n_{min} = 35, ε = 1mm).

Tree	surface pts	center pts
1	266,299	1,677
2	74,042	1,101
3	215,527	1,185
4	345,992	1,207
5	178,177	553
6	122,326	641
7	140,408	666
8	111,696	215
9	58,880	201

Stem diameter profiles, i.e. graphed or tabulated stem diameter versus height, were estimated by reapplying the stem center-finding algorithm to tree surface data following scan co-registration. Diameter estimates from the unregistered scans were used to exclude data points far from tree centers prior to reapplication of the center-finding algorithm. This improved the ability of the algorithm to accurately estimate stem centers and diameters, reducing errors caused by interference from branches and foliage apart from the main stems. A smaller threshold n_{min} = 35 was used, which increased the ratio of estimated center points to surface points, about 1 to 200, as compared to the individual scan results based on n_{min} = 55 (cf. Table 3.2, Table 3.5). Despite

the smaller n_{min} parameter, diameter estimates from the combined scans were less variable than those obtained from individual scans; however, neither were necessarily unbiased (e.g., Figure 3.6).

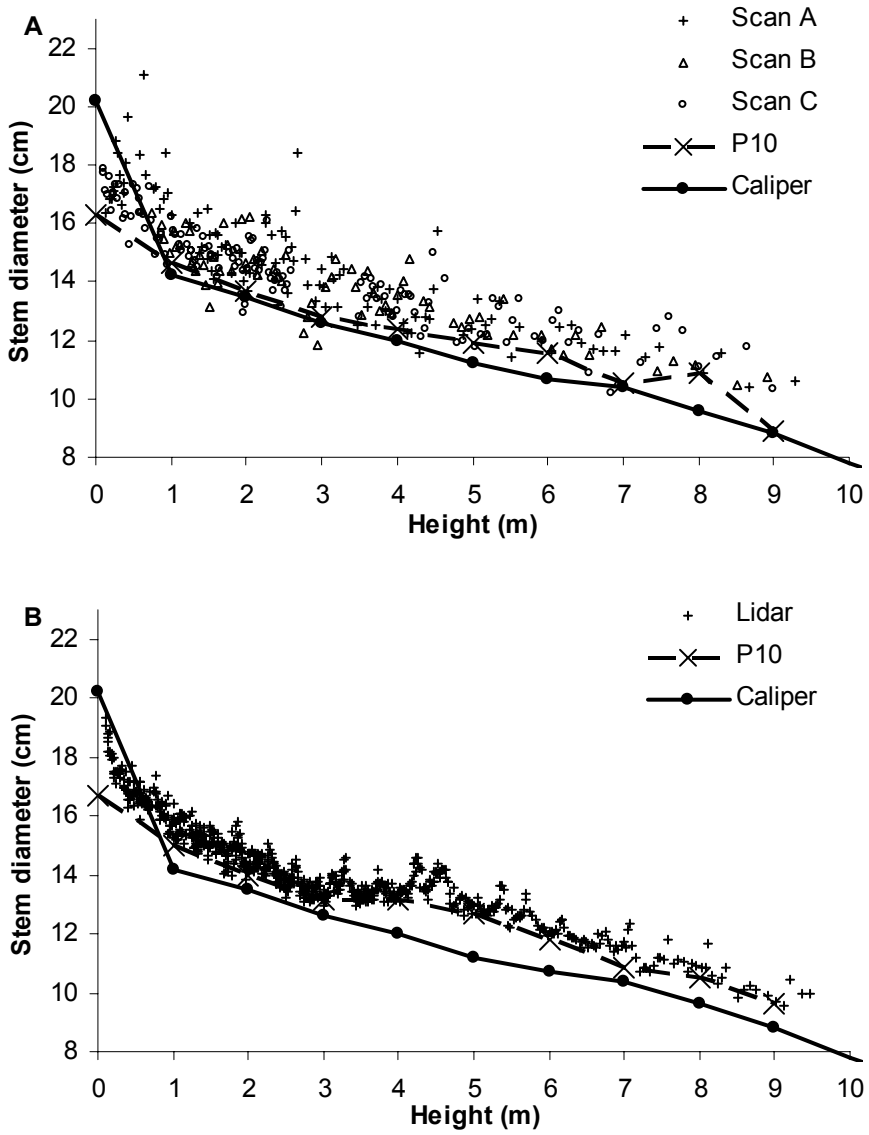

Figure 3.6. Tree 6 lidar-derived stem diameter estimates from individual (A) and combined (B) scans. Caliper measurements and tenth percentiles (P10) from scan data are superimposed.

Examination of stem cross sections in the point clouds revealed surface point measurements more often appeared outside tree surfaces than inside them (Figure 3.3, Figure 3.4). Accordingly, diameter estimates from laser scan data tended to be larger than caliper measurements (Figure 3.5, Figure 3.6). To account for this apparent bias we estimated stem

diameter profiles based on tenth-percentiles (P10) from binned stem diameter point estimates. For comparison to caliper measurements the lidar based point estimates of diameter were binned into 1 m height intervals. A P10 value was determined for every 1 m bole section (Figure 3.7). Ground-line diameter P10 values substantially underestimated caliper ground-line diameters (Figure 3.7, △). The P10 estimate for tree 5, height = 12 m was evidently affected by a fork in the stem at height 11.7 m (Figure 3.7 x). Excluding these inaccurate measurements, the average diameter error (error = P10 – caliper) was 0.3 cm with a standard deviation of 0.8 cm (n = 95). With all available data included (n = 105), the average error was -0.2 cm with a standard deviation of 2.1 cm. Error summaries by stem height showed an increasing average error above 10 m (Table 3.6). Stem diameter profiles based on lidar P10 were obtained up to 8 m on all nine trees surveyed. The average caliper stem diameter at the highest lidar-estimated stem height was 10.5 cm, with a mean lidar P10 error of 1.1 cm at the maximum measurable height (n = 9).

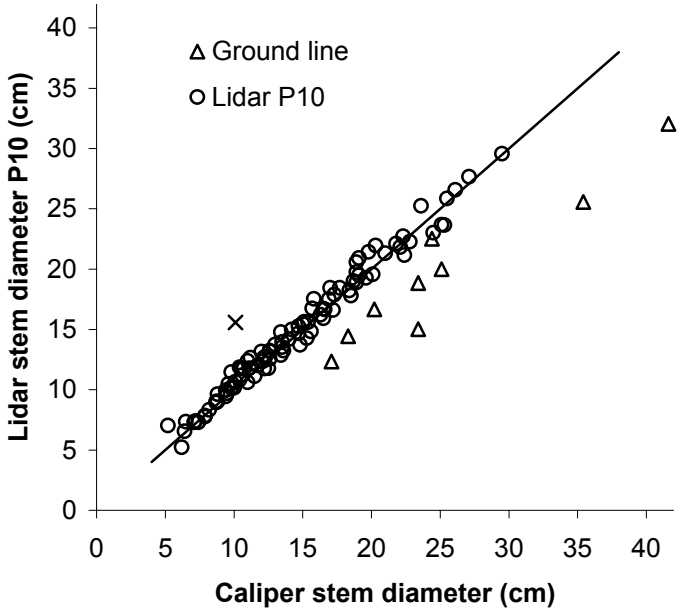

Figure 3.7. Lidar tenth-percentile (P10) stem diameter estimates paired with caliper stem diameter measurements taken at 1 m height intervals on nine loblolly pine trees. The datum marked with (x) corresponds to tree 5, height = 12 m.

Table 3.6. Stem diameter errors (lidar P10 – caliper) by stem height for nine loblolly pine trees.

Height (m)	Count (trees)	Average (cm)	Std Dev (cm)
0	9	-5.7	2.8
1	9	-0.1	1.0
2	9	0.1	0.9
3	9	0.1	0.5
4	9	0.5	0.3
5	9	0.5	0.9
6	9	0.1	0.7
7	9	0.2	0.7
8	9	0.5	1.0
9	8	0.2	0.8
10	6	0.3	0.7
11	4	0.5	0.2
12	3	1.1[†]	0.6
13	2	1.3	0.3

[†] tree 5 observation omitted, cf. Figure 3.7.

Patterns of localized peaks in the stem diameter profiles were commonly observed for trees 1-5 and in a few cases for trees 6-9 (e.g., Figure 3.6). Comparisons of field measurements of live branch heights with the scanner-derived stem profile "peaks" were not conclusive. For all but two trees, the heights to first live branches were > 10 m (Table 3.1). In contrast, scanner-derived stem profile measurements above 10 m were scarce. In all, less than 1% of the lidar-derived upper-stem diameter measurements corresponded to heights above the lowest measured live branches.

For tree 7 some determination of the nature of the stem profile peaks was possible based on comparisons involving the raw point-cloud data, registered point-clouds from multiple range images, and field notes, which included several measurements of heights to branches below the live crown (Table 3.7). We examined the point cloud data to identify branch heights on tree 7 using the proprietary point cloud management software LPMSCAN, (RIEGL Laser Measurement Systems; Figure 3.8). This examination showed a correspondence between the field records of tree 7 branch heights and measured branch heights from LPMSCAN. A computer-mouse controlled measurement tool was used to estimate branch heights from the ground using LPMSCAN. The branch heights as measured from LPMSCAN were within 0.1 m of field measured heights (Table 3.7). Although only select whorls are indicated by arrows in Figure 3.8, all the branches listed in Table 3.7 were identified in at least one of the scan A-C point clouds using LPMSCAN.

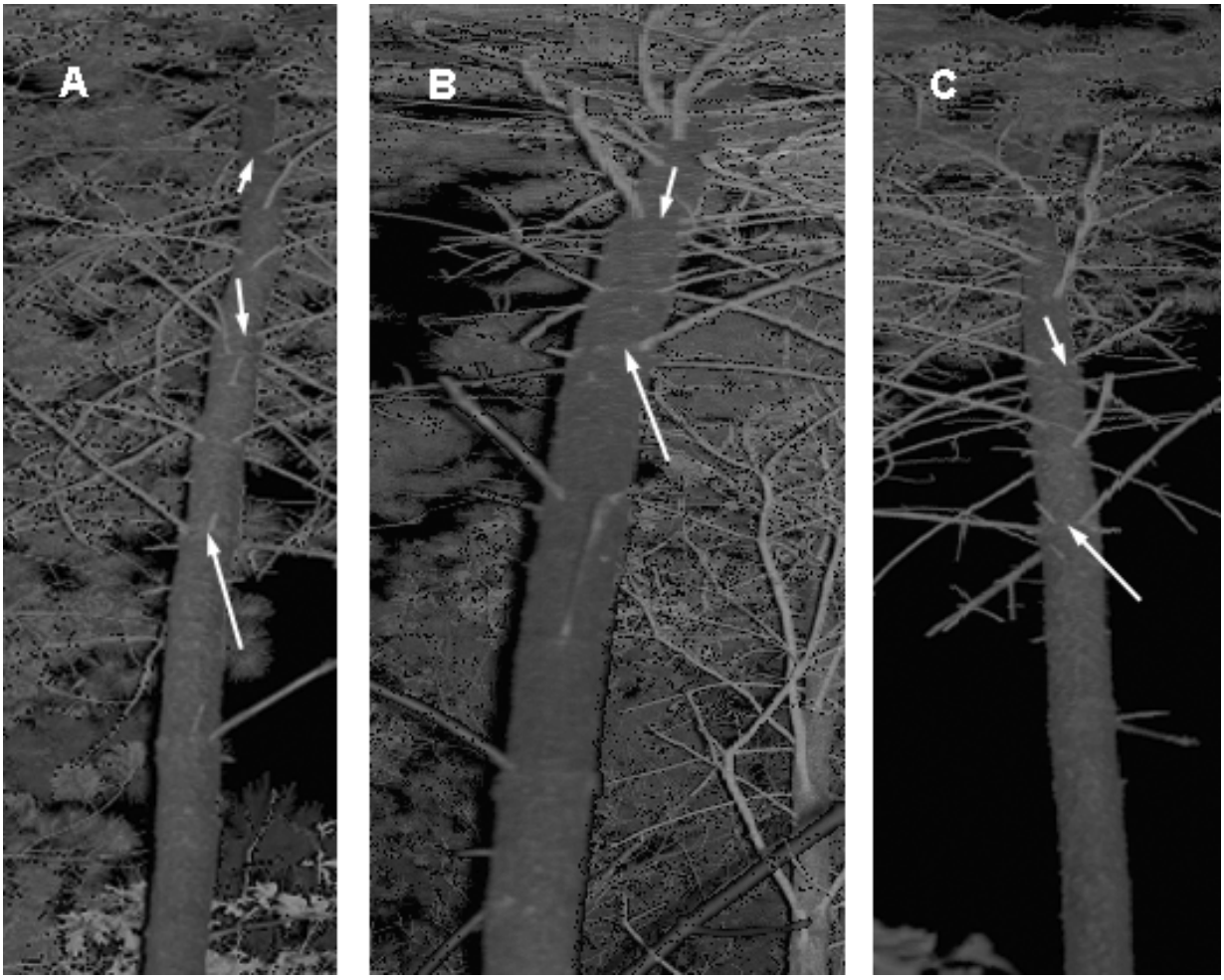

Figure 3.8. 2D rendering of point cloud data from subject tree 7, scans A-C. Lowest, upward pointing arrows point to a whorl at height 6.8 m. Higher, downward-pointing arrows point to a whorl at height 8.7 m. The top arrow in A points to a whorl at 11.3 m.

Table 3.7. Field measurements of tree 7 branch heights.

Branch height (m)
6.8
7.6
8.7
9.7†
10.3
10.7
11.3

† denotes lowest live branch

X-Y data from 10 cm thick bole slice sections with midpoint heights 6.8 m, 8.7 m and 11.3 m, were plotted from the combined, registered tree surface data of scans A-C (Figure 3.9).

X-Y scatterplots and rotating 3D scatterplots we examined (not presented here) all showed visible evidence of branches – some notable spatial distortions notwithstanding – at the same heights as were recorded in the field. The lidar-derived stem diameter profile for tree 7 (not shown) showed a distinct peak between 6.8 and 6.9 m; however, a low density of diameter point estimates above 7 m precluded the identification of other peaks at heights corresponding to those listed in Table 3.7. For trees scanned using the smaller scanner angle stepwidth of 0.054°, or when dead branch stubs persisted lower on trees where bole surface point densities were sufficiently high, LPMSCAN whorl measurements corresponded visibly with peaks on stem diameter profiles. As an example, whorls were noted on the LPMSCAN tree 6 point-clouds (not shown) at stem heights of {3.2, 3.7, 4.3, 4.6, 5.4 5.7, 6.1, 6.7, 7.0} m, all of which visibly matched peaks in the tree 6 diameter profile (Figure 3.10). It was not always possible for us to unequivocally identify branch locations based on the peaks in the lidar-derived diameter profiles alone. Nor was it always possible to find unambiguous evidence of branches from inspection of the point-cloud images, rotating plots, or 2D scatterplots of extracted bole slice sections alone; however, the various sources of information often corroborated branch heights when examined together.

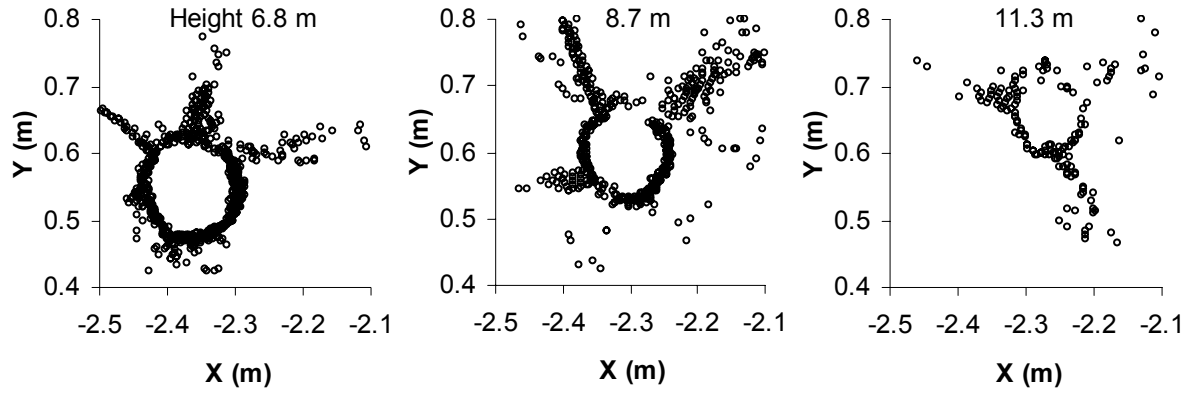

Figure 3.9. Bole slice sections at three whorls for tree 7 from co-registered scans A-C.

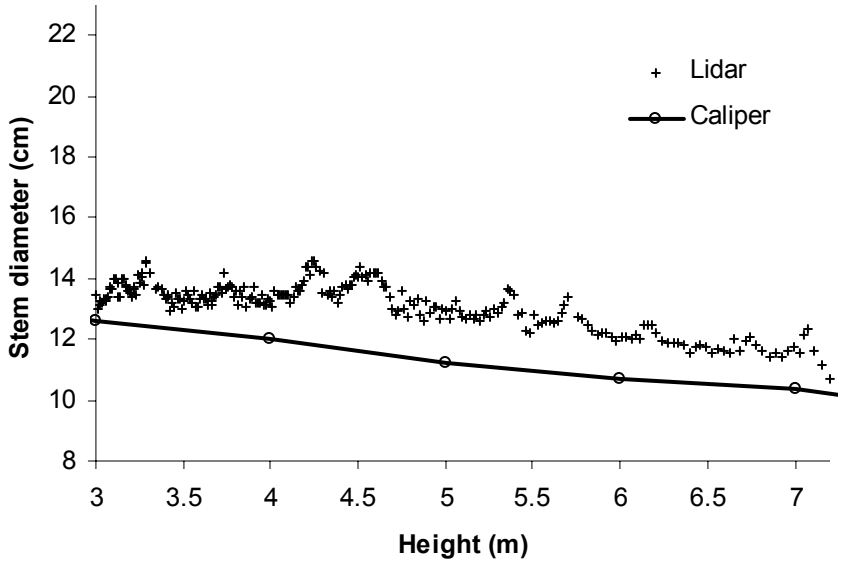

Figure 3.10. Detail of lidar-derived stem diameter profile for a 4 m section of tree 6.

3.4 DISCUSSION

Remote sensing from airborne platforms is, by far, the most widely used application of scanning lidar in assessing forest resources. Typical applications include measuring individual trees, estimating canopy structure or biophysical parameters, constructing terrain models, and estimating volume or mass contents at various scales (Nelson et al. 1988; Magnussen et al. 1998; Lefsky et al. 1999; Lefsky et al. 1999; Dubayah et al. 2000; Harding et al. 2001; Behera et al. 2002; Drake et al. 2002; Popescu et al. 2002; Brandtberg et al. 2003; Drake et al. 2003; Holmgren et al. 2003; Leckie et al. 2003; Lim et al. 2003; Lim et al. 2003; Popescu et al. 2003; Reutebuch et al. 2003; Weller et al. 2003; Zimble et al. 2003; Clark et al. 2004; Holmgren et al. 2004; Koukoulas et al. 2004; Næsset et al. 2004; Nelson et al. 2004; Patenaude et al. 2004; Popescu et al. 2004). In contrast, only a few applications of ground-based lidar scanning have been reported to date. Ground-based lidar has been shown to hold promise in the determination of various canopy structural attributes (Tanaka et al. 1998; Radtke et al. 2001; Lovell et al. 2003; Parker et al. 2004; Tanaka et al. 2004) and measurements of individual trees (Tanaka et al. 1998; Hopkinson et al. 2004; Thies et al. 2004).

Tanaka et al. (1998) constructed a laser range-finding system that used a rotating laser light source set apart from a CCD video camera and recorded the trace of the laser as it

illuminated nearby tree surfaces. Using triangulation geometry, rather than pulse return times, they generated 3D range images from which stem positions and diameters were measured. The work of Hopkinson et al. (2004) isolated individual trees for subsequent height and dbh measurement in multiple, merged lidar scenes acquired with a commercially available scanner on 0.12 ha field plots within two distinct forest types. Theis et al. (2004) merged lidar scenes, also acquired with a commercially available scanner, to make detailed stem measurements of two large diameter (≥ 60 cm), deciduous trees. Of these three studies, the work of Theis et al. (2004) is most similar to that carried out here, as it was aimed at making detailed measurements of a small number of individual target trees.

With regard to scene registration, both Hopkinson et al. (2004) and Theis et al. (2004) placed artificial targets in the lidar scenes as control markers. Both studies employed third party software or private contractors to perform the registration procedures. It is unclear to us following this study whether additional registration accuracy would have been gained here by the use of artificial targets or third-party software for image co-registration. Registration accuracy is typically difficult to quantify at points far away from precisely surveyed, paired reference targets. The co-registration statistics in Table 3.4 show that using tree centers can result in registration errors consistently averaging 1 cm or less. The accuracy of tree center estimates directly affected registration accuracy; further, accuracy seemed to degrade when fewer than 10 or 20 center points for a tree were identified in a single scan (Table 3.2, Table 3.4).

We did not present detailed results of upper stem measurements based on single scans; however, if some loss of precision were deemed acceptable, a measurement protocol could be devised requiring only one scan per tree (Figure 3.5, Figure 3.6). The single scan would nominally be made from a vantage point with a clear view to the stem. Assuming the costs of co-registration software will decrease in coming years, and improvements will be made to allow co-registration by computer users with little special training, certain gains achieved by using multi-view imagery may outweigh the costs.

Based on scans from three separate vantage points around each tree, our upper stem diameter estimates were accurate to within a few mm, on average, (Table 3.6) up to a height of 10 m. Such accuracy is seldom achieved by indirect dendrometry (Clark et al. 2000; Clark et al. 2000). We recognize that the P10 estimator for stem diameters may not be uniformly best;

however, we noted little sensitivity in the lidar-derived diameter estimates for small perturbations in the choice of quantile used, so long as it remained in a range roughly between the 5th and 20th percentiles. In contrast, the P10 estimator was useful in compensating for diameter overestimation from lidar returns due to stem defects or branches (Figure 3.6). A comparatively minor point involves the accurate measurement of stem diameters near the ground. Because we binned diameter point estimates from heights between zero and one-half meter to compute P10 and compared them with stem caliper measurements made at ground line, an obvious bias resulted (Figure 3.6, Figure 3.7). A method for estimating smooth diameter profiles, such as modeling by a taper equation, would undoubtedly give a more appealing characterization of the stem's flare near the ground line (Sharma et al. 2001; Sharma et al. 2003).

Loss of accuracy at points higher than 10 m in this study can be attributed, in part, to the reduced numbers of surface points in bole-slice sections at such heights. Several factors contribute to this reduction. First, point-density is reduced due to the scanner's finite angle stepwidth and the increased distance from the instrument to bole surfaces high above ground. Second, smaller stem diameters present smaller surfaces to be scanned, resulting in fewer surface points for arc-center estimation. Third, obstructions from branches and foliage reduce the number of data points available to characterize bole surfaces at such heights. The minimum angle stepwidth possible using the LPM-25HA was 0.027°, which, had we used it, may have effectively quadrupled the number of surface points characterizing unobstructed bole sections (Table 3.1, Table 3.2). Given additional time spent acquiring data at higher resolutions or the availability of a faster scanning mechanism, it seems possible that accurate characterization of some trees' upper stem diameters could be accomplished at heights substantially greater than 10 m. A newer model LPM scanner manufactured by Riegl USA Inc. allows angular stepwidths as small as 0.018°. Several commercially available rotating mirror scanner systems, which feature substantially faster data acquisition times than pan-tilt mount scanners, are capable of attaining stepwidths of 0.01° or smaller (Hopkinson et al. 2004; Thies et al. 2004).

While the work here does not provide a rigorous comparison of branch measurements with lidar-derived estimates, it does support the possibility that ground-based lidar could be used to accurately determine branch heights for branches at or below the base of the live crown. Considerable work remains to efficiently extract accurate branch information from data

summaries like those shown (Figure 3.8, Figure 3.9, Figure 3.10). Surface-point sample numbers on branch protrusions from the bole are relatively small due to the small sizes of branches and their distance from the scanning instrument. Nonetheless, it may be possible to extract useful information about branches from the point clouds including branch diameter, azimuth, inclination and possibly length. We did not develop an algorithm to use branch protrusions for assisting scene registration, but doing so would require matching paired branches' heights and azimuths for use as control points. Such a procedure might improve co-registration accuracy, especially high in the canopy.

Literature Cited

Behera, M.D. and Roy, P.S., 2002. Lidar remote sensing for forestry applications: The Indian context. Curr. Sci. 83: 1320-1328.

Besl, P.J. and McKay, N.D., 1992. A method for registration of 3-D shapes. IEEE Patt. Anal. Mach. Intell. 14: 239-256.

Brandtberg, T., Warner, T.A., Landenberger, R.E. and McGraw, J.B., 2003. Detection and analysis of individual leaf-off tree crowns in small footprint, high sampling density lidar data from the Eastern Deciduous Forest in North America. Rem. Sens. Env. 85: 290-303.

Clark, M.L., Clark, D.B. and Roberts, D.A., 2004. Small-footprint lidar estimation of sub-canopy elevation and tree height in a tropical rain forest landscape. Rem. Sens. Env. 91: 68-89.

Clark, N., Wynne, R.H., Schmoldt, D.L. and Winn, M., 2000. An assessment of the utility of a non-metric digital camera for measuring standing trees. Comp. El. Agr. 28: 151-169.

Clark, N.A., Wynne, R.H. and Schmoldt, D.L., 2000. A review of past research on dendrometers. For. Sci. 46: 570-576.

Dean, T.J., 2004. Basal area increment and growth efficiency as functions of canopy dynamics and stem mechanics. For. Sci. 50: 106-116.

DeKruger, D., Hodge, J., Bezdek, J.C., Keller, J.M. and Gader, P., 2001. Detecting mobile land targets in LADAR imagery with fuzzy algorithms. J. Intel. Fuz. 10: 197-213.

Drake, J.B., Dubayah, R.O., Knox, R.G., Clark, D.B. and Blair, J.B., 2002. Sensitivity of large-footprint lidar to canopy structure and biomass in a neotropical rainforest. Rem. Sens. Env. 81: 378-392.

Drake, J.B., Knox, R.G., Dubayah, R.O., Clark, D.B., Condit, R., Blair, J.B. and Hofton, M., 2003. Above-ground biomass estimation in closed canopy neotropical forests using lidar remote sensing: Factors affecting the generality of relationships. Glob. Ecol. Biogeogr. 12: 147-159.

Dubayah, R.O. and Drake, J.B., 2000. Lidar Remote Sensing for Forestry. J. For. 98: 44-46.

Eggert, D.W., Fitzgibbon, A.W. and Fisher, R.B., 1998. Simultaneous registration of multiple range views for use in reverse engineering of CAD models. Comp. Vis. Im. 69: 253-272.

Fitzgibbon, A.W., Eggert, D.W. and Fisher, R.B., 1997. High level CAD model acquisition from range images. Comput. Aid. 29: 321-330.

Hardie, R.C., Vaidyanathan, M. and McManamon, F., 1998. Spectral band selection and classifier design for a multispectral imaging laser radar. Opt. Eng. 37: 752-762.

Harding, D.J., Lefsky, M.A., Parker, G.G. and Blair, J.B., 2001. Laser altimeter canopy height profiles - methods and validation for closed-canopy, broadleaf forests. Rem. Sens. Env. 76: 283-297.

Hetzel, G., Leibe, B., Levi, P. and Schiele, B., Year. 3D object recognition from range images using local feature histograms. P. 394-399 *in* Proc. IEEE Comp. Soc. Conference on Computer Vision and Pattern Recognition, A. Jacobs, and Baldwin, T. (eds.), IEEE Computer Society, Los Alamitos, CA.

Holmgren, J. and Persson, A., 2004. Identifying species of individual trees using airborne laser scanner. Rem. Sens. Env. 90: 415-423.

Holmgren, J., Nilsson, M. and Olsson, H., 2003. Estimation of tree height and stem volume on plots-using airborne laser scanning. For. Sci. 49: 419-428.

Hopkinson, C., Chasmer, L., Young-Pow, C. and Treitz, P., 2004. Assessing forest metrics with a ground-based scanning lidar. Can. J. For. Res. 34: 573-583.

Huber, D.F. and Hebert, M., 2003. Fully automatic registration of multiple 3D data sets. Imag. Vis. Comp. 21: 637-650.

Jokinen, O. and Haggrén, H., 1998. Statistical analysis of two 3-D registration and modeling strategies. ISPRS J. Photogramm. Remote Sens. 53: 320-341.

Koukoulas, S. and Blackburn, G.A., 2004. Quantifying the spatial properties of forest canopy gaps using LiDAR imagery and GIS. Rem. Sens. Env. 25: 3049-3071.

Leckie, D., Gougeon, F., Hill, D., Quinn, R., Armstrong, L. and Shreenan, R., 2003. Combined high-density lidar and multispectral imagery for individual tree crown analysis. Can. J. Rem. Sens. 29: 633-649.

Lefsky, M.A., Harding, D., Cohen, W.B., Parker, G. and Shugart, H.H., 1999. Surface lidar remote sensing of basal area and biomass in deciduous forests of eastern Maryland, USA. Rem. Sens. Env. 67: 83-98.

Lefsky, M.A., Cohen, W.B., Acker, S.A., Parker, G.G., Spies, T.A. and Harding, D., 1999. Lidar remote sensing of the canopy structure and biophysical properties of Douglas-fir western hemlock forests. Rem. Sens. Env. 70: 339-361.

Lim, K., Treitz, P., Baldwin, K., Morrison, I. and Green, J., 2003. Lidar remote sensing of biophysical properties of tolerant northern hardwood forests. Can. J. Rem. Sens. 29: 658-678.

Lim, K., Treitz, P., Wulder, M., St-Onge, B. and Flood, M., 2003. Lidar remote sensing of forest structure. Prog. Phys. Geogr. 27: 88-106.

Lovell, J.L., Jupp, D.L.B., Culvenor, D.S. and Coops, N.C., 2003. Using airborne and ground-based ranging lidar to measure canopy structure in Australian forests. Can. J. Rem. Sens. 29: 607-622.

Magnussen, S. and Boudewyn, P., 1998. Derivations of stand heights from airborne laser scanner data with canopy-based quantile estimators. Can. J. For. Res. 28: 1016-1031.

Næsset, E., Gobakken, T., Holmgren, J., Hyyppä, H., Hyyppä, J., Maltamo, M., Nilsson, M., Olsson, H., Persson, Å. and Söderman, U., 2004. Laser scanning of forest resources: The Nordic experience. Scand. Jour. For. Res. 19: 482-499.

Nelson, R., Swift, R. and Krabill, W., 1988. Using airborne lasers to estimate forest canopy and stand characteristics. J. For. 86: 31-38.

Nelson, R., Short, A. and Valenti, M., 2004. Measuring biomass and carbon in Delaware using an airborne profiling LIDAR. Scand. J. For. Res. 19: 500-511.

Parker, G.G., Harding, D.J. and Berger, M.L., 2004. A portable LIDAR system for rapid determination of forest canopy structure. J. Appl. Ecol. 41: 755-767.

Patenaude, G., Hill, R.A., Milne, R., Gaveau, D.L.A., Briggs, B.B.J. and Dawson, T.P., 2004. Quantifying forest above ground carbon content using LiDAR remote sensing. Rem. Sens. Env. 93: 368-380.

Popescu, S.C., Wynne, R.H. and Nelson, R.F., 2002. Estimating plot-level tree heights with lidar: Local filtering with a canopy-height based variable window size. Comp. El. Agr. 37: 71-95.

Popescu, S.C., Wynne, R.H. and Nelson, R.F., 2003. Measuring individual tree crown diameter with lidar and assessing its influence on estimating forest volume and biomass. Can. J. Rem. Sens. 29: 564-577.

Popescu, S.C., Wynne, R.H. and Scrivani, J.A., 2004. Fusion of small-footprint lidar and multispectral data to estimate plot-level volume and biomass in deciduous and pine forests in Virginia, USA. For. Sci. 50: 551-565.

Radtke, P.J. and Bolstad, P.V., 2001. Laser point-quadrat sampling for estimating foliage-height profiles in broad-leaved forests. Can. J. For. Res. 31: 410-418.

Reutebuch, S.E., McGaughey, R.J., Andersen, H.E. and Carson, W.W., 2003. Accuracy of a high-resolution lidar terrain model under a conifer forest canopy. Can. J. Rem. Sens. 29: 527-535.

Sharma, M. and Oderwald, R.G., 2001. Dimensionally compatible volume and taper equations. Can. J. For. Res. 31: 797-803.

Sharma, M. and Burkhart, H.E., 2003. Selecting a level of conditioning for the segmented polynomial taper equation. For. Sci. 49: 324-330.

Stevens, M.R. and Beveridge, J.R., 2000. Localized scene interpretation from 3D models, range, and optical data. Comp. Vis. Im. 80: 111-129.

Tanaka, T., Yamaguchi, J. and Takeda, Y., 1998. Measurement of forest canopy structure with a laser plane range-finding method - development of a measurement system and applications to real forests. Agric. For. Met. 91: 149-160.

Tanaka, T., Park, H. and Hattori, S., 2004. Measurement of forest canopy structure by a laser plane range-finding method: Improvement of radiative resolution and examples of its application. Agric. For. Met. 125: 129-142.

Thies, M., Pfeifer, N., Winterhalder, D. and Gorte, B.G.H., 2004. Three-dimensional reconstruction of stems for assessment of taper, sweep and lean based on laser scanning of standing trees. Scand. J. For. Res. 19: 571-581.

Weller, D., Denham, R., Witte, C., Mackie, C. and Smith, D., 2003. Assessment and monitoring of foliage projected cover and canopy height across native vegetation in Queensland, Australia, using laser profiler data. Can. J. Rem. Sens. 29: 578-591.

Zhilkin, P. and Alexander, M.E., 2000. 3D image registration using a fast noniterative algorithm. Magn. Res. Imag. 18: 1143-1150.

Zimble, D.A., Evans, D.L., Carlson, G.C., Parker, R.C., Grado, S.C. and Gerard, P.D., 2003. Characterizing vertical forest structure using small-footprint airborne lidar. Rem. Sens. Env. 87: 171-182.

4 Results

4.1 Field plot data

On the 80 m × 80 m field plot 768 live trees were measured with dbh ranging from 0.4 cm to 85.1 cm in 1998. During the 2002 remeasurement 708 live trees were measured with dbh ranging from 0.6 cm to 86.2 cm. On the 40 m × 20 m interior plot 118 trees were measured in 1998 with dbh ranging from 0.7 cm to 51.9 cm. During the 2002 remeasurement 101 trees were measured with dbh ranging from 1.1 cm to 53 cm. Diameter distributions for the interior and entire plot are presented in Figure 4.1.

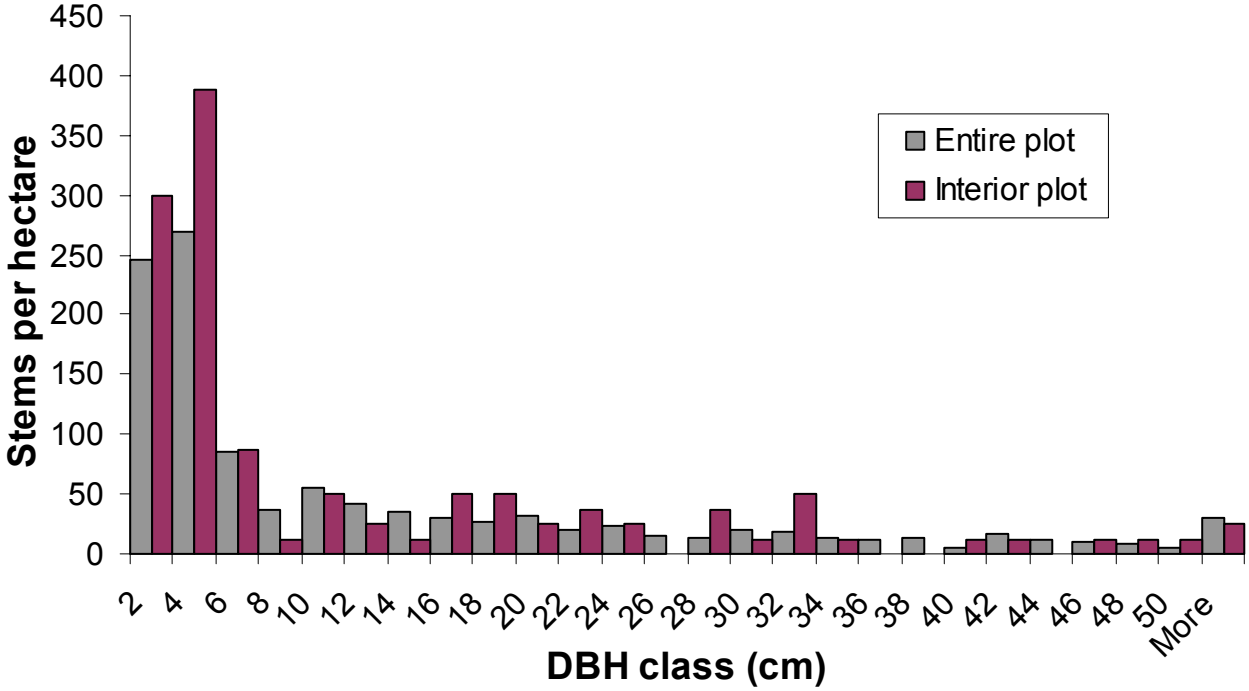

Figure 4.1. Interior (40 m × 20 m) and entire (80 m × 80 m) plot dbh distributions from the 2002 remeasurement.

Table 4.1 and Table 4.2 include species specific summaries for the entire and interior plots respectively. The interior plot is 0.08 ha in area while the entire plot is 0.64 ha in area. The interior plot represents 12.5% of the area of the entire plot. On the entire plot twenty-seven different species were measured while only twelve different species were measured on the interior plot. The interior plot contained 14.3% as many trees as present on the entire plot.

Table 4.1. Species specific summary information for all the trees measured on the 80 m × 80 m plot during the 2002 remeasurement.

Species	Number of Stems	Diameter Range (cm)	Quadratic mean diameter (cm)	Basal area (m^2/ha)
Acer pensylvanicum L.	156	(0.6,13.1)	2.9	0.158
Acer rubrum L.	111	(1,80.7)	18.8	4.827
Acer sacchrum Marsh.	2	(35.1,36.3)	35.7	0.313
Amelanchier alnifolia (Nutt.) Nutt.	1	(4.2,4.2)	4.2	0.002
Amelanchier arborea (Michx. f.) Fern.	2	(8.1,8.8)	8.5	0.018
Betula lenta L.	32	(3.7,42.7)	22.9	2.060
Carya glabra (Mill.)	26	(1.6,60.1)	30.9	3.038
Castanea dentatata (Marsh.) Borkh.	14	(0.9,6.3)	2.9	0.014
Cornus florida L.	67	(1,28.3)	8.3	0.567
Hamamelis virginiana L.	52	(1.2,5.2)	2.9	0.053
Ilex ambigua (Michx.) Torr.	1	(2.8,2.8)	2.8	0.001
Liriodendron tulipifera L.	57	(0.9,69.4)	31.6	6.992
Magnolia fraseri Walt.	38	(1,43.6)	8.0	0.301
Nyssa sylvatica Marsh.	21	(1.7,37.7)	17.3	0.769
Oxydendrum arboreum (L.) DC.	37	(1.5,32.9)	14.2	0.914
Pinus strobus L.	2	(3.7,4.8)	4.3	0.005
Pyrulania pubera Michx.	4	(1.8,3.5)	2.5	0.003
Quercus coccinea Muenchh.	6	(23.4,68.5)	56.9	2.386
Quercus prinus L.	29	(1.4,79.6)	33.8	4.070
Quercus rubra L.	4	(23.6,86.2)	49.4	1.196
Quercus velutina Lam.	6	(16.3,83.7)	48.9	1.759
Robinia pseudoacacia L.	5	(28.1,56.5)	43.0	1.134
Sassafras albidum (Nutt.) Nees	4	(1.4,4)	2.5	0.003
Symplocos tinctoria L. (L'Her.)	6	(1.8,4.4)	2.8	0.006
Tilia americana L.	3	(4.7,52.8)	31.1	0.357
Tsuga canadensis (L.) Carr.	15	(1,24.1)	11.0	0.222
unknown*	6	(1.2,44.7)	25.0	0.459
All species	707	(0.6,86.2)	19.1	31.630

* Trees in the unknown category could not be identified by species in the field.

Table 4.2. Species specific summary information for all the trees measured on the interior 20 m × 40 m plot during the 2002 remeasurement.

Species	Number of Stems	Diameter Range (cm)	Quadratic mean diameter (cm)	Basal area (m^2/ha)
Acer pensylvanicum L.	30	(1.1,5)	2.3	0.162
Acer rubrum L.	7	(2.3,30.3)	18.7	2.396
Betula lenta L.	4	(15.9,31.4)	25.3	2.505
Carya glabra (Mill.)	3	(16.3,53)	37.4	4.114
Cornus florida L.	8	(1.9,14.8)	7.8	0.481
Hamamelis virginiana L.	15	(1.3,5.2)	3.2	0.152
Liriodendron tulipifera L.	17	(1.1,48.9)	27.8	12.868
Magnolia fraseri Walt.	4	(2,3.8)	2.9	0.032
Oxydendrum arboreum (L.) DC.	4	(1.7,14.7)	8.1	0.255
Robinia pseudoacacia L.	2	(31.6,45.9)	39.4	3.049
Tilia americana L.	3	(4.7,52.8)	31.1	2.857
Tsuga canadensis (L.) Carr.	4	(3.4,17.9)	12.4	0.604
All species	101	(1.1,53)	17.2	29.475

4.2 Scanner data

All of the scans were viewed in range image form using 3D-RiSCAN, the software packaged with the scanner. All scans were exported from that software in delimited ASCII text file format for further processing, viewing and manipulation using other computer programs.

4.2.1 Range image view of data

Range images represent 3D data in a visual 2D format. The range images in Figure 4.2 are examples of the type of raw data obtained in this research. Each pixel in a range image corresponds to a single range measurement. Pixels that are adjacent from left to right correspond to a single azimuth but are obtained at incremental polar angles corresponding to the user defined angular scan resolution. Likewise pixels that are adjacent from top to bottom correspond to a common polar angle but incremental azimuths at the same scan resolution. The images were cropped so that both images in Figure 4.2 represent an 80° × 180° field of view centered on the zenith. The angular resolution of both scans is 0.18°. The tree stems visible in the images appear to curve toward the center of the image due to distortion introduced by projecting the 3D data as a 2D image.

Differences between leaf-on and leaf-off conditions are apparent in images A and B in Figure 4.2. More points are visible far from the scanner in the leaf-off image as evidenced by the greater visibility of branches in the upper canopy and the fact that the holes in the canopy appear larger and more frequent. The black pixels in Figure 4.2 represent pulses that were not intercepted. In Figure 4.2A canopy gaps appear notably smaller. Under leaf-off conditions (Figure 4.2A) 13,927 pulses were not intercepted, while under leaf-on conditions (Figure 4.2A) only 994 pulses were not intercepted.

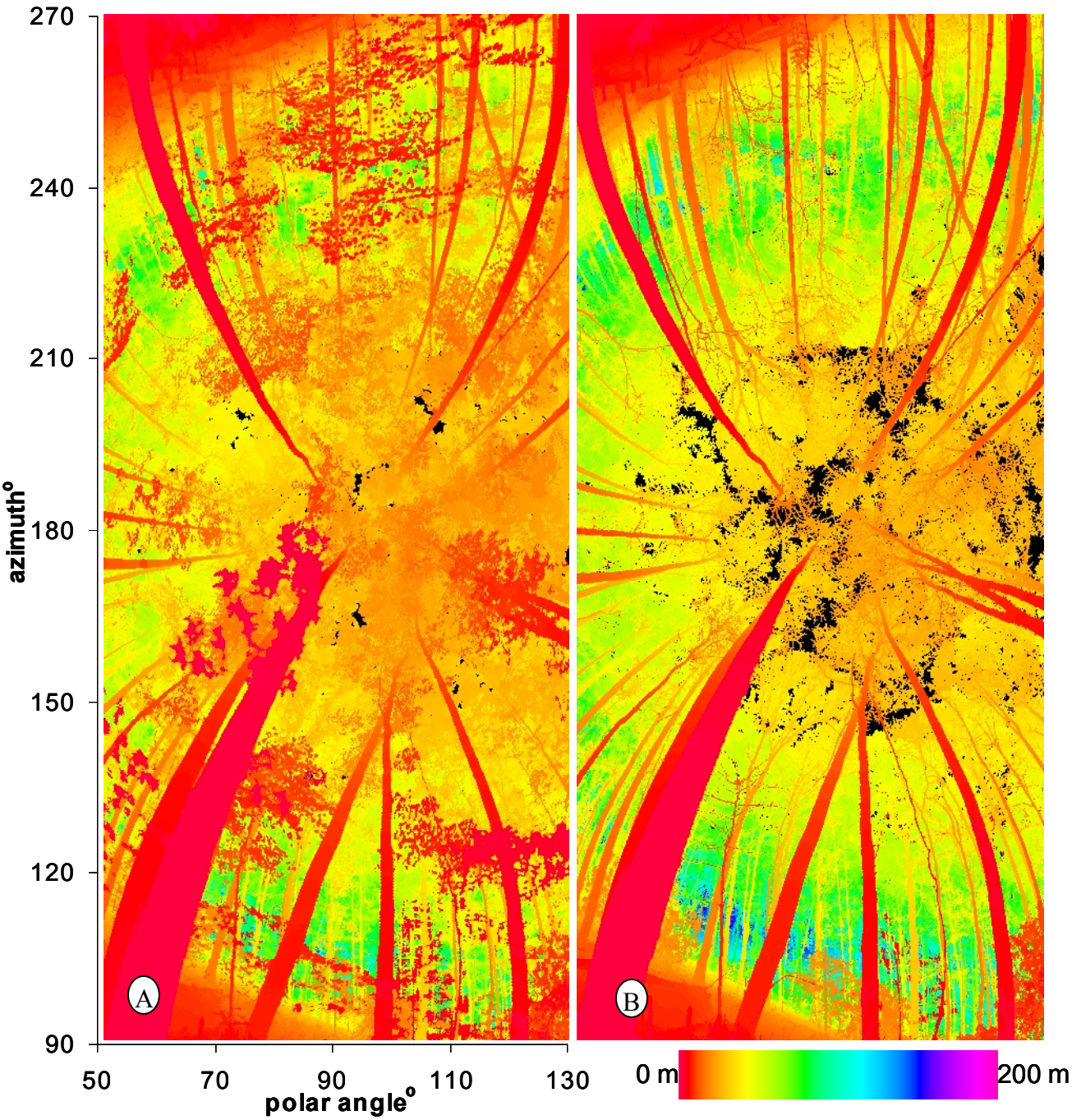

Figure 4.2. False color range images generated from single scans from node (60, 40) during leaf-on (A) and leaf-off (B). Polar angle and azimuth scales are included for reference. Colors represent distance from the scanner as indicated by the color bar scale.

Occluding foliage close to the scanner is visible in Figure 4.2A. This type of occlusion was typical for the leaf-on scans, many of which exhibited even greater amounts of foliage near the scanner with correspondingly greater occlusion of distant surfaces. The average range

measurement in the pixels under leaf-off (Figure 4.2B) was 32.6 m while the average range measurement in the leaf-on image (Figure 4.2A) was 25.2 m.

4.2.2 Point cloud view of data

Point cloud data are comprised of the XYZ Cartesian coordinates of each intercepted laser pulse return as present in delimited ASCII text files exported from 3D-RiSCAN. Point clouds were viewed as 2D marginal scatter plots or 3D rotating scatter plots at various scales and vantages. Specific regions within point clouds could be viewed separately from the bulk of data, or omitted from viewing. Point clouds were partitioned into manageable-size data sets to facilitate rendering and overcome hardware or software limitations.

In order to graphically present the scanner data in point cloud format it was often necessary to limit the volume of the scan presented. This was generally due to the inability of the computer hardware and the graphing software available to render data sets comprised of hundreds of thousands and in some cases millions of points in a multidimensional format.

Figure 4.3 and Figure 4.4 are 3D scatter plots of the point cloud obtained from single scans from node (50, 40) during leaf-on and leaf-off. In both images the displayed data are limited to the 80 m × 80 m × 80 m cubic volumes with the scanner at the scatterplots' origins. A number of tree boles are visible in both figures. The images are rotated to illustrate the sloping terrain. A greater total number of points are present in the leaf-off image because a wider field of view was used for the scans obtained from (50, 40) during leaf-off than for scans obtained during leaf-on.

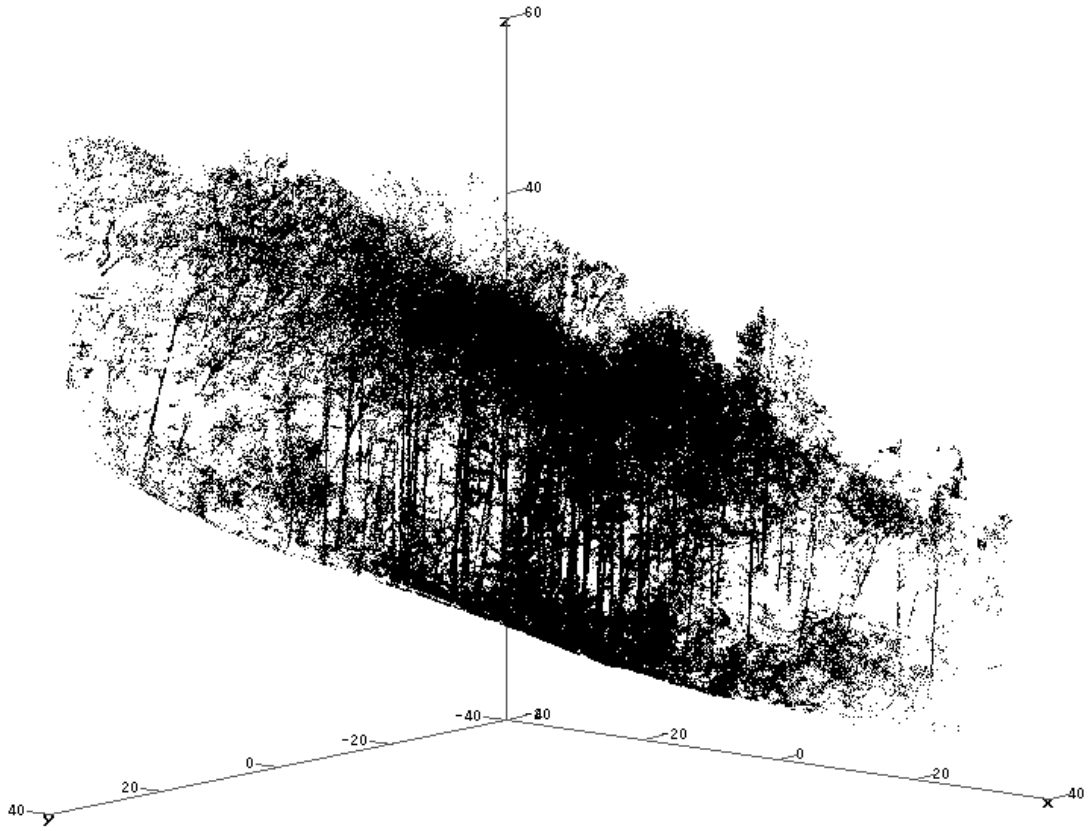

Figure 4.3. 3D scatter plot of point cloud data obtained from a single scan at node (50, 40) during leaf-off. Plot depicts 749,465 points, with each point representing a single range measurement.

The leaf-off data in Figure 4.3 appear to have a greater number of points higher in the canopy than the leaf-on data in Figure 4.4. To verify this fact the median Z-value of the points in the two figures were calculated with all points below a Z-value of 3 m ignored to eliminate ground interceptions. The median Z-value for the remaining points under leaf-off conditions was 22 m while the median Z-value of the remaining points under leaf-on condition was 12.5 m.

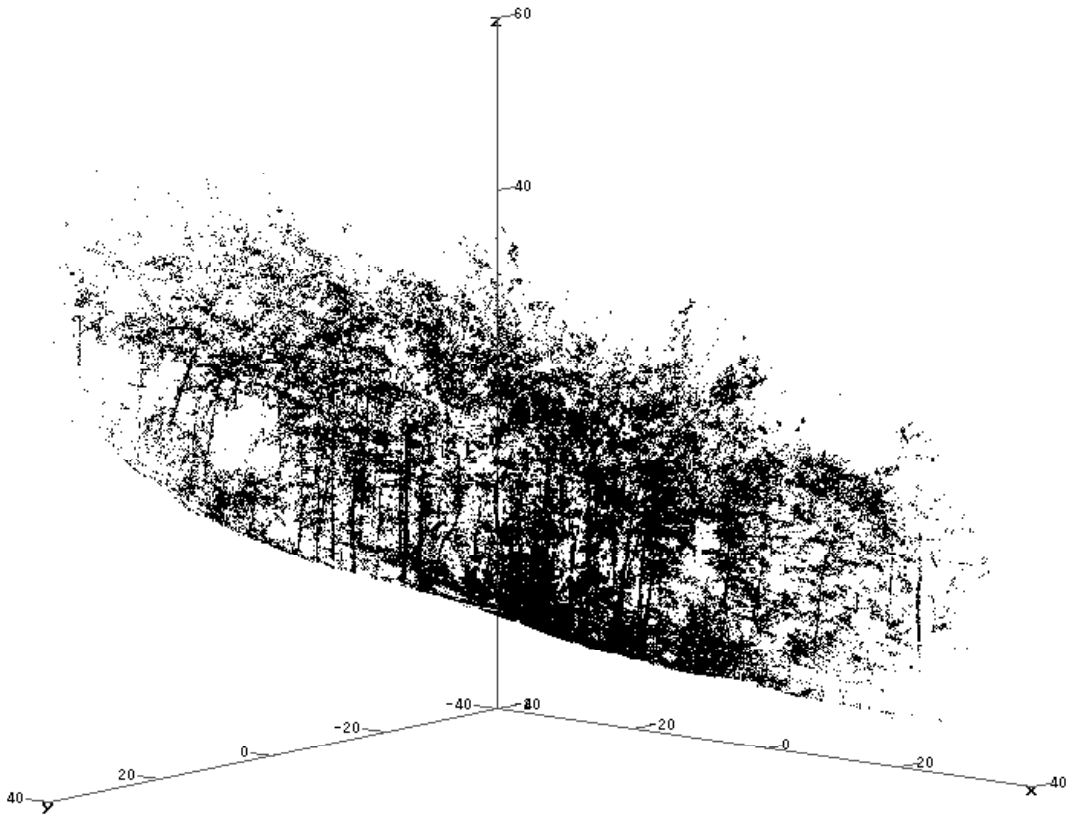

Figure 4.4. 3D scatter plot of point cloud data obtained from a single scan at node (50, 40) during leaf-on. Plot depicts 640,315 points, with each point representing a single laser pulse return.

Marginal XY-scatter plots were created to provide overhead views of the point clouds (Figure 4.5). The scanner was located at point (0, 0) and the data were cropped vertically to range between 0 m and 20 m in the marginalized Z-direction to highlight occluded sectors.

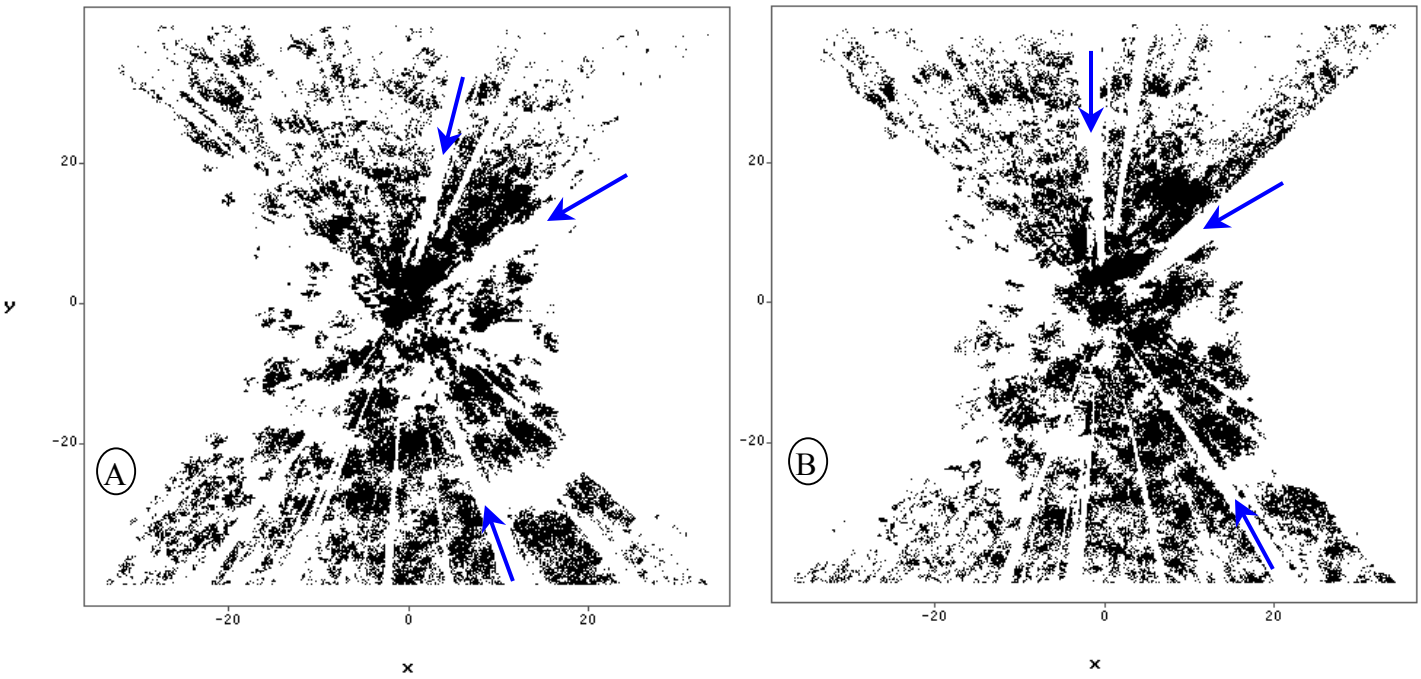

Figure 4.5. Horizontal point cloud profiles obtained from a single scan at node (50, 40) during periods of leaf-on (A) and leaf-off (B), respectively. Arrows indicate occluded sectors.

These "overhead views" illustrate the extent of the scanner coverage in the horizontal directions and show how point densities decrease with distance from the scanner. Large voids on the left and right sides of the scatterplots were due to the instrument's limited, 80° extent, in polar angle. Combining multiple scans to obtain complete hemispherical coverage over each tripod position eliminated the voids.

Given that the sector occlusions occurred over the entire 20 m vertical extent of the data shown in the overhead views, it was determined that the occluded sectors were caused by the boles of trees. Corresponding occluded sectors were evident in both leaf-on and leaf-off scans (Figure 12). Moving clockwise from the top of the images in Figure 4.5 the occluded sectors indicated by the arrows were caused by a 53 cm dbh *Cary glabra*, 5.7 m from the scanner; a 20.9 cm *Liriodendron tulipifera*, 0.9 m from the scanner; and a 21.5 cm *L. tulipifera*, 3.5 m from the scanner. The width of occluded sectors was related to both the size of the occluding tree and its distance from the scanner.

The fact that corresponding occluded sectors were offset by a slight rotation between the two scans shown was due to the inaccurate means by which the scanner was positioned in the field (Figure 4.5). The registration algorithm accounted for this inaccuracy.

4.3 Registration evaluation

Registration was carried out in a stepwise process. The following sections present results pertaining to the individual steps and facilitate evaluation of the complete registration process. The results that follow were obtained using the point cloud data. Comparisons were made between the use of leaf-off and leaf-on data and the use of single scan and node-level point clouds to determine how various factors affected the registration steps. Appropriate examples are presented in the following sections and generally are associated with the steps involved in the registration of scan 2 from node (30, 30) obtained under leaf-off conditions. The effects of using registered data on occlusion reduction, point cloud reclassification, canopy surface distribution modeling and stem map creation are included in sections related to those applications.

4.3.1 Coarse registration

The results of coarse registration—aligning point clouds to the field plot coordinate system based on field notes—are shown in Figure 4.6. Coarse registration was accomplished for all scans by first applying Equation [10] to the XYZ point cloud data (Figure 4.6A and B).

$$\mathbf{A} = \begin{bmatrix} 0 & 0 & 1 \\ 0 & 1 & 0 \\ -1 & 0 & 0 \end{bmatrix} \quad \text{and} \quad \widetilde{\mathbf{b}} = \begin{bmatrix} 0 \\ 0 \\ 0 \end{bmatrix} \qquad [10]$$

The second coarse registration step involved rotating the data, in horizontal plane, through an offset angle defined in the field, and shifting the data horizontally based on the node coordinates. For scan 2 from node (30, 30) the recorded offset angle of 210° between the long-axis of the scanner and the field plot's X-axis required the transformation shown in Equation [11] (Figure 4.6C).

$$\mathbf{A} = \begin{bmatrix} \cos(210) & \sin(210) & 0 \\ -\sin(210) & \cos(210) & 0 \\ 0 & 0 & 1 \end{bmatrix} \quad \text{and} \quad \widetilde{\mathbf{b}} = \begin{bmatrix} 30 \\ 30 \\ 0 \end{bmatrix} \qquad [11]$$

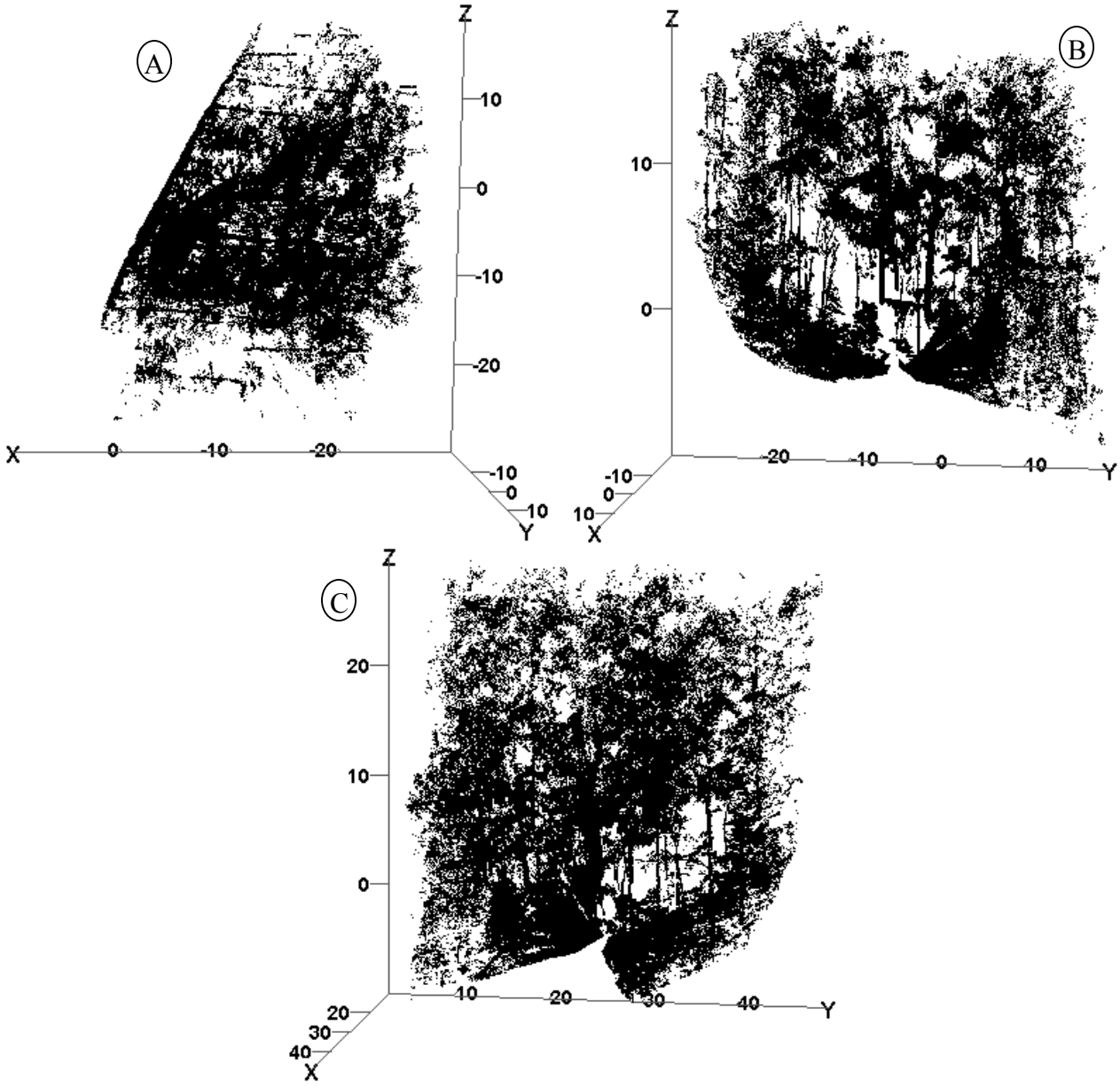

Figure 4.6. Point cloud from scan 2 (A) obtained from node (30, 30) during leaf-off. The coarse registration first made the XY-plane correspond to the field plot's horizontal XY-plane (B) using Equation [10]. The point cloud was then rotated and translated based on field notes to correspond to the field plot coordinate system (C) using Equation [11].

Offset angles measured in the field were generally accurate to within 5 to 10°. In the context of positional accuracy an error of 5° in the scanner's orientation resulted in a tree 20 m from the scanner being 1.7 m from its measured field plot XY coordinates. The following fine registration steps minimized positional errors.

4.3.2 Isolation and matching of bole sections for within node registration

Summaries of the extracted bole sections (EBSs) from each scan matched for use in ICP registration are presented in Table 4.3 and Table 4.4 for leaf-on and leaf-off conditions, respectively. In Table 4.3 and Table 4.4 the number of bole sections used for registration are not listed for any of the scan 1s. This was because multiple scans were registered to each scan 1. The number of bole sections used from a scan 1 was the same as the scan 2 or 3 that was registered to it.

The algorithm found more points on more bole sections under leaf-off conditions. Under leaf-on conditions there were a number of instances where only one bole section was found that was usable for registration. An average of 2.9 EBSs were used for within node registration of the leaf-on data and an average of 3.6 EBSs were used for within node registrations of the leaf-off data. Recall that EBS surfaces were used directly in the leaf-on registrations while EBS centers were used in the leaf-off registrations.

Table 4.3. Summary of extracted bole sections (EBSs) from leaf-on scans. Surface points of EBSs matched between scans were used in ICP registrations of scans from a common node.

Node	Scan	Potential EBSs	Actual EBSs	Mean and range of points per EBS	Mean and range of distance in XY plane of EBSs from scanner (m)	Number of bole sections used for registration
(30,30)	2	22	10	1,338 (512, 5,525)	11.3 (6.5,16.6)	3
(30,30)	1	15	9	3,296 (716, 10,941)	10.4 (3.6,19.3)	-
(30,30)	3	22	10	1,203 (526, 2,045)	11.8 (4.6,18.6)	3
(30,40)	2	22	11	2,489 (553, 6,165)	10.5 (3.5,18.5)	2
(30,40)	1	18	10	1,700 (534, 3,942)	10.6 (2.2,17.4)	-
(30,40)	3	21	9	1,504 (527, 2,732)	11.8 (5.4,18.9)	3
(30,50)	2	18	12	3,741 (748, 19,271)	10.2 (3,18.9)	4
(30,50)	1	19	13	1,619 (555, 4,000)	11.2 (3.6,18.1)	-
(30,50)	3	23	12	1,334 (606, 2,635)	10.4 (4,18)	6
(40,30)	2	20	9	1,553 (456, 4,485)	10.3 (5.5,16.6)	2
(40,30)	1	21	11	1,569 (933, 3,145)	10.8 (5.8,16.6)	-
(40,30)	3	16	6	2,158 (780, 5,892)	10.1 (5.5,16.4)	2
(40,40)	2	16	10	2,245 (536, 4,584)	9.7 (3.4,15.9)	3
(40,40)	1	16	6	1,496 (801, 3,113)	10.9 (7.1,16.6)	-
(40,40)	3	25	12	3,557 (935, 22,522)	10.2 (2.2,16.4)	3
(40,50)	2	20	13	1,657 (588, 3,978)	10.1 (4.1,15.7)	4
(40,50)	1	20	12	1,663 (748, 3,766)	9.4 (2.5,15.3)	-
(40,50)	3	14	9	3,747 (1,076, 14,872)	8.4 (4,15.7)	2
(50,30)	2	19	7	2,890 (1950, 4,944)	7.5 (4,12.7)	3
(50,30)	1	19	5	1,977 (556, 5,166)	9.2 (5.1,18.1)	-
(50,30)	3	16	6	1,471 (467, 2,391)	9.3 (5,18.1)	2
(50,40)	2	16	11	1,455 (664, 3,667)	11.8 (6.1,20.9)	3
(50,40)	1	17	16	1,152 (526, 1,961)	12.4 (6.3,21.5)	-
(50,40)	3	15	11	2,387 (508, 6,066)	9.8 (3.9,15.6)	1
(50,50)	2	22	19	2,118 (689, 8,475)	10.6 (4.6,18.1)	1
(50,50)	1	21	16	2,080 (601, 4,352)	10.8 (4.6,20.1)	-
(50,50)	3	21	21	1,573 (700, 2,891)	10.7 (4.6,18.1)	6
(60,30)	2	12	4	1,970 (490, 3,876)	10.1 (6,13.7)	1
(60,30)	1	12	6	1,182 (589, 1,944)	10.7 (8.2,12.4)	-
(60,30)	3	19	10	2,314 (517, 10,708)	9.7 (3.7,14.5)	3
(60,40)	2	33	21	2,228 (726, 7,352)	10.1 (4.7,16.5)	5
(60,40)	1	28	18	1,750 (498, 6,704)	10.9 (4.8,23.4)	-
(60,40)	3	26	16	2,295 (882, 12,001)	10.8 (4.1,20.5)	3
(60,50)	2	15	12	2,073 (407, 8,321)	9.5 (2.5,18.2)	3
(60,50)	1	21	16	2,741 (359, 16,542)	9.3 (2.3,17.1)	-
(60,50)	3	20	16	2,489 (779, 9,412)	9.5 (3.4,14.4)	2
(70,30)	2	18	9	6,375 (661, 31,947)	9.1 (1.8,19)	2
(70,30)	1	25	12	2,523 (596, 8,659)	9.4 (2,15.4)	-
(70,30)	3	17	8	1,510 (427, 3,283)	10.2 (6.5,15.5)	3
(70,40)	2	17	10	2,080 (574, 4,818)	11.2 (5.4,14.7)	4
(70,40)	1	14	11	1,855 (634, 4,505)	10.3 (5.5,16.7)	-
(70,40)	3	11	9	1,266 (662, 1,978)	12.9 (8.5,16.9)	1
(70,50)	2	17	8	2,114 (624, 5,598)	9.7 (4.4,14.3)	2
(70,50)	1	15	12	3,171 (661, 9,248)	9.6 (0.5,16.2)	-
(70,50)	3	17	10	3,065 (574, 10,027)	9.6 (4.3,16.1)	5

Table 4.4. Summary of extracted bole sections (EBSs) from leaf-off scans. Center points of EBSs matched between scans were used in ICP registrations of scans from a common node.

Node	Scan	Potential EBSs	Actual EBSs	Mean and range of points per EBS	Mean and range of distance in XY plane of EBSs from scanner (m)	Number of bole sections used for registration
(30,30)	2	21	12	2,806 (567, 8,486)	11.4 (1.7,21.9)	5
(30,30)	1	16	12	4,097 (542, 22,931)	12.7 (1.3,21.9)	-
(30,40)	2	14	9	2,865 (715, 5,826)	11.1 (3.5,17.5)	4
(30,40)	1	16	13	2,944 (743, 12,481)	13.4 (1.7,21.9)	-
(30,40)	3	22	14	2,238 (678, 4,122)	14.8 (5.4,23.1)	3
(30,50)	2	12	7	2,908 (1,220, 5,612)	11.9 (3.8,18.2)	3
(30,50)	1	14	9	2,478 (1,264, 5,148)	12.5 (3.5,21.5)	-
(40,30)	2	12	9	2,804 (726, 6,644)	10.1 (4.1,18.9)	3
(40,30)	1	14	8	2,004 (462, 3,894)	11.1 (5.2,17.2)	-
(40,30)	3	18	16	2,479 (942, 7,113)	11.4 (4.3,16.8)	3
(40,40)	2	31	22	2,881 (720, 9,870)	11.4 (3.4,19.8)	4
(40,40)	1	29	18	2,812 (483, 24,242)	10.9 (2,19.6)	-
(40,40)	3	19	16	2,614 (468, 5,453)	11 (2.4,20.1)	5
(40,50)	2	16	12	4,098 (493, 23,296)	14.3 (4,22.3)	3
(40,50)	1	16	12	3,743 (464, 12,288)	13.5 (3.9,22.9)	-
(40,50)	3	16	10	2,486 (814, 6,030)	10.3 (2.6,20.6)	3
(50,30)	2	10	7	1,670 (1,198, 1,919)	12.1 (4.1,18.3)	3
(50,30)	1	10	10	12,469 (442, 103,473)	9.2 (0.9,18.2)	-
(50,30)	3	17	13	2,724 (1,054, 7,532)	9.4 (0.6,19.3)	4
(50,40)	2	25	21	1,914 (615, 5,492)	11.7 (4.3,21.4)	5
(50,40)	1	24	19	2,813 (482, 9,251)	9.5 (4.1,16.8)	-
(50,40)	3	27	24	2,029 (768, 7,295)	10.5 (3.3,21.1)	3
(50,50)	2	19	17	3,007 (820, 7,628)	12.8 (6.1,20.4)	3
(50,50)	1	19	17	2,825 (495, 16,134)	12.4 (5.6,19.5)	-
(50,50)	3	11	7	4,865 (788, 16,650)	11.2 (6,17.8)	3
(60,30)	2	15	13	3,374 (942, 7,641)	10.2 (4.9,19.1)	4
(60,30)	1	16	12	2,817 (588, 7,142)	12.6 (4.6,22.1)	-
(60,30)	3	16	10	10,181 (1,110, 75,170)	11.9 (0.6,22)	3
(60,40)	2	26	20	2,279 (476, 6,574)	10.8 (4.4,23.3)	3
(60,40)	1	28	16	2,627 (989, 11,837)	10.8 (3.9,20.3)	-
(60,40)	3	29	23	2,271 (674, 5,789)	10.1 (4.2,23.9)	5
(60,50)	2	16	11	4,510 (1,491, 11,261)	10.1 (3.5,15.7)	4
(60,50)	1	15	13	4,294 (1,194, 12,034)	12.4 (2.6,18.6)	-
(60,50)	3	16	12	2,295 (1,066, 4,895)	12.5 (3.3,18.1)	3
(70,30)	2	18	12	3,245 (664, 14,060)	12.6 (2.1,19.7)	4
(70,30)	1	11	6	1,975 (883, 3,842)	12.4 (7.1,16.6)	-
(70,40)	2	25	12	2,815 (789, 10,183)	12.5 (5.7,21.3)	2
(70,40)	1	14	11	4,103 (1,468, 12,030)	11.2 (4.1,21.1)	-
(70,40)	3	16	15	2,982 (682, 17,599)	10 (2.6,20.9)	4
(70,50)	2	18	13	11,222 (1,341, 103,902)	12 (1,21.4)	4
(70,50)	1	17	14	3,534 (811, 10,215)	12.7 (4.3,21.4)	-

Figure 4.7 shows a leaf-on point cloud obtained in scan 2 from node (30, 30) and potential bole sections that were extracted from this point cloud using the automated bole section extraction algorithm. Figure 4.7B contains all of the output from this algorithm, which includes some points that do not actually represent bole section surfaces and were not useful in registration. Twenty-three potential bole sections are pictured Figure 4.7B, with ten verified as representing actual bole sections. The point cloud in Figure 4.7A consisted of 515,024 points while 34,222 data points are presented in Figure 4.7B.

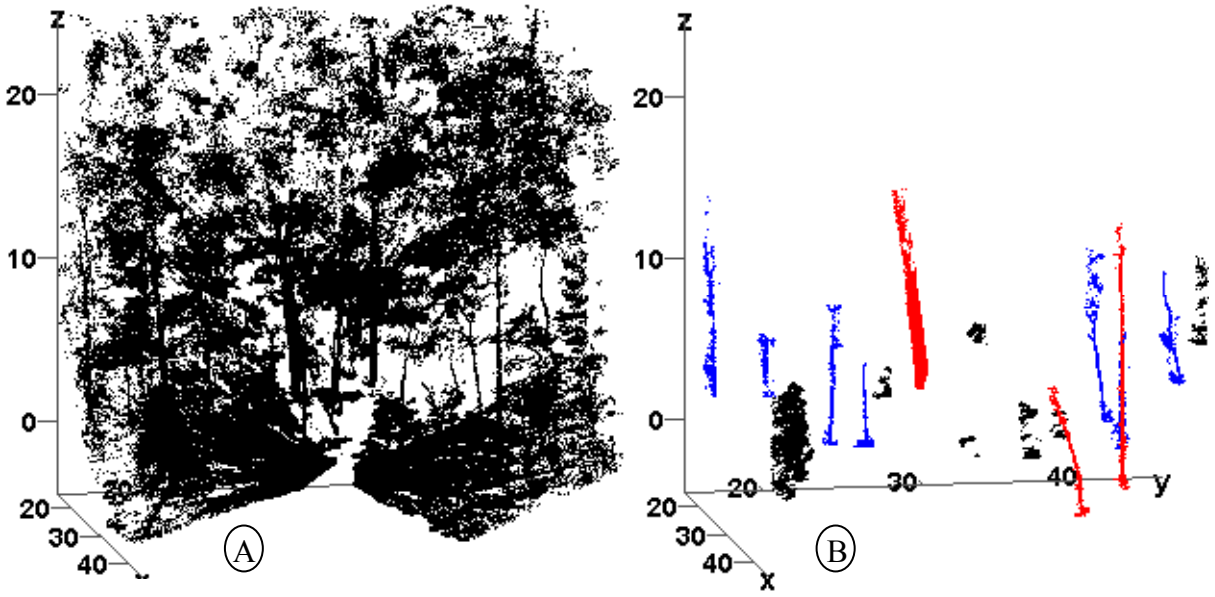

Figure 4.7. Coarsely registered, scan 2, leaf-on point cloud from node (30, 30) (A) and the potential bole sections extracted (B) from that scan using the automated bole section extraction algorithm. Actual bole sections are highlighted in blue and red, with red indicating bole sections matched to bole sections from scan 1 for registration.

The same bole section extraction procedure was applied to scan 1 from node (30, 30); the scan to which scan 2 was registered. The matching of bole sections was completed through comparison of extracted bole section XY locations and 3D point clouds. Three bole sections were matched between scans 1 and 2 from node (30, 30) (Figure 4.7B).

Table 4.5 provides a summary of the output of bole section extraction from all leaf-on and leaf-off scans respectively, for within node registration. Not all of the leaf-off scans were identical with the thirty-two scans along the plot edge being limited in azimuth range and having higher resolution than the nine scanner locations completely within plot. For this reason the same results for the leaf-off scans in this section are presented over all scans and divided by whether

the scanner was located within the plot or along the plot border as indicated in the table. These divisions were not necessary for the leaf-on data because three scans were captured at all nodes using consistent resolution and angular scan limits for all scans.

Table 4.5. Summary of the EBSs obtained from individual scans with the automated bole section extraction algorithm

	Leaf-off	Leaf-on
Total number of potential EBSs	744	850
Total number of actual EBSs	547	504
Percentage of potential EBSs representing actual EBSs	73.5%	59.3%
Mean number of points per actual EBS	3,377	2,169
Mean vertical range of actual EBSs	16.6 m	11.7 m
Mean points per vertical meter of actual EBSs	271	214
Mean Distance in XY-plane of actual EBSs from scanner	11.5 m	10.3 m
Mean number of actual EBSs per scan	13 (20[a],11[b])	11
Number of scans	41	45

[a] Value is for the 9 complete overhead scans from nodes (40, 40), (50, 40) and (60, 40).
[b] Value is for all scans along the plot edge (i.e. those not contained in [a]).

A larger number of actual EBSs were identified in leaf-on scans; in contrast, the percentage of useable EBSs was larger in the leaf-off scans. The mean number of points per vertical meter of EBS is larger for leaf-off scans, which, in part, reflects that data were collected at a higher scan resolution in leaf-off versus leaf-on. Due to differences in angular extents and resolution between summer and winter scans, direct comparisons can be made only for the nine complete overhead scans from nodes (40,40), (50,40) and (60,40), acquired using identical scanner resolution and angular limits (Table 4.5, footnote a). Increased numbers and vertical extents of EBSs provided larger control surfaces for registration and larger input data sets for the center finder algorithm.

4.3.3 Within node ICP registration

Once bole sections were paired from scans 1 and 2 or scans 1 and 3, they were saved in separate data files for each scan. Unregistered EBS data from scans 1 and 2 from node (30, 30) are presented in Figure 4.8. The imperfect alignment visible in Figure 4.8 reflects the imperfect nature of the coarse registrations.

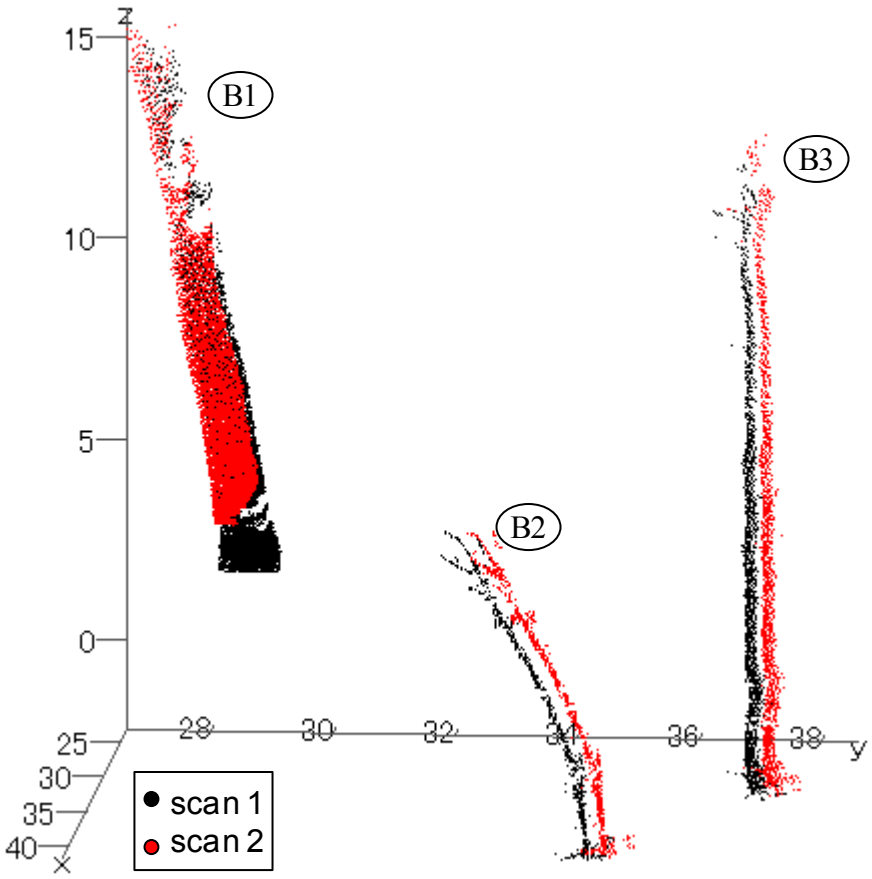

Figure 4.8. Paired bole section point clouds used to register scans 1 and 2 from node (30, 30).

In Figure 4.8 the scan 1 data set was comprised of 9,059 points (6,765, 716 and 1,578 points for bole sections B1, B2 and B3, respectively). The scan 2 data set was comprised of 7,660 points (5525, 772 and 1363 points for bole sections B1, B2 and B3, respectively). Bole sections B1, B2, and B3 in Figure 4.8 correspond to an 86.2 cm dbh *Quercus rubra*, a 12.2 cm dbh *Cornus florida* and a 26.7 cm dbh *Acer rubrum*, respectively. From the 2002 remeasurement field data, tree B1 was located at field plot coordinates (23.3 m, 29.5 m), 6.7 m from the scanner. Tree B2 was located at field plot coordinates (41.3 m, 35.9 m), 12.7 m from the scanner. Tree B3 was located at field plot coordinates (40.6 m, 37.9 m), 13.2 m from the scanner. The distances between the XY positions of trees B1, B2 and B3 from the coarsely registered scan 1 point cloud and the trees positions recorded in the tree survey were 0.9 m, 0.9 m and 0.3 m, respectively. The distances between the XY positions of trees B1, B2 and B3 from the coarsely registered scan 2 point cloud and their positions recorded in the tree survey were 1.1 m, 0.5 m and 0.5 m, respectively. The distances between the paired bole sections from the two coarsely registered

scans were 0.2 m for B1, 0.5 m for B2 and 0.3 m for B3. The XY positions of the bole sections in the scanner data were determined with the center finding algorithm at breast height (1.37 m) of each bole section.

The EBS representations of trees B2 and B3 were nearly identical in both leaf-on scan 1 and scan 2 point clouds from node (30, 30), satisfying the requirement of inclusive segmentation (Figure 4.8). The point clouds for these bole sections cover nearly the exact same vertical extent and the scans were captured from a common tripod location so the same side of the tree was visible. For bole section B1 the scan 2 EBS covers a vertical range within that of the matched bole section from scan 1. Thus, inclusive segmentation was satisfied for all three EBSs identified for registering scans 1 and 2, from node (30, 30) (Figure 4.8).

Equation [12] contains the transformation parameters obtained from the ICP algorithm to align scan 2 with scan 1, using the EBS surfaces displayed in Figure 4.8.

$$\mathbf{A}_{2\to 1} = \begin{bmatrix} 0.9997 & 0.0219 & 0.0046 \\ -0.0220 & 0.9998 & 0.0030 \\ -0.0045 & -0.0031 & 1.0000 \end{bmatrix} \quad \text{and} \quad \widetilde{\mathbf{b}}_{2\to 1} = \begin{bmatrix} -0.7644 \\ 0.6032 \\ 0.1895 \end{bmatrix} \qquad [12]$$

In all reported transformation parameters actual values have been rounded to four decimal places. The mean distance between closest points at convergence of ICP was 3.5 cm. Figure 4.9 shows the results of applying the transformation parameters $\mathbf{A}_{2\to 1}$ and $\widetilde{\mathbf{b}}_{2\to 1}$ to align the scan 2 EBSs with their scan 1 counterparts.

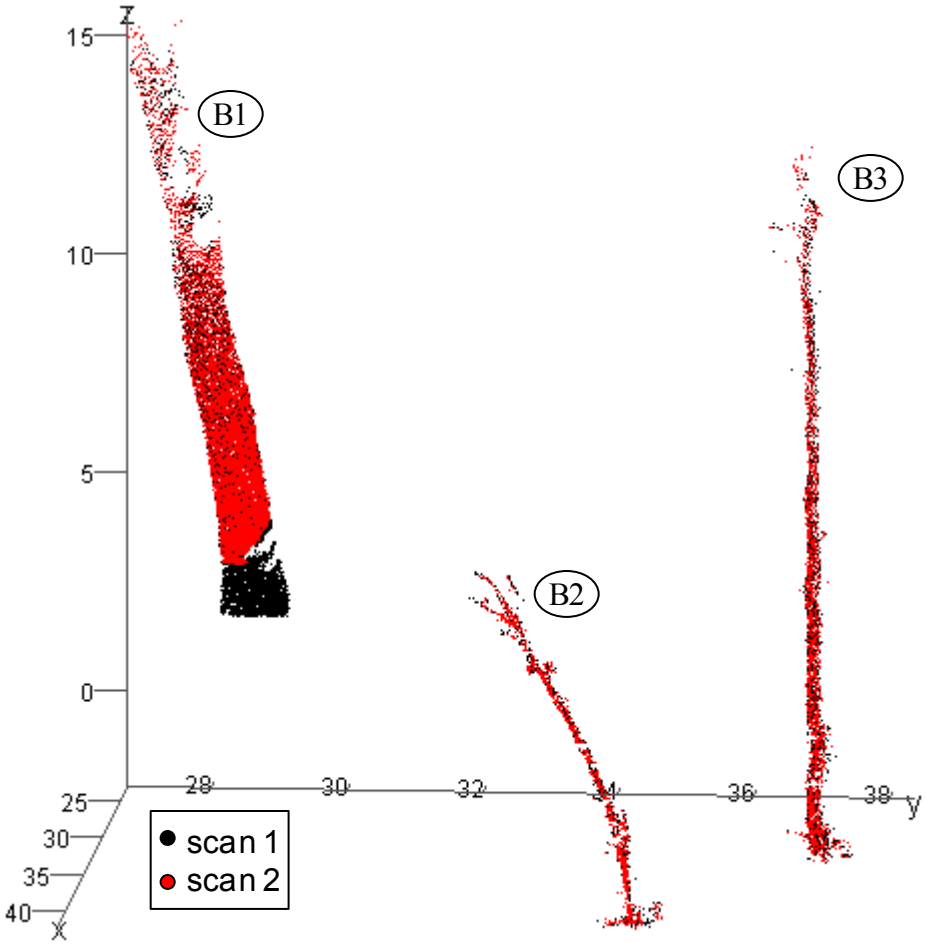

Figure 4.9. Matched bole sections from leaf-on scans 1 and 2 from node (30, 30) following application of transformation parameters $\mathbf{A}_{2\to1}$ and $\tilde{\mathbf{b}}_{2\to1}$ from Equation [12].

The Equation [12] transformation was applied to the entire point cloud from scan 2. A separate transformation was obtained in the same manner to align the node (30, 30) leaf-on scan 3 to scan 1. Within node transformations were obtained in the same manner for all the nodes of the field plot, one set for leaf-on scans and another set for leaf-off scans. Following within node registration the aligned point clouds for each node were combined into single node-level data files.

4.3.4 Extraction and matching of bole sections between node-level point clouds

The extraction of bole sections for the node-level point clouds proceeded in the same manner as for the single scan point clouds. More bole sections were typically extracted from the

node-level point clouds than the single scan point clouds (Figure 4.10). Table 4.6 and Table 4.7 include summaries of EBSs used in between node registration for leaf-off and leaf-on data, respectively. The reported matched bole section counts are only for the registrations of the given node, not when that node was used as a target for registration.

Table 4.6. Summary statistics for extracted bole sections (EBSs) from leaf-on node point clouds. Matched EBS centers were used in between node ICP registrations.

Node	Potential EBSs	Actual EBSs	Mean and range of points per EBS	Mean and range of distance in XY plane of EBSs from node (m)	Number of bole sections used for registration
(30,30)	64	26	3,681 (735, 26,954)	10.9 (3.6,21.9)	3
(30,40)	60	24	2,874 (689, 7,877)	12.4 (3.5,22.1)	6
(30,50)	51	32	3,492 (480, 27,375)	11.8 (2.9,21.5)	4
(40,30)	55	20	2,480 (1,031, 5,025)	9.8 (3.7,16.5)	5
(40,40)	58	25	4,100 (406, 31,341)	11.7 (2.3,20.8)	4
(40,50)	52	25	4,145 (621, 22,122)	11.1 (3.2,22.4)	4
(50,30)	57	18	5,458 (488, 48,461)	10.5 (2.1,19.2)	3
(50,40)	48	39	2,465 (526, 10,151)	11.5 (3.4,21)	-
(50,50)	54	30	3,731 (644, 12,807)	12.6 (4.7,20.1)	2
(60,30)	50	23	2,456 (682, 10,613)	10.6 (3.9,21)	4
(60,40)	55	37	4,320 (681, 20,026)	11.6 (2.4,23.4)	4
(60,50)	51	29	4,687 (481, 28,528)	11.1 (2.4,20.2)	4
(70,30)	49	19	9,122 (1,319, 70,997)	9.3 (1.6,19.1)	3
(70,40)	50	28	2,607 (445, 9,838)	12.1 (3.7,21.3)	3
(70,50)	43	19	4,417 (731, 18,408)	12.4 (4.4,24.7)	4

Table 4.7. Summary statistics for extracted bole sections (EBSs) from leaf-off node point clouds. Matched EBS centers were used in between node ICP registrations.

Node	Potential EBSs	Actual EBSs	Mean and range of points per EBS	Mean and range of distance in XY plane of EBSs from node (m)	Number of bole sections used for registration
(30,30)	34	18	4,735 (665, 28,904)	13.3 (1.3,21.8)	5
(30,40)	52	27	3,871 (720, 21,310)	14.8 (3.3,25.9)	6
(30,50)	27	19	2,864 (325, 7,767)	11 (0.5,21.4)	4
(40,30)	45	29	3,049 (351, 8,222)	11.5 (4,18.5)	4
(40,40)	58	40	5,016 (485, 39,984)	13 (2,26.2)	6
(40,50)	41	28	5,010 (608, 41,171)	13.7 (1.9,22.8)	5
(50,30)	30	22	12,130 (506, 19,2839)	10.6 (0.7,18.3)	5
(50,40)	63	46	4,169 (599, 18,224)	12.5 (3.6,25.3)	-
(50,50)	43	34	4,298 (474, 36,587)	13.4 (2.3,22.4)	5
(60,30)	38	32	4,714 (366, 17,542)	11.8 (2.3,22.1)	4
(60,40)	50	42	4,199 (732, 19,269)	11.6 (4.1,23.8)	5
(60,50)	39	28	5,509 (579, 25,674)	12.9 (2.5,24.4)	4
(70,30)	20	15	3,914 (663, 9,512)	12.6 (7.1,18)	5
(70,40)	42	30	3,685 (528, 21,368)	12.2 (2.6,21.3)	5
(70,50)	27	19	5,526 (430, 20,155)	13.8 (4.1,23.5)	6

A total of 59 potential bole section were extracted from the (40, 40) node-level point cloud, with 27 visually confirmed as actual bole sections (Figure 4.10A). A total of 63 potential bole sections were extracted from the (30, 30) node-level point cloud, with 29 confirmed as actual bole sections (Figure 4.10B). The region of overlap where common EBSs could be found for these nodes was 30 m × 30 m. In this overlapping area 15 actual bole sections were extracted from node (40, 40) (Figure 4.10A) and 18 actual bole sections were extracted from node (30, 30) (Figure 4.10B).

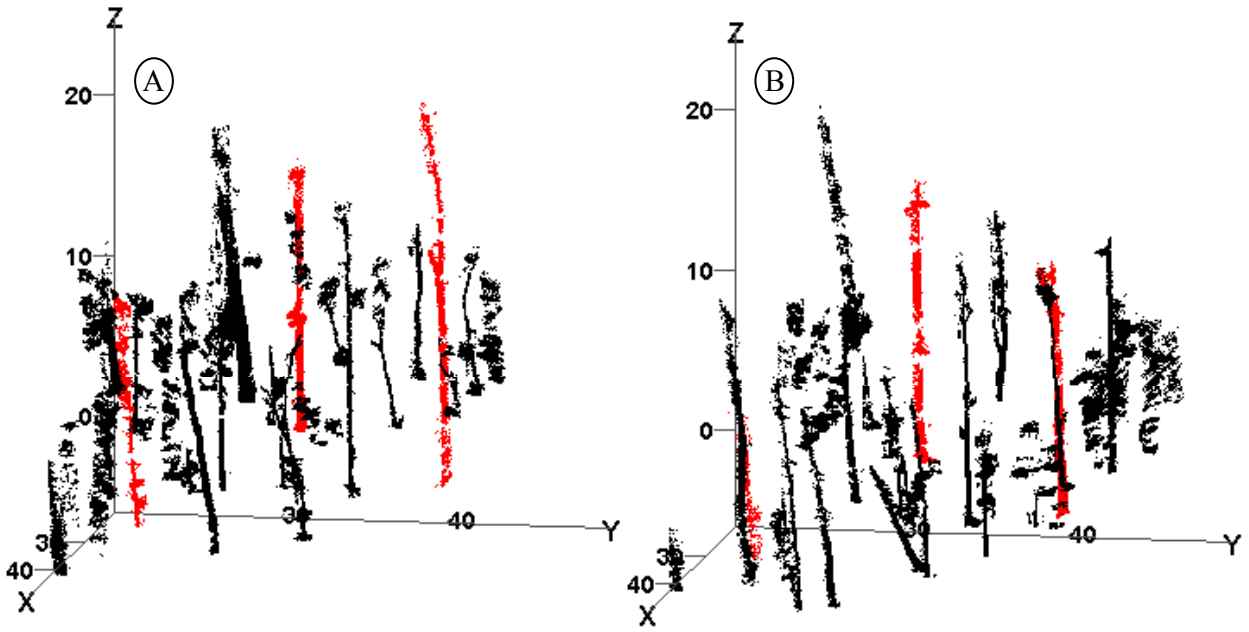

Figure 4.10. Extracted potential bole sections from the overlapping areas between the node-level point clouds from node (30, 30) (A) and node (40, 40) (B). Matched bole sections used in ICP registration are in red.

Matching bole sections between node-level point clouds was made difficult by the fact that the bole sections were scanned from different vantage points meaning they may be occluded at different points or they may simply appear dissimilar in profile. As a result the appearances and vertical extents of visible bole sections may be substantially dissimilar in the point-clouds being aligned. Further, matched bole sections were seldom, if ever comprised of an equal number of points when scanned from different nodes. Differences in the ground elevation of different plot nodes also results in dissimilarities in scanned bole sections between nodes. Some of these attributes are illustrated in Figure 4.11, which shows a 3D scatter plot of three matched bole sections extracted from the node (30, 30) and node (40, 40) leaf-off point clouds. For node (40, 40) the data shown consist of 14,141 points (748, 9977 and 3416 points for bole sections B1, B2, and B3, respectively). The node (30, 30) data consist of 32,728 points (3479, 2295 and 26954 points for bole sections B1, B2 and B3, respectively).

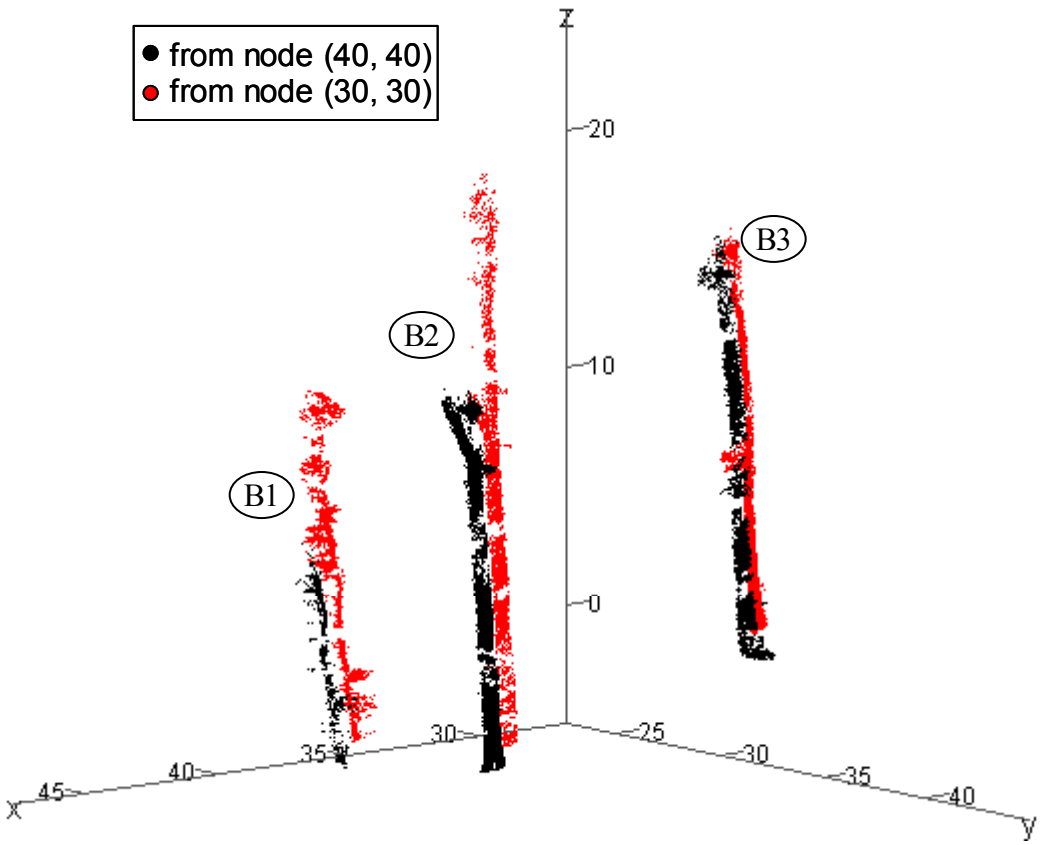

Figure 4.11. Matched bole sections from nodes (30, 30) and node (40, 40) point clouds before registration.

Bole sections B1, B2, and B3 in Figure 4.11 corresponded to a 19.5 cm dbh *Nyssa sylvatica*, a 53.0 cm dbh *Carya glabra* and a 60.1 cm dbh *Carya glabra*, respectively. In the 2002 tree survey data B1 corresponded to a tree located at coordinates (36.1 m, 24.7 m), 8.0 m from node (30, 30) and 15.8 m from node (40, 40). B2 was located at coordinates (46.8 m, 44.7 m), 22.3 m from node (30, 30) and 8.3 m from node (40, 40). B3 was located at coordinates (27.0 m, 33.0 m) 4.2 m from node (30, 30) and 14.8 m from node (40, 40). The horizontal distances between the XY positions of trees B1, B2 and B3 from the node (40, 40) point cloud and their positions recorded in the tree survey were 1.3 m, 0.2 m and 0.8 m, respectively. The horizontal distances between the XY positions of trees B1, B2 and B3 from the node (30, 30) point cloud and their positions recorded in the tree survey were 0.4 m, 0.2 m and 0.4 m, respectively. The horizontal distances between the XY positions of paired bole sections from the two unregistered node point clouds were 1.1 m for tree B1, 0.3 m for tree B2 and 0.5 m for tree B3. The XY

positions for the EBSs were determined using the center finding algorithm at breast (1.37 m) height of the bole sections.

Table 4.8 contains a comparison of summaries of EBSs obtained from the leaf-off and leaf-on node-level point clouds. The extraction algorithm found more potential bole sections and a higher percentage of actual bole sections under leaf-off conditions. Compared to the extraction of bole sections from single-scan point clouds there was a decrease in efficiency of the extraction algorithm for the node-level point clouds (Table 4.5 and Table 4.8). The density of points decreased further from the scanner resulting in the taller bole sections and bole sections further from the scanner visible in the leaf-off data being represented by relatively fewer points per vertical meter (Table 4.8). Some of the summary information was divided to highlight the differing scan limits used under leaf-off conditions, as indicated in the Table 4.8 footnotes.

Table 4.8. Summary of the EBSs obtained from node-level point clouds.

	Leaf-off	Leaf-on
Total number of potential EBSs	609	797
Total number of actual EBSs	429	394
Percentage of potential EBSs representing actual EBSs	70.44%	49.44%
Mean number of points per actual EBS	4,741	3,860
Mean vertical range of actual EBSs	18.0 m	13.2 m
Mean points per vertical meter of actual EBSs	308	351
Mean Distance in XY-plane of actual EBSs from node	12.6 m	11.4 m
Mean number of actual EBSs per node	29 (43[a],18[b],29[c])	26
Number of nodes	15	15

[a] Value is for the data from nodes (40, 40), (50, 40) and (60, 40) where each node was comprised of three complete overhead scans.
[b] Value is the mean for the data from the four corner nodes, (30, 30), (30, 50), (70, 30) and (70, 50), each comprised of only two scans that were limited in azimuth angular range.
[c] The value for the eight non-corner plot edge nodes where each node was comprised of three scans that were limited in azimuth angular range (i.e. those not included in [a] or [b]).

4.3.5 Finding stem centers

Stem center points were used as control surfaces to register nodes obtained from different vantage points. This added step required that, for each matched bole section, an adequate number of center points could be found to facilitate registration. A vector of center points was found for

all potential bole sections and only those sections with an adequate number of center points were matched between node-level point clouds.

The estimation of a single center point is pictured in Figure 4.12. The represented horizontal slice was from bole section B2 in Figure 4.11 from the (40, 40) node-level point cloud. The EBS corresponded to a 53 cm dbh *Cary glabra* located 8.3 m from node (40, 40).

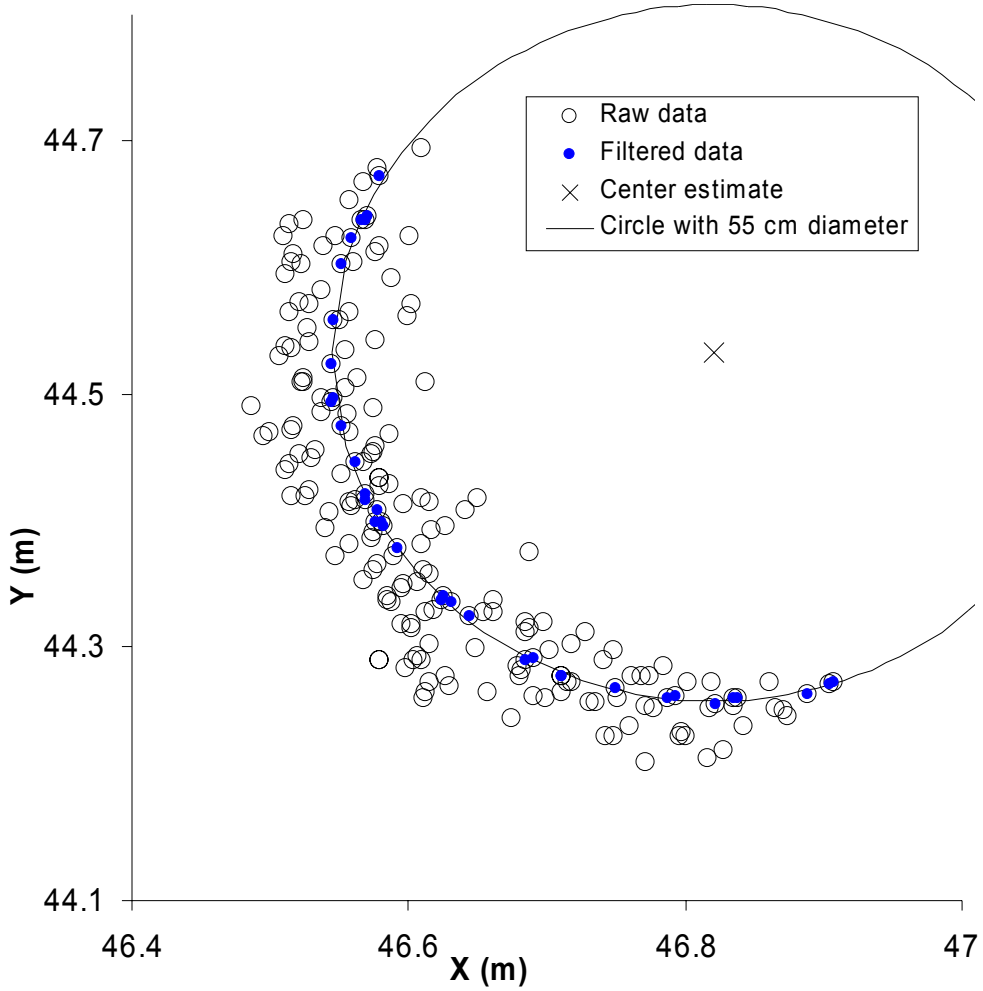

Figure 4.12. Raw data were a 10.7 cm vertical slice of a bole section point cloud consisting of 200 points near breast height (1.37 m). 36 points were selected from the raw data as those best fitting a horizontal arc. The estimated diameter was 55 cm and a circle of that diameter with the estimated center is plotted in the graph.

Figure 4.13 contains "center vectors" comprised of a vertical series of center points for each of the matched bole sections in Figure 4.11. Inclusive segmentation was not guaranteed for these vectors because the points are relatively sparse and do not explicitly represent stem centers at corresponding heights. This lack of inclusive segmentation necessitated interpolation.

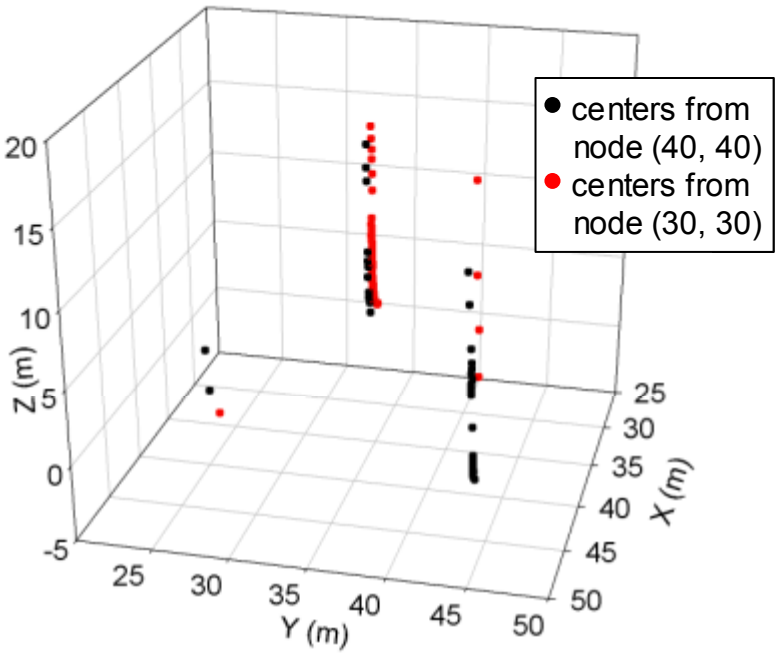

Figure 4.13. Center vectors estimated from the three paris of matched bole sections in Figure 4.11.

The interpolated stem center data sets used for registration are presented in Figure 4.14. By interpolating the stem centers from one node inclusive segmentation was guaranteed. However, it was not possible to tell whether it was best to interpolate the center data from (30, 30) or (40, 40). Registrations were calculated with the data from each node interpolated.

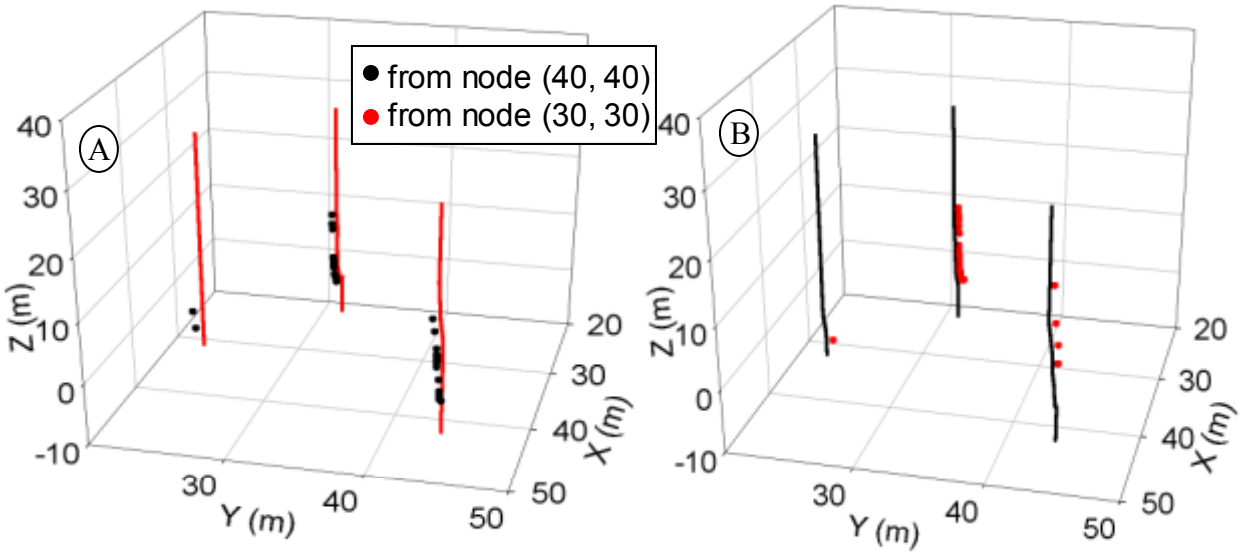

Figure 4.14. The interpolated bole section center data set used for registration. In (A) the centers from node (30, 30) have been interpolated while in (B) the centers from node (40, 40) have been interpolated.

4.3.6 Between node ICP registrations

The two between node registrations were estimated using the ICP algorithm applied to the data in Figure 4.14A and Figure 4.14B. Equation [13] is the transformation calculated with ICP using the data from Figure 4.14A. At convergence of ICP the mean distance between closest points was14 cm.

$$\mathbf{A}_{(30,30)\rightarrow(40,40)} = \begin{bmatrix} 0.9999 & -0.0074 & 0.0079 \\ 0.0075 & 0.9998 & -0.0157 \\ -0.0078 & 0.0158 & 09998 \end{bmatrix} \text{ and } \tilde{\mathbf{b}}_{(30,30)\rightarrow(40,40)} = \begin{bmatrix} 0.6082 \\ -0.4836 \\ -0.3003 \end{bmatrix} \quad [13]$$

Equation [14] is the transformation calculated with ICP for the data from Figure 4.14B. At convergence of ICP the mean distance between closest points was 5 cm.

$$\mathbf{A}_{(30,30)\rightarrow(40,40)} = \begin{bmatrix} 1.0000 & 0.0042 & -0.0081 \\ -0.0042 & 1.0000 & -0.0008 \\ 0.0081 & -0.0031 & 1.0000 \end{bmatrix} \text{ and } \tilde{\mathbf{b}}_{(30,30)\rightarrow(40,40)} = \begin{bmatrix} 0.2600 \\ -0.1206 \\ -0.2800 \end{bmatrix} \quad [14]$$

As a check of the registration methods the Equation [13] and Equation [14] transformations were applied to the extracted bole sections from node (30, 30) (see Figure 4.11) with the results presented in Figure 4.15. The transformation estimated with the stem centers from (40, 40) (Equation [14]) resulted in a visually more accurate alignment of the scanner data

(Figure 4.15B). The transformation in Equation [14] had a lower final mean distance between closest at ICP convergence than the transformation in Equation [13]. For this research the between node registration resulting in the smaller mean distance between closest at ICP convergence was used to align node-level point clouds.

The alignment of EBSs in Figure 4.15B appears accurate in the X- and Y-directions but was not completely accurate in the Z-direction. The bottoms of the EBSs from different nodes were not aligned and numerous branches along the boles were not at corresponding heights. These registration errors as well as the possibility of inaccurate tilting of one point cloud relative to another necessitated the ground registration step.

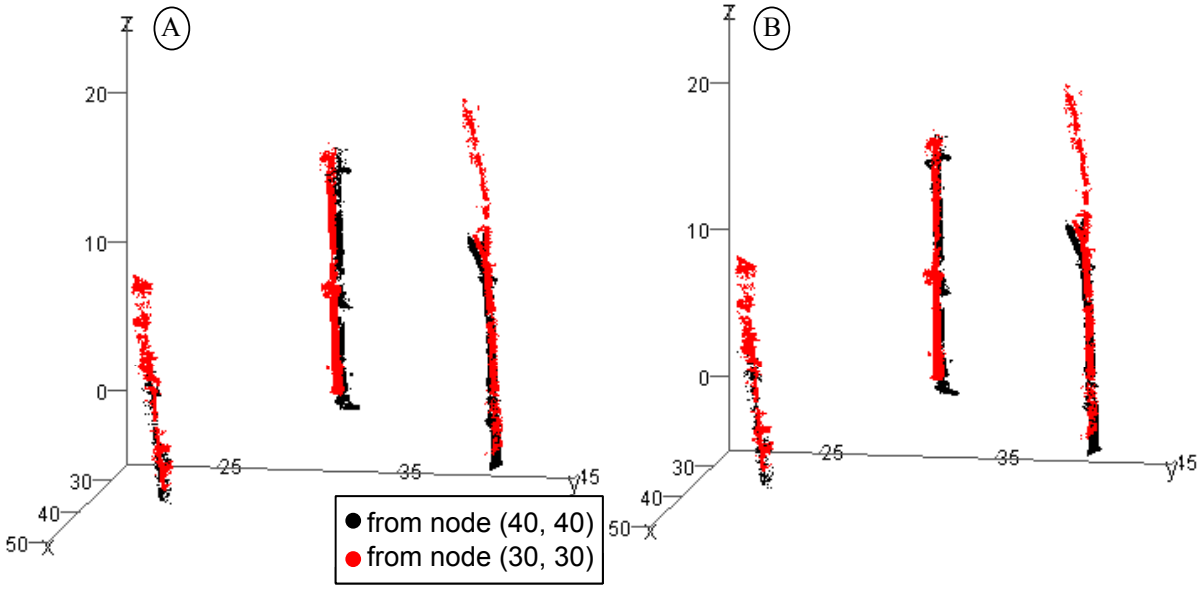

Figure 4.15. The alignment of the registered bole sections from node (30, 30) using the registrations calculated with the stem centers from node (30, 30) interpolated (A) or the stem centers from node (40, 40) interpolated (B).

4.3.7 Ground surface registration

Ground surface registration was only performed for the leaf-on scans because minimal tilting was observed in the leaf-off scans and the limited field of view of those scans did not consistently provide enough ground points for registration. The ground registration was performed 14 times to get the ground surface from all nodes aligned with the ground surface of the center node at (50, 40). Table 4.9 contains a summary of the area of overlap and the number of points used in each registration. The area of ground overlap varied between registrations

because the ground surface was found for the 30 m × 30 m area surrounding each scanner. The overlap of the ground between nodes registered diagonally was less than the overlap for nodes that were immediately adjacent. An area of overlap of 20 m × 20 m meant 400 ground surface points could potentially be available for registration. An area of overlap of 20 m × 30 m resulted in 600 ground surface points potentially available for registration. The average number of common ground surface points found was 388 for 20 m × 20 m areas of overlap and 558 for 20 m × 30 m areas of overlap.

Table 4.9. Summary of the data used for ground registrations. The "ground points available" is the number of points at the same XY positions in paired ground surfaces.

Node being registered	Ground points available	Node registered to	Area of overlap
(30, 30)	382	(40, 40)	20 m × 20 m
(30, 40)	577	(40, 40)	20 m × 30 m
(30, 50)	386	(40, 40)	20 m × 20 m
(40, 30)	386	(50, 40)	20 m × 20 m
(40, 40)	548	(50, 40)	20 m × 30 m
(40, 50)	355	(50, 40)	20 m × 20 m
(50, 30)	507	(50, 40)	30 m × 20 m
(50, 50)	552	(50, 40)	30 m × 20 m
(60, 30)	381	(50, 40)	20 m × 20 m
(60, 40)	568	(50, 40)	20 m × 30 m
(60, 50)	353	(50, 40)	20 m × 20 m
(70, 30)	390	(60, 40)	20 m × 20 m
(70, 40)	547	(60, 40)	20 m × 30 m
(70, 50)	353	(60, 40)	20 m × 20 m

Figure 4.16 contains the estimated ground surface height from the registered node-level point clouds from node (50, 40) and (50, 30). The ground estimates from (50, 40) were presented as a surface model to make the image easier to understand. The area of overlap was 30 m × 20 m. The ground was found for 507 corresponding XY positions in both ground surface data sets. The ground from node (50, 30) was tilted relative to the node (50, 40) data with the corner near (65, 25) being lower than the (50, 40) surface model and the corner near (35, 45) being higher than the (50, 40) surface model.

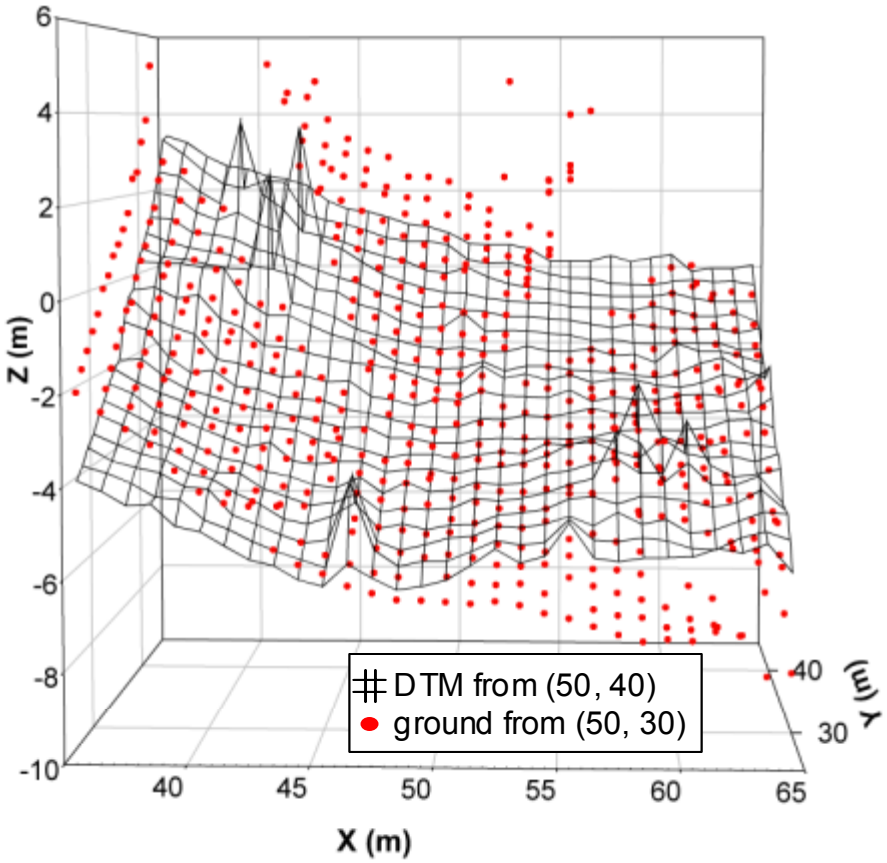

Figure 4.16. Ground surfaces from (50, 40) and (50, 30) node-level point clouds. Data sets were used with ICP to calculate a transformation to align ground surfaces.

Equation [15] contains transformation parameters calculated with ICP using the ground surfaces from nodes (50, 40) and (50, 30) (Figure 4.16).

$$A_{(50,30)\rightarrow(50,40)} = \begin{bmatrix} 0.9922 & 0.03369 & -0.1199 \\ -0.0231 & 0.995772 & 0.0089 \\ 0.1223 & -0.0855 & 0.9888 \end{bmatrix} \text{ and } \tilde{b}_{(50,30)\rightarrow(50,40)} = \begin{bmatrix} -1.0571 \\ 1.7970 \\ -3.5033 \end{bmatrix} \quad [15]$$

The application of the transformation parameters in Equation [15] to the ground surface from node (50, 30) resulted in the alignment presented in Figure 4.17. Visual inspection reveals improved alignment of the ground surfaces.

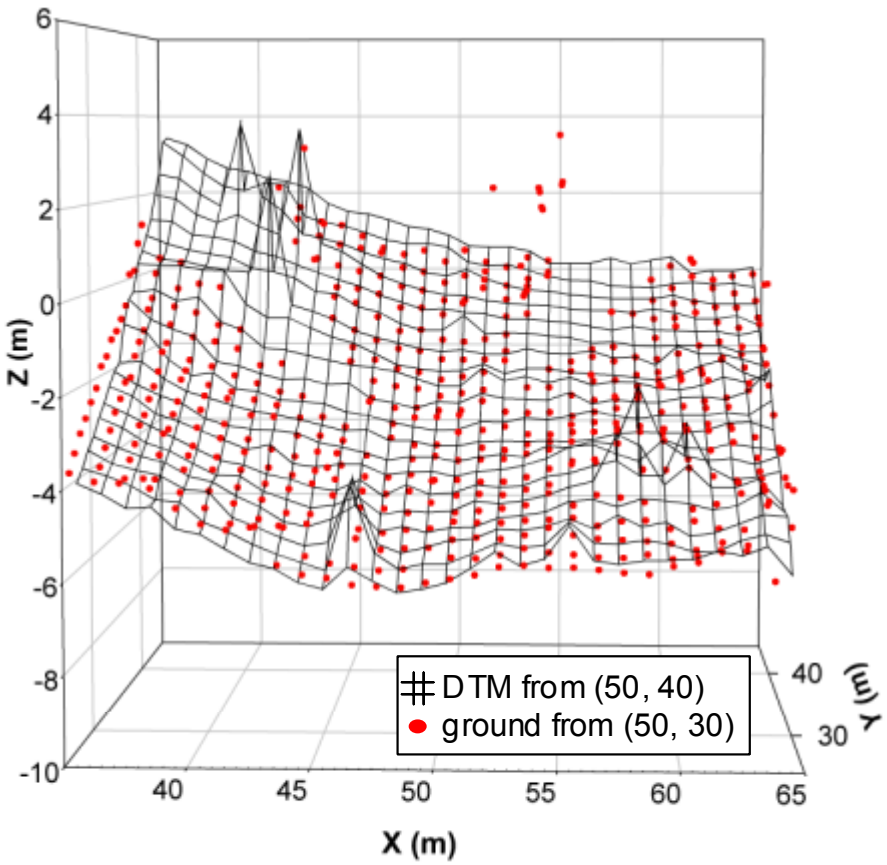

Figure 4.17. Aligned ground surfaces from (50, 40) and (50, 30) node-level point clouds. Alignment was performed with the ICP estimated transformation parameters in Equation [15].

4.3.8 Sequential application of registrations

The registration steps described thus far calculate all the transformation parameters necessary to get all scans aligned with the node-level point cloud from node (50, 40). To actually align the point clouds numerous $\mathbf{A}$ rotations and $\tilde{\mathbf{b}}$ translations had to be applied in sequence. The number and order of transformation parameters necessary varied depending on the scan being aligned.

Table 4.10 and Table 4.11 indicate the ICP estimated parameter sets and the order of their sequential application necessary to align each coarsely registered point cloud to the node (50, 40) point cloud, for leaf-on and leaf-off data sets, respectively. Applications of secondary between node and ground registrations were necessary for nodes that could not be directly registered to data from node (50, 40) (see Figure 2.6). A final adjustment to the plot coordinates (as defined in

the following section) was included to complete the alignment of all scanner data to the field plot.

The leaf-off data had eight scans requiring the application of 3 ICP derived transformations; thirty scans requiring the application of two ICP derived transformations; two scans requiring one ICP derived transformation and one scan requiring no ICP derived transformations. The leaf-on data had twelve scans requiring the application of five ICP derived transformations, six scans requiring four ICP derived transformations, sixteen scans requiring three ICP derived transformations, eight scans requiring two ICP derived transformations, two scans requiring one ICP derived transformation and one scan requiring no ICP derived transformations.

The Appendix includes final $\mathbf{A}$ rotations and $\widetilde{\mathbf{b}}$ translations necessary to align each raw point cloud to the field plot. Final $\mathbf{A}$ rotations and $\widetilde{\mathbf{b}}$ translations were calculated by algebraically combining the coarse registrations, ICP registrations and the final adjustment to the field plot. The mean distance between closest points at convergence for ICP registrations are included in the Appendix as well.

Table 4.10. The ICP registrations, applied sequentially left to right to each scan to align that scan's point cloud to the point cloud data from node (50, 40), for leaf-on scans.

Node	Scan	Within node Registration	Primary between node registration	Secondary between node registration	Primary ground registration	Secondary ground registration
(30, 30)	1	-				
(30, 30)	2	2→1	(30, 30)→(40, 40)	(40, 40)→(50, 40)	(30, 30)→(40, 40)	(40, 40)→(50, 40)
(30, 30)	3	3→1				
(30, 40)	1	-				
(30, 40)	2	2→1	(30, 40)→(40, 40)	(40, 40)→(50, 40)	(30, 40)→(40, 40)	(40, 40)→(50, 40)
(30, 40)	3	3→1				
(30, 50)	1	-				
(30, 50)	2	2→1	(30, 50)→(40, 40)	(40, 40)→(50, 40)	(30, 50)→(40, 40)	(40, 40)→(50, 40)
(30, 50)	3	3→1				
(40, 30)	1	-				
(40, 30)	2	2→1	(40, 30)→(50, 40)	-	(40, 30)→(50, 40)	-
(40, 30)	3	3→1				
(40, 40)	1	-				
(40, 40)	2	2→1	(40, 40)→(50, 40)	-	(40, 40)→(50, 40)	-
(40, 40)	3	3→1				
(40, 50)	1	-				
(40, 50)	2	2→1	(40, 50)→(50, 40)	-	(40, 50)→(50, 40)	-
(40, 50)	3	3→1				
(50, 30)	1	-				
(50, 30)	2	2→1	(50, 30)→(50, 40)	-	(50, 30)→(50, 40)	-
(50, 30)	3	3→1				
(50, 40)	1	-				
(50, 40)	2	2→1	-	-	-	-
(50, 40)	3	3→1				
(50, 50)	1	-				
(50, 50)	2	2→1	(50, 50)→(50, 40)	-	(50, 50)→(50, 40)	-
(50, 50)	3	3→1				
(60, 30)	1	-				
(60, 30)	2	2→1	(60, 30)→(50, 40)	-	(60, 30)→(50, 40)	-
(60, 30)	3	3→1				
(60, 40)	1	-				
(60, 40)	2	2→1	(60, 40)→(50, 40)	-	(60, 40)→(50, 40)	-
(60, 40)	3	3→1				
(60, 50)	1	-				
(60, 50)	2	2→1	(60, 50)→(50, 40)	-	(60, 50)→(50, 40)	-
(60, 50)	3	3→1				
(70, 30)	1	-				
(70, 30)	2	2→1	(70, 30)→(60, 40)	(60, 40)→(50, 40)	(70, 30)→(60, 40)	(60, 40)→(50, 40)
(70, 30)	3	3→1				
(70, 40)	1	-				
(70, 40)	2	2→1	(70, 40)→(60, 40)	(60, 40)→(50, 40)	(70, 40)→(60, 40)	(60, 40)→(50, 40)
(70, 40)	3	3→1				
(70, 50)	1	-				
(70, 50)	2	2→1	(70, 50)→(60, 40)	(60, 40)→(50, 40)	(70, 50)→(60, 40)	(60, 40)→(50, 40)
(70, 50)	3	3→1				

Table 4.11 The ICP registrations, applied sequentially left to right to align each scan's point clouds to the data from node (50, 40), for leaf-off scans.

Node	Scan	Within node Registration	Primary between node registration	Secondary between node registration
(30, 30)	1	-	(30, 30)→(40, 40)	(40, 40)→(50, 40)
(30, 30)	2	2→1		
(30, 40)	1	-		
(30, 40)	2	2→1	(30, 40)→(40, 40)	(40, 40)→(50, 40)
(30, 40)	3	3→1		
(30, 50)	1	-	(30, 50)→(40, 40)	(40, 40)→(50, 40)
(30, 50)	2	2→1		
(40, 30)	1	-		
(40, 30)	2	2→1	(40, 30)→(50, 40)	-
(40, 30)	3	3→1		
(40, 40)	1	-		
(40, 40)	2	2→1	(40, 40)→(50, 40)	-
(40, 40)	3	3→1		
(40, 50)	1	-		
(40, 50)	2	2→1	(40, 50)→(50, 40)	-
(40, 50)	3	3→1		
(50, 30)	1	-		
(50, 30)	2	2→1	(50, 30)→(50, 40)	-
(50, 30)	3	3→1		
(50, 40)	1	-		
(50, 40)	2	2→1	-	-
(50, 40)	3	3→1		
(50, 50)	1	-		
(50, 50)	2	2→1	(50, 50)→(50, 40)	-
(50, 50)	3	3→1		
(60, 30)	1	-		
(60, 30)	2	2→1	(60, 30)→(50, 40)	-
(60, 30)	3	3→1		
(60, 40)	1	-		
(60, 40)	2	2→1	(60, 40)→(50, 40)	-
(60, 40)	3	3→1		
(60, 50)	1	-		
(60, 50)	2	2→1	(60, 50)→(50, 40)	-
(60, 50)	3	3→1		
(70, 30)	1	-	(70, 30)→(60, 40)	(60, 40)→(50, 40)
(70, 30)	2	2→1		
(70, 40)	1	-		
(70, 40)	2	2→1	(70, 40)→(60, 40)	(60, 40)→(50, 40)
(70, 40)	3	3→1		
(70, 50)	1	-	(70, 50)→(60, 40)	(60, 40)→(50, 40)
(70, 50)	2	2→1		

Equation [16] depicts an example of the sequential application of transformation parameters algebraically combined to align the leaf-on data for node (30, 30) scan 2 to the leaf-on node (50, 40) point cloud.

$$
\begin{aligned}
T_{(30,30)_2\rightarrow(50,40)}(\tilde{\mathbf{p}}_{(30,30)_2}) = \mathbf{A}_{\mathrm{G}(40,\,40)\rightarrow\mathrm{G}(50,40)}(\mathbf{A}_{\mathrm{G}(30,\,30)\rightarrow\mathrm{G}(40,40)}(\mathbf{A}_{(40,\,40)\rightarrow(50,40)} \\
(\mathbf{A}_{(30,\,30)\rightarrow(40,40)}(\mathbf{A}_{(30,\,30)_2\rightarrow(30,30)_1}(\mathbf{A}_{\mathrm{coarse}}\tilde{\mathbf{p}}_{(30,30)_2} + \tilde{\mathbf{b}}_{\mathrm{coarse}}) + \\
\tilde{\mathbf{b}}_{(30,\,30)_2\rightarrow(30,30)_1}) + \tilde{\mathbf{b}}_{(30,\,30)\rightarrow(40,40)}) + \tilde{\mathbf{b}}_{(40,\,40)\rightarrow(50,40)}) + \\
\tilde{\mathbf{b}}_{\mathrm{G}(30,\,30)\rightarrow\mathrm{G}(40,40)}) + \tilde{\mathbf{b}}_{\mathrm{G}(40,\,40)\rightarrow\mathrm{G}(50,40)} \\
= \mathrm{A}_{(30,30)_2\rightarrow(50,40)}\tilde{\mathbf{p}}_{(30,30)_2} + \tilde{\mathrm{b}}_{(30,30)_2\rightarrow(50,40)}
\end{aligned}
\qquad [16]
$$

where:

$T_{(30,30)_2\rightarrow(50,40)}(\tilde{\mathbf{p}}_{(30,30)_2})$ = data from node (30, 30) scans transformed to align with the data from node (50, 40)

$\tilde{\mathbf{p}}_{(30,30)_2}$ = untransformed point cloud data from scan 2 at node (30, 30)

$\mathbf{A}$ = 3 × 3 rotation matrix

$\tilde{\mathbf{b}}$ = translation 3 vector

and subscripts refer to:

coarse = coarse registration

$(30, 30)_2\rightarrow(30, 30)_1$ = EBS surface-based ICP registration of scan 2 to scan 1 at (30, 30)

(30, 30)→(40, 40) = EBS center-based ICP registration of (30, 30) to (40, 40)

(40, 40)→(50, 40) = EBS center-based ICP registration of (40, 40) to (50, 40)

G(30, 30)→G(40, 40) = ground surface based ICP registration of (30, 30) to (40, 40)

G(40, 40)→G(50, 40) = ground surface based ICP registration of (40, 40) to (50, 40)

$(30, 30)_2\rightarrow(50, 40)$ = combined registrations to align scan 2 from (30, 30) to the node (50, 40) point cloud

4.3.9 Final adjustment to plot coordinates

To maximize correspondence between scanner data and Coweeta tree survey data a final alignment step was necessary. The scanner locations within the registered data were determined by applying the combined sequential coarse and ICP registrations for each scan to the point (0, 0, 0). Figure 4.18 depicts the scanner locations in the registered scanner data and the field plot nodes. Optimally scanner locations from the scan data would be located directly over the field plot nodes.

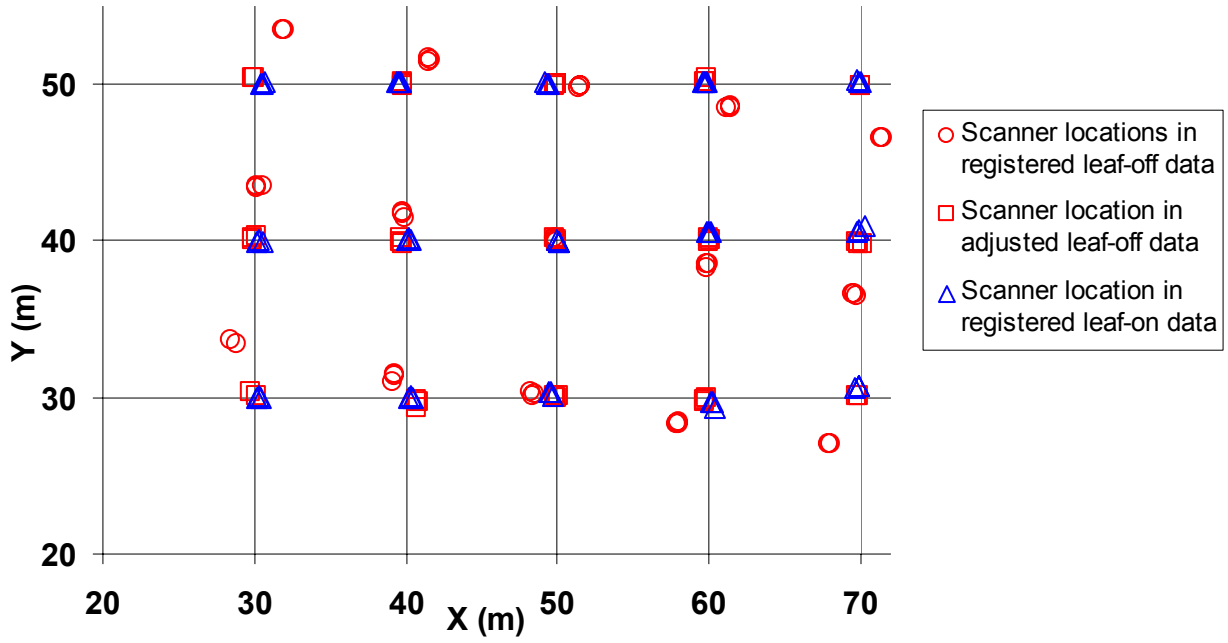

Figure 4.18. Locations of the scanner relative to the registered plot data for leaf-off and leaf-on data. The leaf-off data required an adjustment to match the field plot nodes.

The average horizontal distance between scanner locations from the registered leaf-on data and the monumented plot nodes was 0.4 m and no patterns were observed in the direction or magnitude of the errors relative to the plot. So no adjustment of the leaf-on plot-level point cloud was necessary.

The average horizontal distance between scanner locations from the registered leaf-off data and the monumented plot nodes was 2.3 m and the scanner locations from the leaf-off data appeared to be rotated relative to the plot. The plot-level, leaf-off point cloud was rotated about point (50, 40) through an angle that minimized the median distance between scanner locations

from the leaf-off data and the monumented nodes. This angle was calculated as a counter-clockwise rotation of 9.3° about (50, 40) and was applied to all the leaf-off registered point clouds. The average horizontal distance between scanner locations from the registered leaf-off data and the monumented nodes following the application of this adjustment was 0.3 m.

This adjustment was the last step necessary to align all leaf-off and leaf-on scans to the field plot coordinate system. The final adjustment was included in the final calculated **A** rotation matrices and $\tilde{\mathbf{b}}$ translation vectors included in the Appendix.

4.3.10 Time to complete registration

The total time to complete the stepwise registration of the point-cloud data for the leaf-off or leaf-on data sets was approximately 12 days. All registration steps were performed on a desktop computer with a 1ghz Intel® Pentium III® processor and 512 KB of RAM. The automated extraction of trees from individual scans took approximately 12 hours or 15 to 20 minutes per scan. The automated extraction of trees from node-level point clouds typically took an hour per node or approximately 16 hours for all nodes. The applications of the center finder algorithm to all EBSs from the scan and node, leaf-off and leaf-on data required 2 to 3.5 days and was dependent on the number of EBSs and the number of points representing each EBS. Confirmation of paired EBSs for both within and between node registrations required 16 hours of software-aided processing by a human operator.

The ICP registrations using bole surfaces required 12 hours of computer time for all registrations to reach convergence. The calculation of the transformation parameters using ICP took a total of one to two hours for within or between node registrations when using stem centers. The ground registration step, including finding ground surfaces from different nodes and applying ICP was completed in 8 hours. Additional time was necessary to manage the data files and apply transformation parameters between steps.

4.4 Evaluation and assessment of DTMs and CTSMs

As points of reference for creation of light availability models and as unique products of the scanner the following digital terrain models (DTMs) and canopy top surface models

(CTSMs) were created. It was assumed that a 0.25 m raster type data set would be useful for the proposed applications. A key tool for addressing this assumption was the examination of 3D representations of the CTSMs and DTMs (Figure 4.19, Figure 4.20 and Figure 4.21). The interior plot DTMs and CTSM consisted of 12,800 cells while the 10 m buffer region consisted of 25,600 cells and the 5 m buffer-region consisted of 11,200 cells.

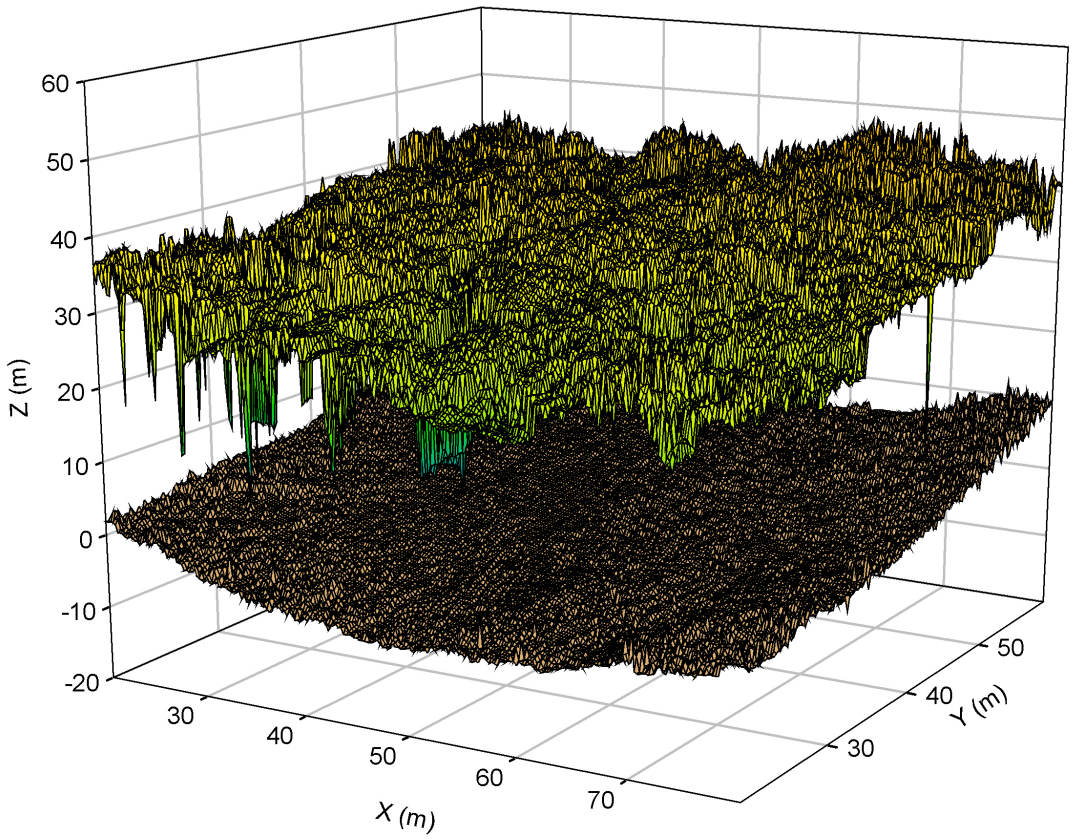

Figure 4.19. DTM and CTSM created from leaf-on scans, including a 10 m buffer region surrounding the interior plot. A cell size of 0.25 m was used.

A comparison of Figure 4.19 and Figure 4.20 reveals differences in the appearance of the DTM and CTSM over the buffer region and the interior plot. The CTSM appears relatively jagged near the outside edges of the 10 m buffer. Differences were also observed when comparing surfaces near the buffer to the surfaces near the middle of the plot, where the scan data were most dense. Similar observations were made for the 5 m buffer area used for the leaf-off CTSM and DTM (not pictured). The CTSM obtained during leaf-off (Figure 4.21) had a smoother appearing surface than the CTSM obtained during leaf-on.

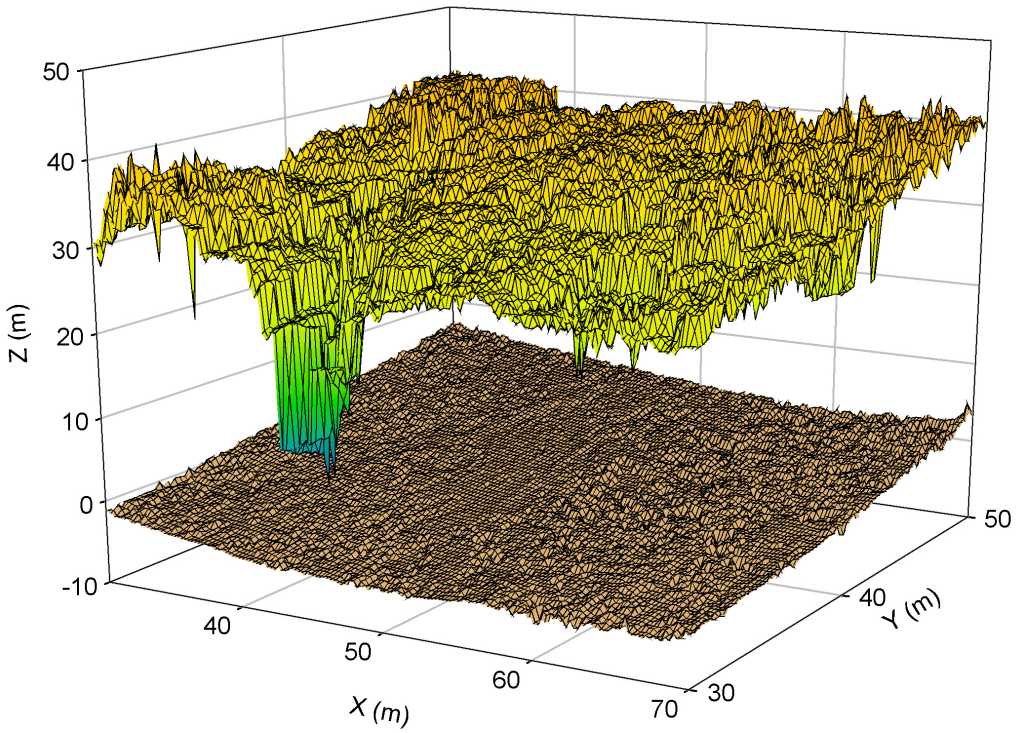

Figure 4.20. DTM and CTSM created from leaf-on scans for the interior plot. A cell size of 0.25 m was used.

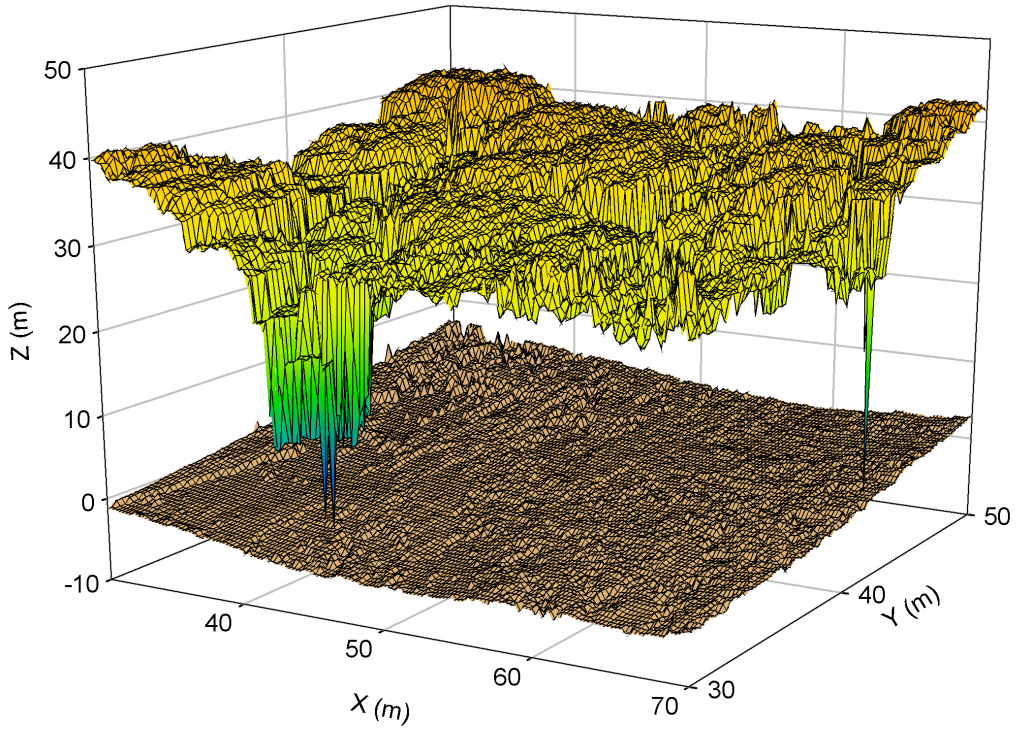

Figure 4.21. DTM and CTSM created from leaf-off scans for the interior plot. A cell size of 0.25 m was used.

It was possible to compare leaf-off and leaf-on models by examining the differences in relative elevation estimated in the CTSM and DTM for common cells. The differences between the leaf-on and leaf-off models (d_{xy}) were calculated as in Equation [17].

$$d_{xy} = Z_{xy(summer)} - Z_{xy(winter)} \quad [17]$$

Where $Z_{xy(leaf\text{-}on)}$ and $Z_{xy(leaf\text{-}off)}$ were the estimated Zs from cells at location XY in a DTM or CTSM from the leaf-on and leaf-off scans, respectively. Bias was introduced by the scanner height at node (50, 40), the height of 0 m in the models, not being the same during leaf-on and leaf-off measurements. The median difference between the DTMs in Figure 4.20 and Figure 4.21 was determined and DTMs and CTSMs were adjusted in the Z-direction to eliminate this bias. In this case the median difference was 0.414 m. This adjustment was calculated using only the interior plot, ignoring buffer zones.

Relatively small values for d_{xy} indicate good agreement between the models obtained during leaf-on and leaf-off conditions. A positive d_{xy} indicates a higher Z-value was found for a given cell from the leaf-on scans than was found for the same cell from the leaf-off scans. The d_{xy}s for the leaf-off and leaf-on DTMs (Figure 4.20 and Figure 4.21) ranged from -2.05 m to 2.53 m and had a standard deviation of 0.42 m. For the 5 m buffer-region that the leaf-on and leaf-off DTMs have in common, the range of d_{xy}s was -4.56 m to 3.21 m with a standard deviation of 0.66 m. In the buffer region the median d_{xy} was -0.08 m while this value was 0 m for the interior plot DTM because of the bias adjustment. The values of d_{xy} for the DTMs increased with increasing distance from the center of the interior plot (Figure 4.22).

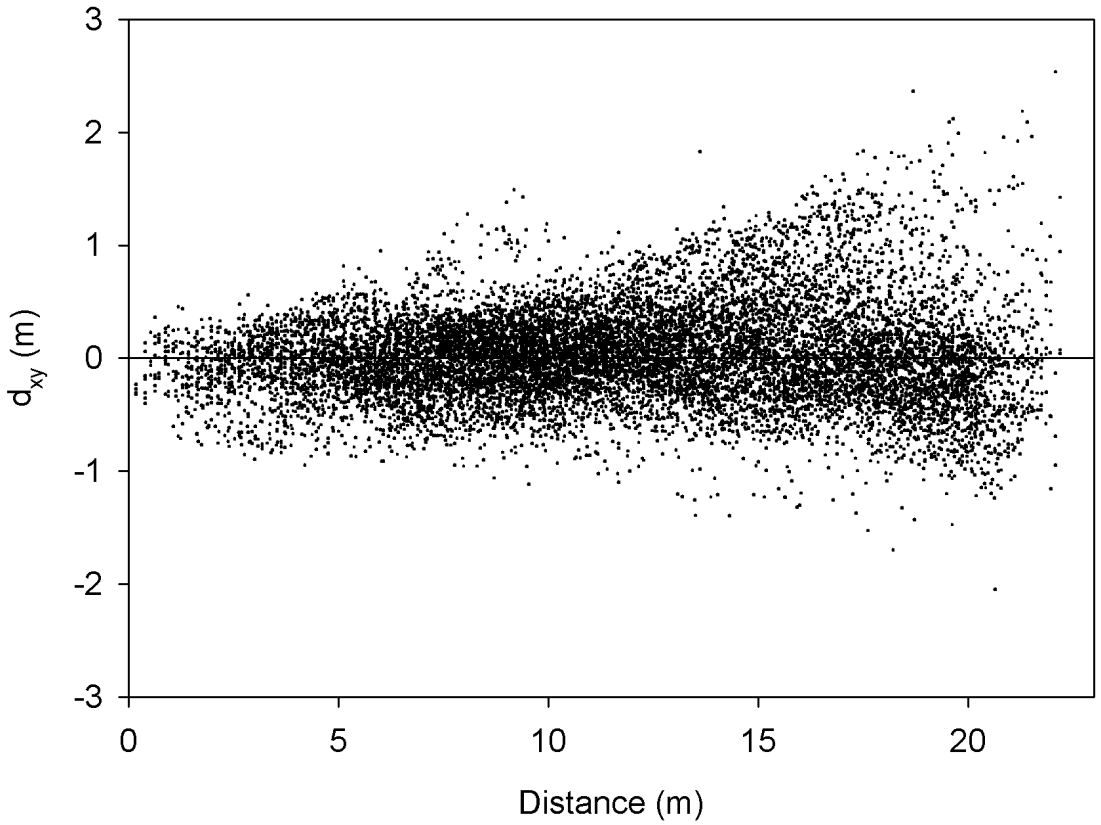

Figure 4.22. d_{xy} values for the DTMs relative to the distance in the XY-plane of cells from the central scanner location at node (50, 40). Values are for the interior plot only.

The d_{xy} values calculated for the CTSM ranged from –26.5 m to 30.4 m in the buffer and -18.0 m to 35.4 m for the interior plot. The median d_{xy} for the interior plot CTSM was -0.27 m while the median d_{xy} for the buffer CTSM was –0.67 m. The standard deviation of the d_{xy} for the interior plot CTSM was 2.7 m while the standard deviation for the d_{xy} of the buffer CTSM was 3.1 m

The CTSMs and DTMs generally had less agreement between leaf-on and leaf-off conditions in the buffer regions where the density of the scanner data was significantly lower. The negative median d_{xy} for the CTSM comparison indicates that a generally higher canopy was found using the leaf-off scanner data.

Further evaluation of the accuracy of the DTMs was possible through comparisons to the slope of interior plot boundaries calculated from onsite GPS measurements (Figure 4.23). GPS measurements of the interior plot corners were available on the Coweeta LTER Data Search website (Kloeppel et al. 2003). The GPS measurements were collected using a Trimble Pro-XRS

12-channel DGPS (Kloeppel et al. 2003). In general the slopes from leaf-on and leaf-off data were within one weighted standard deviation of the slopes obtained using the GPS measurements (Figure 4.23). The lack of agreement between the slopes obtained for the plot boundary between (70, 50) and (30, 50) was minimal and could be due to inaccuracy of the GPS measurements as well as inaccuracy of the DTM corners. This was a coarse comparison based on only four measurement points from each data source.

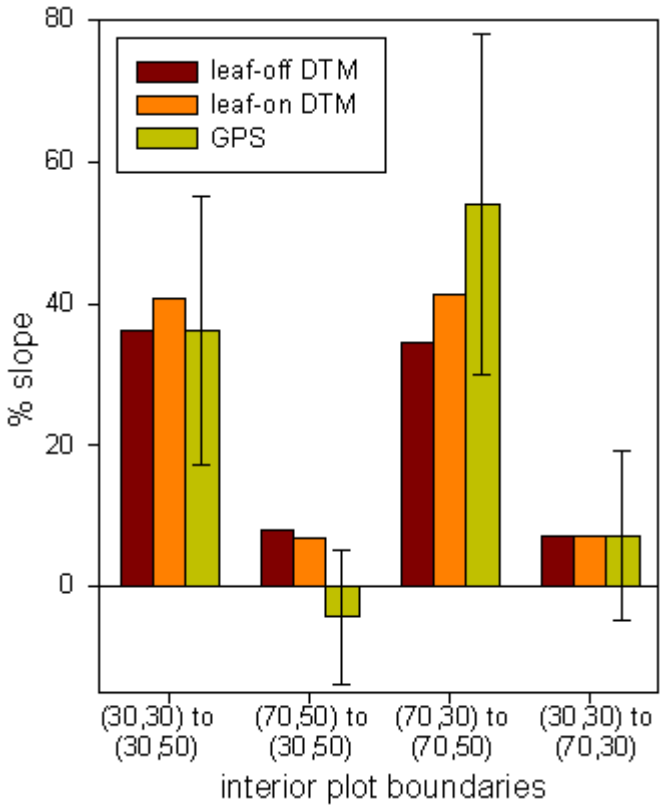

Figure 4.23. Comparison of slopes obtained using the corners of the leaf-on DTM, leaf-off DTM and on-site GPS measurements. Errors bars on the GPS measurements represent the average weighted standard deviation for the given corner locations. The error bars nominally represent ±1 standard deviation in the vertical direction.

4.5 Evaluation and assessment of CHMs

CHMs were calculated as the difference between the CTSM and the DTM. A number of summary statistics were calculated from the CHMs and are presented in Table 4.12. The leaf-on and leaf-off CHMs (Figure 4.24 and Figure 4.25) derived from the pairs of CTSMs and DTMs in Figure 4.20 and Figure 4.21 showed a high degree of agreement.

Table 4.12. Summary statistics derived from leaf-on and leaf-off CHMs

	Leaf-on CHM	Leaf-off CHM
Maximum ht (m)	41.9	41.8
Minimum ht (m)	8.4	0.7
Mean ht (m)	34.0	34.1
Standard Deviation of ht (m)	3.00	3.44

As with the evaluation of the CTSMs and DTMs it was possible to calculate d_{xy} values between leaf-on and leaf-off CHMs using Equation [17]. The d_{xy} values ranged from –17.8 m to 35.5 m with a median of –0.30 m and a standard deviation of 2.7 m. The largest d_{xy} values were generally found around regions of the CHM where the height changed rapidly over a relatively short distance, as in the apparent canopy gap near the coordinates (45 m, 30 m) in Figure 4.24 and Figure 4.25.

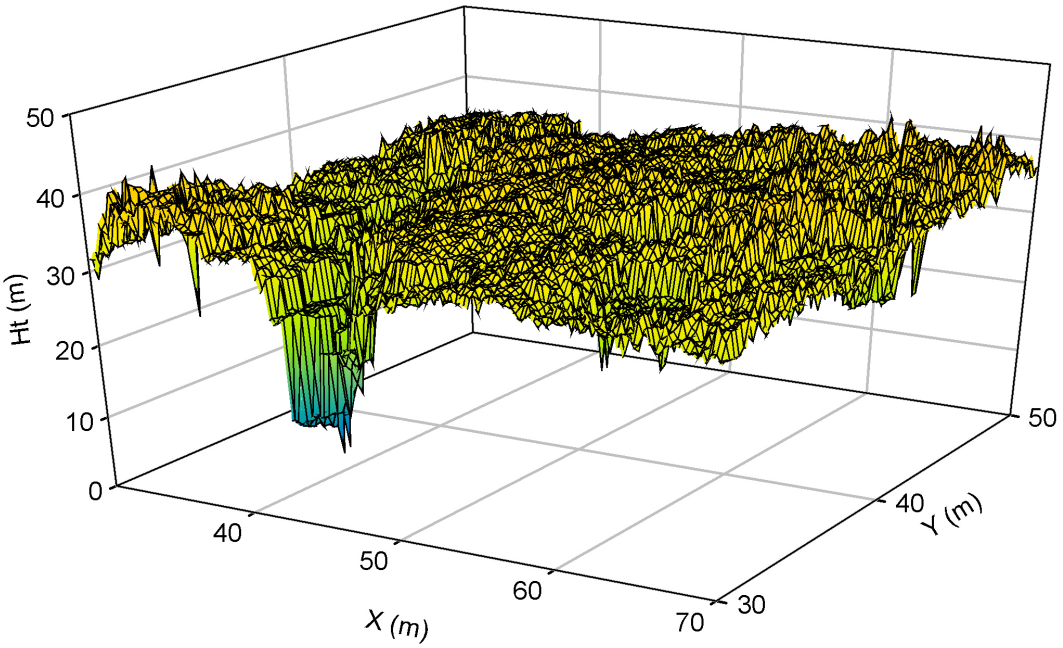

Figure 4.24. Leaf-on CHM calculated as the difference between the leaf-on CTSM and DTM. A cell size of 0.25 m was used.

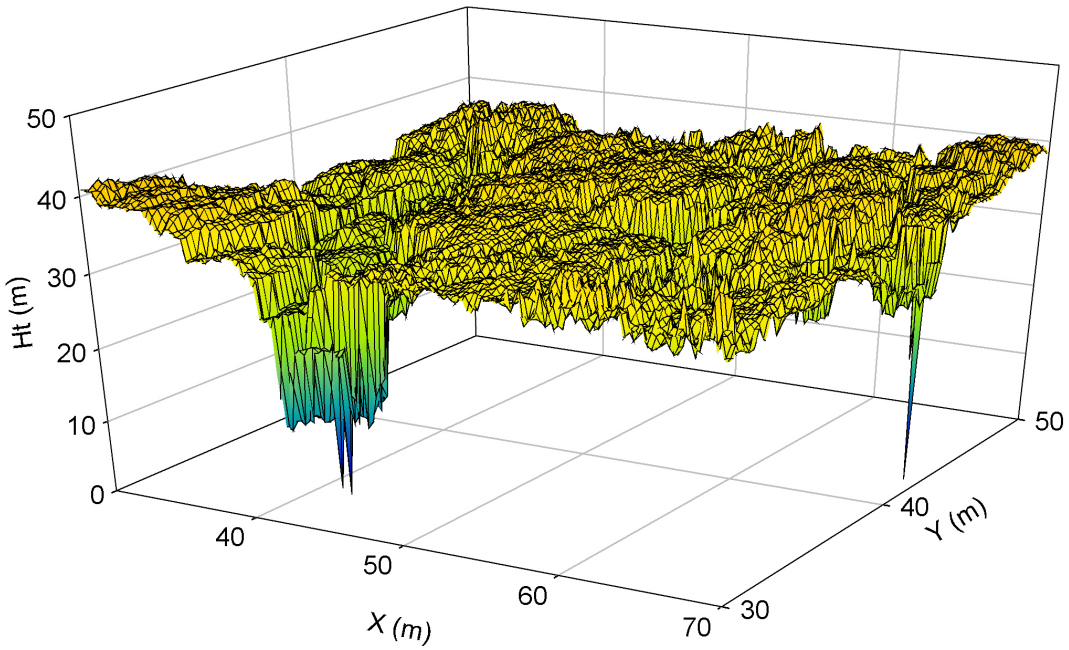

Figure 4.25. Leaf-off CHM calculated as the difference between the leaf-on CTSM and DTM. A cell size of 0.25 m was used

4.6 Reclassification of point cloud into cubes

The relative densities of intercepted surfaces represented in the cubic cell reclassification of the registered point clouds were used to evaluate and quantify occlusion. These results are directly related to how well the reclassified data performed in summarizing the distribution of canopy structure.

The reclassifications were performed using cubic cells with sizes of 1 m, 0.5 m, and 0.25 m on a side, for both the leaf-on and leaf-off plot-level point clouds. The cube data sets were limited in the vertical direction to exclude cubes entirely above the CTSM and cubes below 0.5 m above the DTM. The 0.5 m buffer above the DTM was necessary to exclude cubes that were highly occluded because they were wholly or largely below the ground level. Also cubes containing many points representing the ground were not useful in measuring canopy structure. The cube data sets were collected over the interior with plot with a 5 m buffer beyond the plot borders. The interior plot was 0.08 ha and the interior plot with 5 m buffer was nearly twice as large at 0.15 ha.

Table 4.13 contains a summary of the total number of cubes necessary to reclassify the leaf-on and leaf-off data at various resolutions. The numbers of cubes necessary for leaf-on and leaf-off differ because the leaf-off and leaf-off DTMs and CTSMs were not identical. For comparison and evaluation of the reclassification in data reduction, the total number of range measurements making up all 45 of the leaf-on scans was 29,970,000.

Table 4.13. Number of cubes necessary to reclassify leaf-on and leaf-off data sets at examined resolutions for the interior plot and the interior plot with a 5 m buffer.

Plot-level data set	Cube size	Cubes over interior plot	Cubes over buffered plot
leaf-off	1 m	27,679	52,493
leaf-on	1 m	27,741	52,232
leaf-off	0.5 m	217,967	414,155
leaf-on	0.5 m	218,170	410,663
leaf-off	0.25 m	1,719,740	3,271,117
leaf-on	0.25 m	1,714,337	3,225,395

4.6.1 Occlusion results from cell data

To examine occlusion the percent occlusion was calculated using the counts of obstructed (O), pass-through (PT) and intercepted (I) pulses for each cube as indicated in Equation [18].

$$\% \text{ occlusion} = O / (O + PT + I) \quad [18]$$

This is a measure of what percentage of the laser pulses aimed at a given cube (from all scanner locations) were intercepted before reaching that cube. The higher the percent occlusion the fewer laser pulses actually reached a given cube. It was also useful to know the maximum number of pulses that could reach a cube if there was no occlusion. This value was the sum of obstructed, pass-through and intercepted pulses.

For comparison “non-overlapping” reclassified data sets were created where the values for each cube were only calculated using range measurements from the nearest node. This data set did not make use of the overlapping nature of the scans from different nodes. To create this dataset counts of intercepted, obstructed and pass-through pulses for each cube were made using

only the data from the nearest node. These non-overlapping data sets were created at the 1 m cubes size for leaf-off and leaf-on data.

Table 4.14 contains a summary of the reclassified data sets using the 1 m cube size. The percentage of cubes that were less than 50% occluded was relatively constant across leaf-on data sets and relatively constant across leaf-off data sets. The percentage of cubes that were greater than 90%, or completely occluded was similar between the buffer and interior plot data sets. The percentage of cubes that were greater than 90% or completely occluded was significantly higher for the "non-overlapping" data sets.

The maximum number of pulses that could reach a cube was lower in the buffer and the non-overlapping data set. The median percent occlusion values were similar for all leaf-on or all leaf-off data sets with the exception of the non-overlapping, leaf-off data.

Table 4.14. Comparison of the cube reclassification for the interior plot, buffer and the non-overlapping data sets at the 1 m cube size resolution. Values were calculated across all cubes for the given data set.

		% of total number of cubes that are				Number of pulses aimed at each cube		
Scan conditions	Data set	completely occluded	>90% occluded	<50% occluded	Median % occluded	median	1st percentile	minimum
leaf-off	interior plot	0.00%	2.52%	81.12%	22.19%	9,613	1,351	865
leaf-off	buffer	0.00%	2.85%	79.21%	24.18%	3,463	823	358
leaf-off	non-overlapping	0.48%	5.53%	77.80%	9.12%	1,508	268	191
leaf-on	interior plot	0.11%	10.96%	50.22%	49.82%	8,455	1,308	816
leaf-on	buffer	0.13%	9.19%	49.95%	50.03%	5,589	1,112	762
leaf-on	non-overlapping	8.20%	25.27%	49.30%	51.27%	1,336	257	181

Table 4.15 contains a summary of the reclassified data sets for the interior plot using both the leaf-on and leaf-off data for 1 m, 0.5 m and 0.25 m cube sizes. The percentage of cubes at various levels of occlusion and the median percent occlusion for the cubes are consistent across the range of cubes sizes within the leaf-off data and leaf-on data, respectively. The leaf-on data have a higher percentage of cubes that are greater than 90% occluded or are totally occluded than the leaf-off data. The median percent occluded was lower in the leaf-off data than in the leaf-on. The number of pulses aimed at a given cell decreased with smaller cube sizes. For the smallest cube sizes the 1st percentile value of 92 for leaf-on conditions meant that for 1% of the cubes no

more than 92 of the range measurements from all of the scans were taken at an angle that could intercept that cube.

Table 4.15. Comparison of the cube reclassification for the interior plot using various cube sizes under leaf-on and leaf-off conditions. The values were calculated across all cubes for the given data set.

		% of total number of cubes that are				Number of pulses aimed at each cube		
Scan conditions	Cube size	completely occluded	>90% occluded	<50% occluded	median % occluded	median	1st percentile	min
leaf-off	1.0 m	0.00	2.52	81.12	22.19	9,613	1,351	865
leaf-off	0.5 m	0.01	2.42	81.74	22.04	2,499	346	214
leaf-off	0.25 m	0.10	2.24	82.20	21.62	647	88	49
leaf-on	1.0 m	0.11	10.96	50.22	49.82	8,455	1,308	816
leaf-on	0.5 m	0.34	10.16	50.11	49.91	2,198	346	198
leaf-on	0.25 m	0.93	9.15	50.61	49.58	572	92	41

Figure 4.26 relates the amount of occlusion to the height above ground using the 0.5 m cube size. Similar graphs for all cube sizes were nearly identical and have therefore not been included. The leaf-off scans had lower percent occlusion throughout the vertical extent of the data. However, the leaf-off occlusion increased more rapidly than the leaf-on occlusion above a height of 25 m.

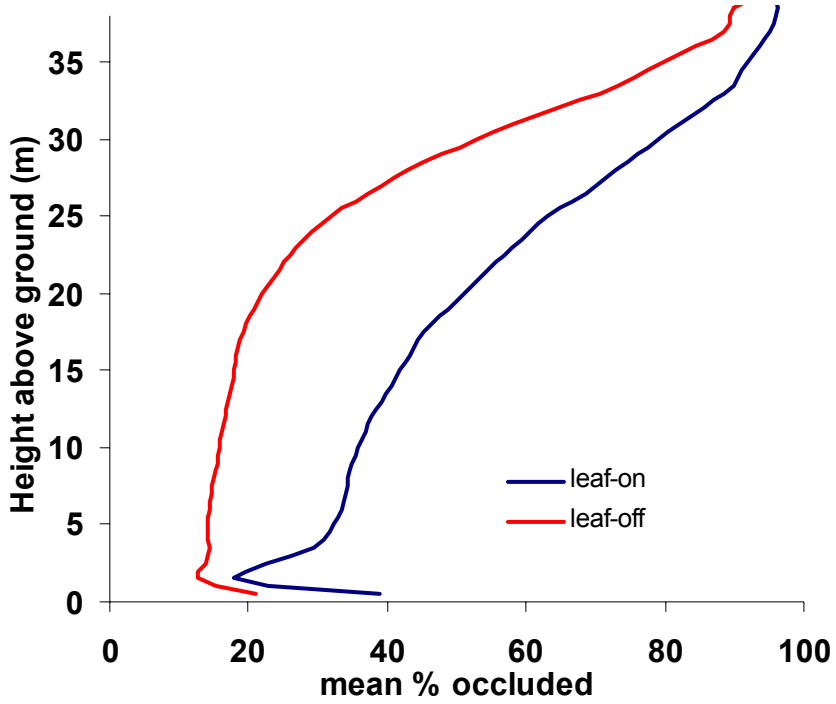

Figure 4.26. The average percent occlusion of 0.5 m cubes relative to their height above ground. The percent occlusion was averaged over all cubes at each 0.5 m height class.

The 0.25 m resolution resulted in such a high number of cubes that computer processing involving those data was difficult. Also, the relatively high percentage of cubes that were completely occluded and the relatively small number of pulses reaching cubes were deemed less than optimal. The 0.5 m cube size had fewer completely occluded cubes and many more pulses aimed at each cube. This resolution also created a data set size that could be processed using existing software with minimal limitation due to available computing power.

4.7 Plant area index estimates

Figure 4.27 contains images of the marginal horizontal distribution of plant area index (PAI) from the leaf-on and leaf-off data using the 0.5 m cube size. Estimates of PAI were obtained for 3200 marginal cells by summing the PAI estimated for each cube in a vertical column. Averaging across the 3200 cells in Figure 4.27 resulted in a plot-level average PAI estimate of 3.6 m^2/m^2 from the leaf-on data and 2.1 m^2/m^2 from the leaf-off data. For the 0.25 m cell size the plot-level average PAI estimate was 3.5 m^2/m^2 form leaf-on data and 2.2 m^2/m^2 for leaf-off data. For the 1 m cell size the plot-level average PAI estimate was 3.7 m^2/m^2 for leaf-on

data and 2.1 m^2/m^2 for leaf-off data. The lack of complete correspondence between tree locations and the distribution of PAI was due in part to leaning trees which would have concentrations of PAI not directly over the stem center at breast height.

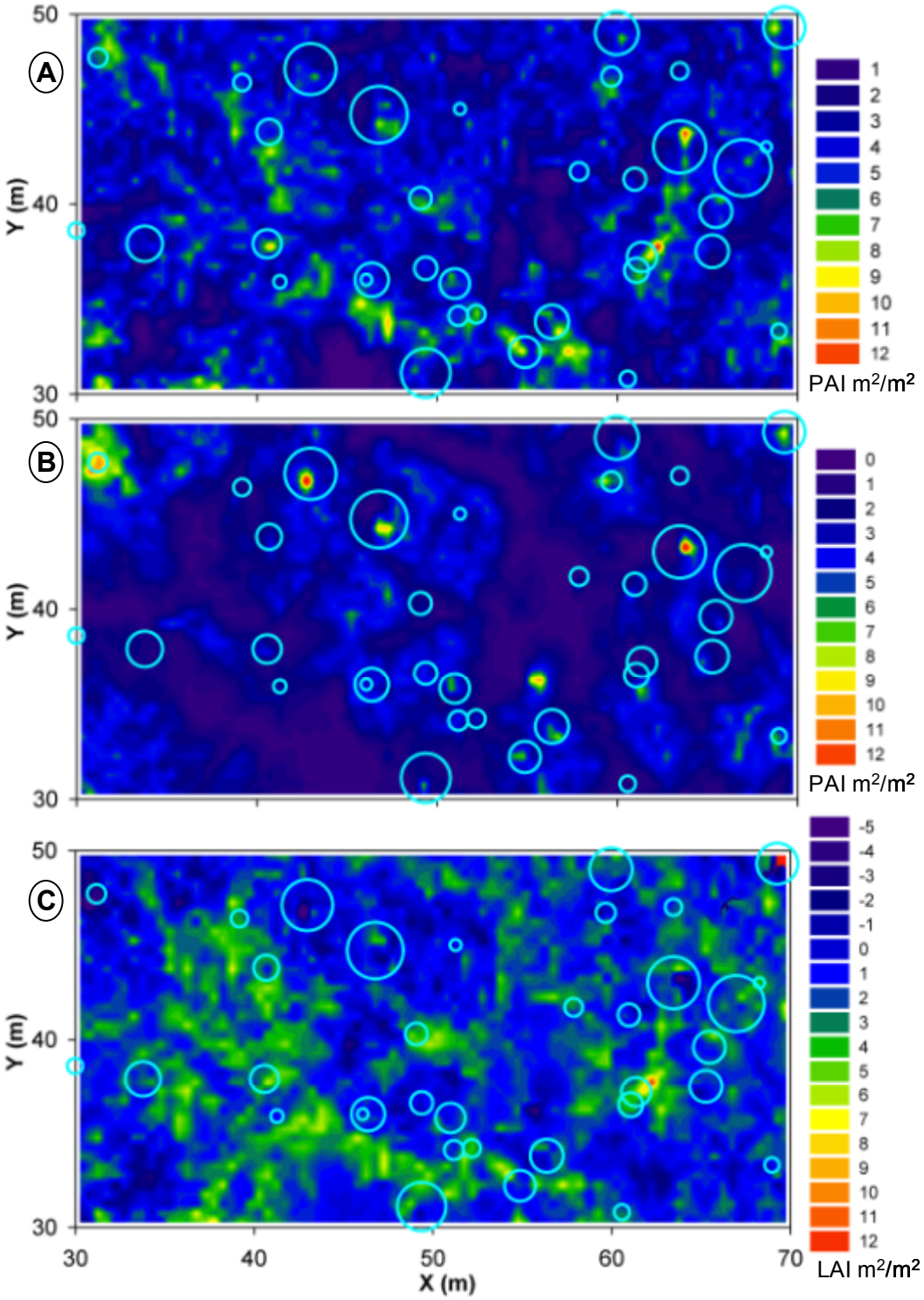

Figure 4.27. Horizontal PAI distributions from leaf-on (A) and leaf-off (B) reclassified data at the 0.5 m cube size. An approximate LAI distribution (C) was created by subtracting (B) from (A). Circles represent the locations of all trees greater than 10 cm in dbh from the 2002 Coweeta tree survey data, and are proportional to tree diameter.

If the leaf-on and leaf-off data had been registered to one another it would have been possible to obtain LAI estimates for individual cubes by subtracting the leaf-off PAI from the leaf-on PAI. However, the registration was not accurate enough to do this for individual cubes. LAI estimation was performed for columns by subtracting of Figure 4.27B from Figure 4.27A resulting in the LAI distribution in Figure 4.27C. There are obvious errors in Figure 4.27C where a number of negative values were obtained for LAI. The average LAI estimated for the plot was 1.4 m^2/m^2. Bolstad et al. (2001) reported average LAI values of 5.8 m^2/m^2 for 16 sites across the Coweeta Hydrologic Laboratory. Their LAI estimates were obtained using five leaf litter traps at each site and ranged from 2.7 m^2/m^2 to 8.2 m^2/m^2 across the sites (Bolstad et al. 2001).

To evaluate the agreement between horizontal PAI distribution and tree positions PAI estimates were obtained for each XY tree location by averaging the PAI values for the nearest 100 0.5 m × 0.5 m cells in Figure 4.27 to that trees XY location. The 100 0.5 m × 0.5 m cells represent an area of 25 m^2 or an approximate minimum projected crown area for trees greater than 10 cm in diameter. Martin et al. (1998) created allometric equations relating tree foliage area (m^2) and stem surface area (m^2) to the $\log_{10}$ of dbh in cm. Martin et al. (1998) observed R^2 values of 0.822 and 0.960 for these relationships using 86 trees of various species. Their individual tree leaf-area estimates were comparable to the leaf-on and leaf-off PAI estimates, although the PAI estimates are expressed relative to ground area. No relationship was observed between PAI and dbh for all the trees on the plot (Figure 4.28B). However, when trees between 10 cm and 20 cm in dbh were examined independently the relationship in Figure 4.28A was observed. The relationship for smaller trees may indicates that the 25 m^2 area was appropriate for smaller trees but not larger trees.

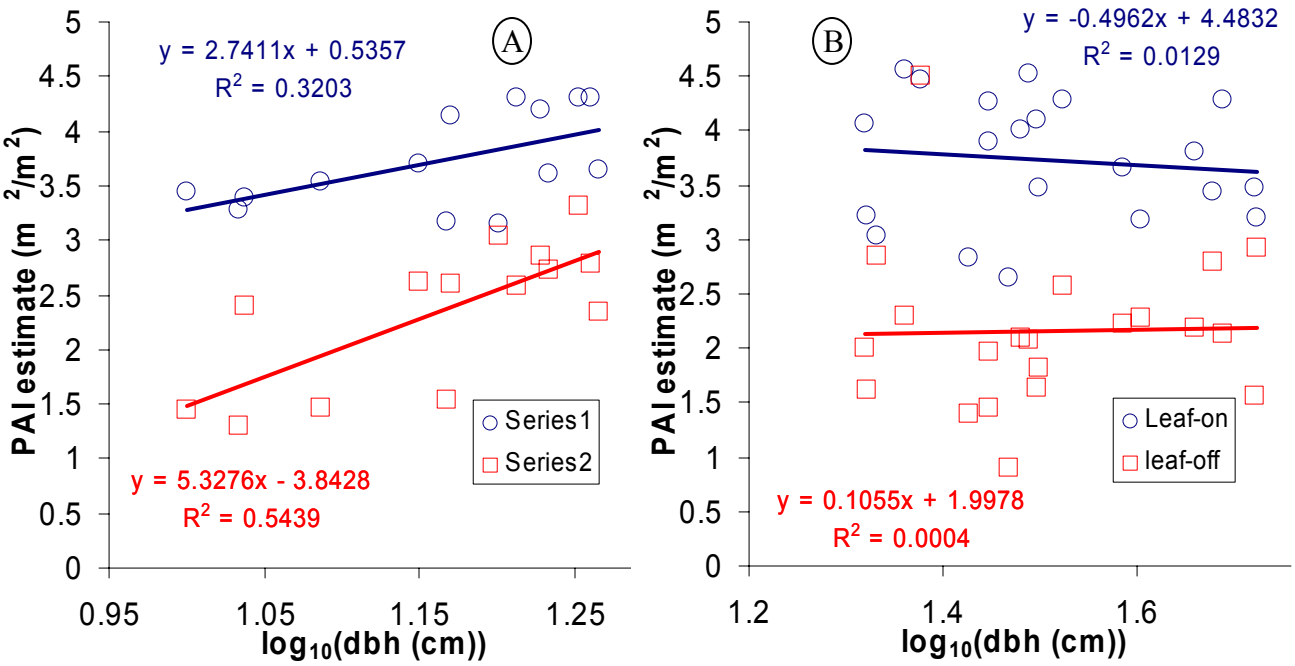

Figure 4.28. Relationships between $\log_{10}$ of dbh and PAI estimates for the 14 trees between 10 cm and 20 cm in dbh on the interior plot (A) and the 21 trees with dbh greater than 20 cm (B). Lines fit to the data using ordinary least squares regression and associated R^2 values are also included.

Weighted averages of PAI across cubes at a given height were used to estimate vertical PAI distributions. Figure 4.29 depicts vertical PAI distributions for the interior plot. The majority of the PAI was concentrated near the upper limits of the canopy with the height of maximum PAI being 33 m and 34.5 m for the leaf on and leaf-off data, respectively.

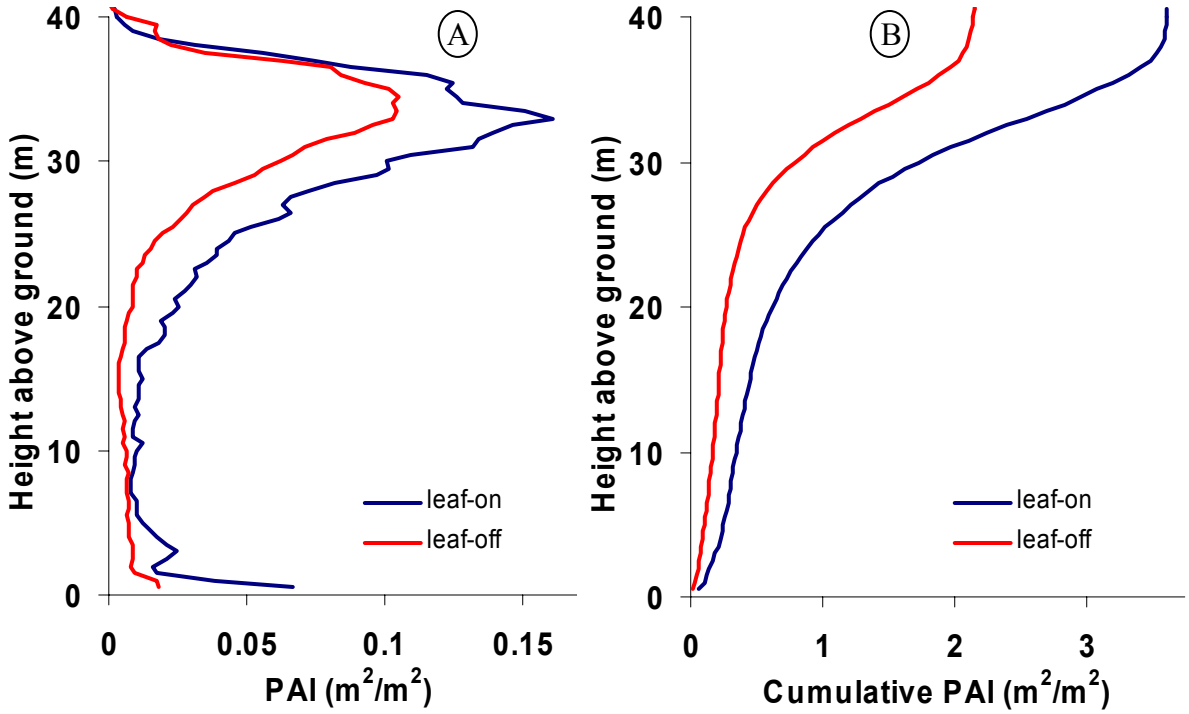

Figure 4.29. The vertical (A) and cumulative vertical distributions (B) of PAI, using 0.5 m cube size reclassified point clouds for leaf-off and leaf-on data.

4.8 Stem maps

The creation of stem maps from the registered scanner data had a number of applications. The stem maps were useful for examining the XY positions of trees in the scanner data relative to their XY location as measured in Coweeta tree survey data. The stem maps were also useful for establishing tree locations within the point cloud.

4.8.1 Stem maps for registration evaluation

Initial stem maps were made from all the EBSs paired for both within and between node registrations. As a result EBSs from multiple scan and node-level point clouds corresponded to the same trees from the survey data. Figure 4.30 contains the stem map made using these bole sections and includes the corresponding tree's locations from the survey data. Only trees that matched those extracted during registration are represented in the stem map. Tree position and diameter estimates correspond to the stem center value with the highest n_i within 1 m in the

vertical direction of breast height (1.37 m) above the DTM. If no points were within 1 m of breast height, the lowest center point in the Z-direction, above breast height, was used.

The least accurate diameters corresponded to the smallest trees, which were represented by proportionally fewer points in the scanner data. The average distance between a survey data tree XY location and a scanner estimated tree XY location was 0.51 m with a standard deviation of 0.37 m and a maximum difference of 2.0 m. The root mean squared error of the diameter estimates was 0.25 m and was inflated due to extreme over estimation of the diameters of small trees.

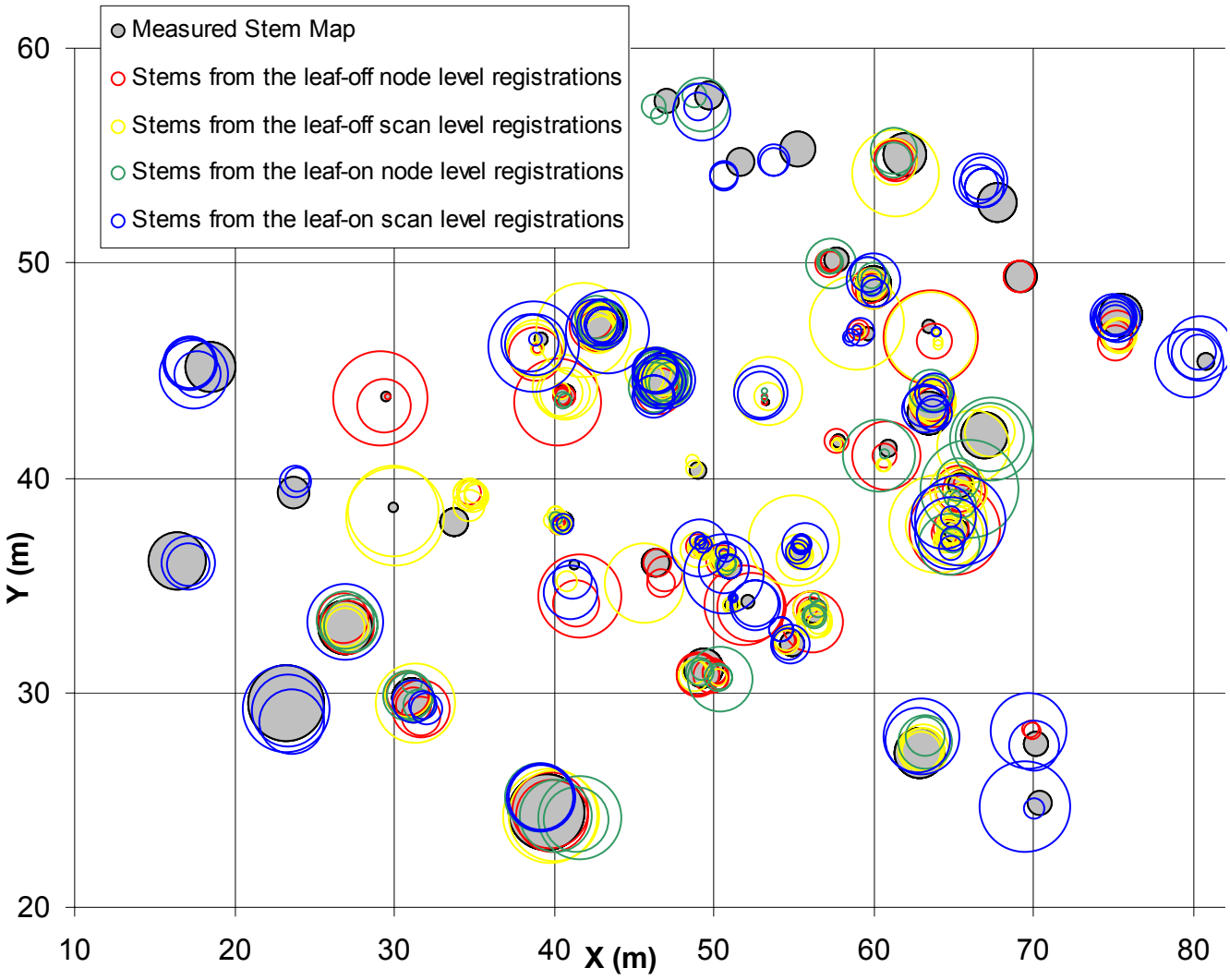

Figure 4.30. Stem map created using tree XY positions and dbh from estimated breast height centers of extracted bole sections used in ICP registrations. “Measured stem map” tree XY positions and dbh correspond to those recorded in the 2002 Coweeta tree survey data. The width of the circles is proportional to the estimated or measured dbh.

Table 4.16 contains summaries of the stem map (Figure 4.30) by scan conditions (i.e. leaf-on or leaf-off) and whether the EBS was from a single scan point cloud or a node-level point cloud. The estimated XY positions of EBSs were closer to the tree survey data for the leaf-off data than for the leaf-on data. Estimates of dbh were most accurate for bole sections from the leaf-on scans used for the node-level registrations. The use of larger trees corresponded to improved dbh estimates but did not significantly improve errors in stem position.

Table 4.16. Summary of the differences between the tree XY positions and dbh measured on the field plot and those estimated from the scanner data.

Conditions	Point cloud type	Number of Bole Sections	Mean distance error (m)	Standard deviation of distance errors (m)	Measured-estimated dbh (m)	Root mean squared dbh error (m)	Average measured dbh (m)
leaf-off	node	106	0.47	0.338	-0.066	0.235	0.34
leaf-off	scan	166	0.46	0.373	-0.099	0.274	0.31
leaf-on	node	68	0.53	0.376	-0.026	0.169	0.43
leaf-on	scan	119	0.59	0.375	-0.121	0.267	0.35
For all stem estimates		459	0.51	0.369	-0.065	0.221	0.37

The accuracy of the dbh estimates increased with the dbh of the tree being measured. This fact was confirmed by examining Figure 4.31 where the largest errors in dbh estimates were associated with the smallest trees. The magnitude of the errors did not appear to change depending on scan conditions and whether single scan or node-level point clouds were used.

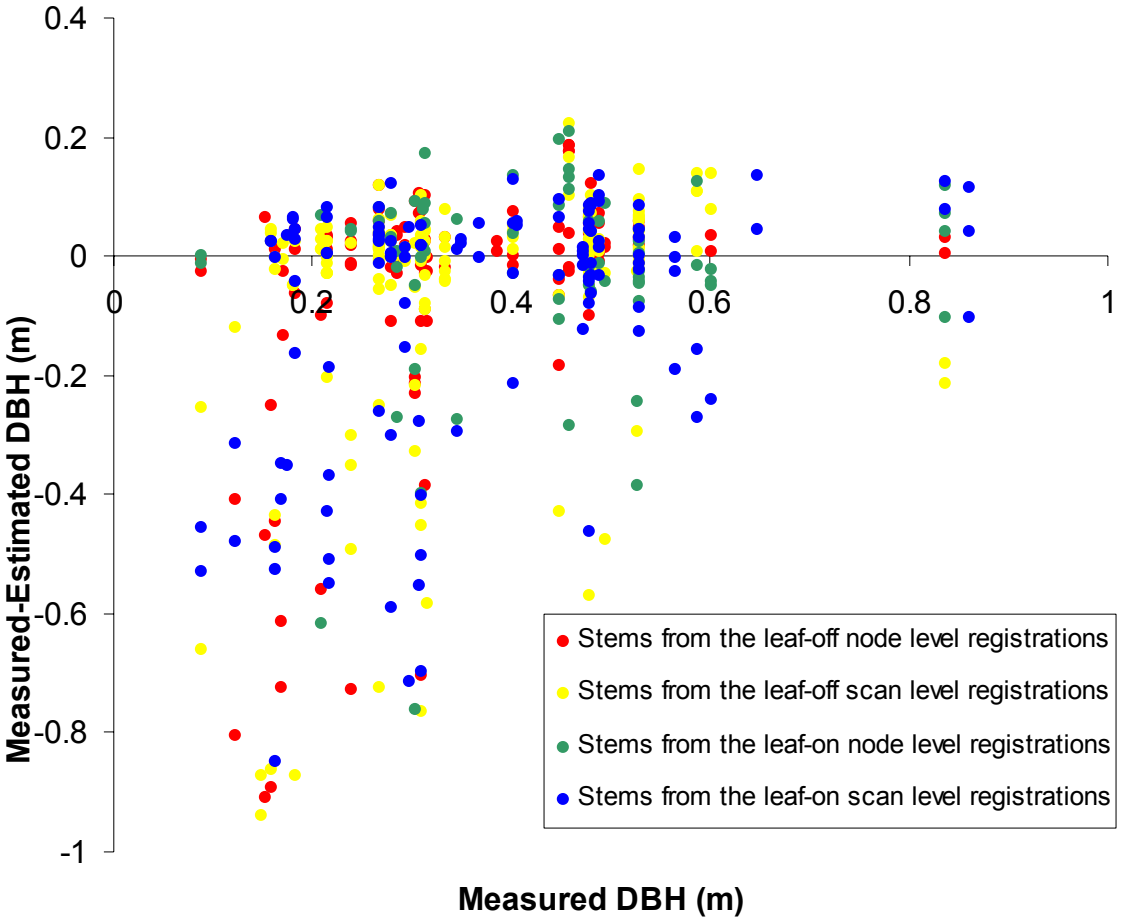

Figure 4.31. Errors in dbh estimation, calculated as the dbh from the 2002 tree survey minus dbh estimated from EBS centers. Error values are colorcoded by the time of scan acquisition (leaf-on or leaf-off) and whether the EBS was from a node-level or single scan point cloud.

Figure 4.32 includes a plot of the errors in dbh estimates relative to measured dbh values. From Figure 4.32 it was apparent that errors in dbhr estimates were unrelated to errors in tree positions. Also the errors in tree positions appear unrelated to when the scan was captured (leaf-on or leaf-off) or whether the bole sections were extracted from scan- or node-level point clouds.

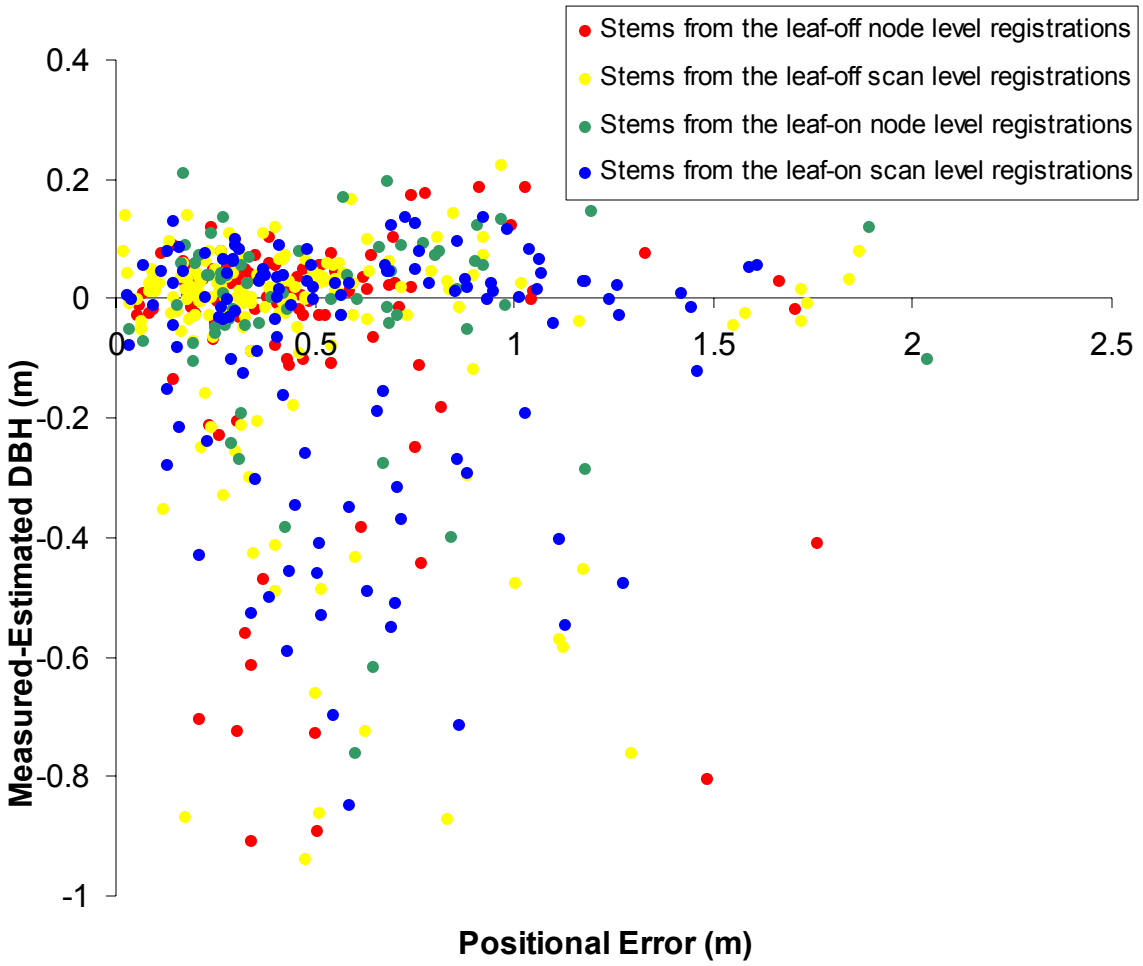

Figure 4.32. Positional errors calculated as the horizontal distance between tree XY positions from the tree survey data and EBS centers. Error values are colorcoded by the time of scan acquisition (leaf-on or leaf-off) and whether the EBS was from a node-level or single scan point cloud.

4.8.2 Final stem maps

To create the best leaf-on and leaf-off stem maps the XY-locations of centers representing the same tree in the survey data Figure 4.30 were averaged and the final diameter estimates were selected for each stem using the center with the highest n_i. This step combined the multiple estimates of tree locations and diameters from multiple scans and node-level point clouds into a single "best" estimate. The resulting stem maps for EBSs from leaf-off and leaf-on scans are presented in Figure 4.33 and Figure 4.34. Only relatively small stems and stems that were located in close proximity to other stems were not extracted and/or used in registration.

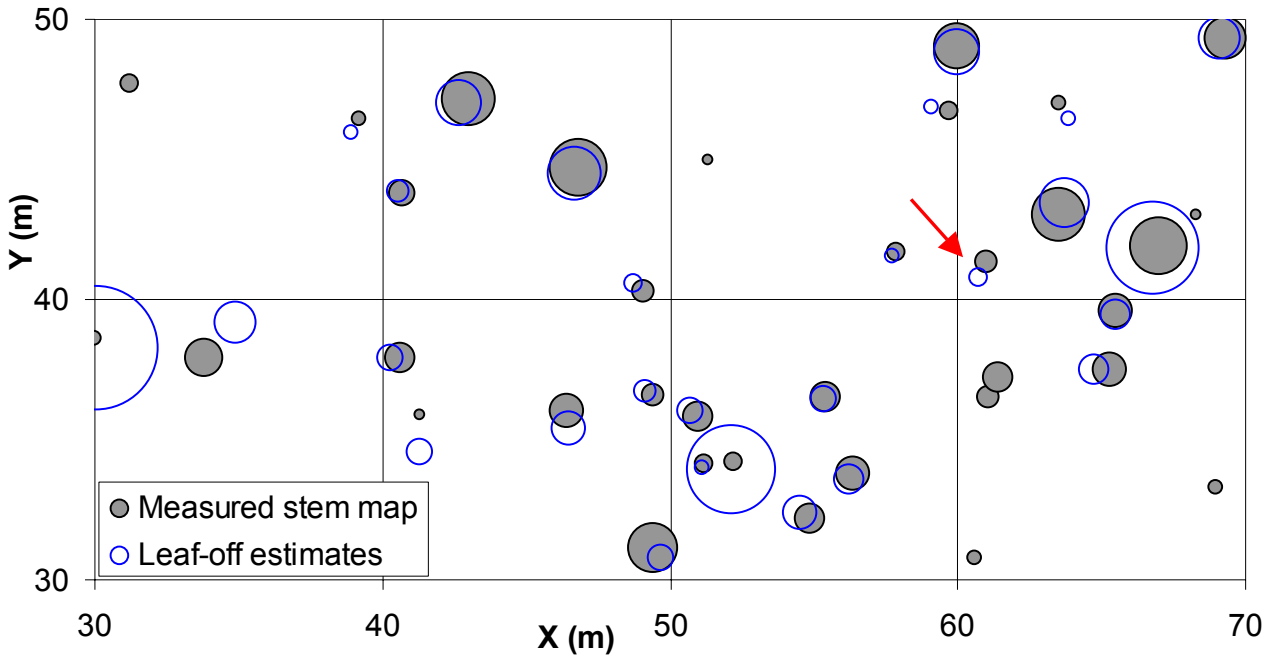

Figure 4.33. Stem map for the interior field plot, created from center estimates for EBSs used in registration of the *leaf-off* scanner data. From the EBSs 28 trees were located. All 35 trees from the survey data with a dbh greater than 10cm are shown.

More stems were included in the leaf-off stem map Figure 4.33. It was notable that in many cases errors in stem position are similar in both the leaf-on and leaf-off maps. See for example, the relative EBS and "measured" tree XY positions indicated by the red arrows in Figure 4.33 and Figure 4.34. This similarity in position error was true for many stem estimates depicted in both the leaf-off and leaf-on stem maps. The leaf-off and leaf-on data were registered

independently so the similarities in their errors suggest systematic errors in the registrations or inaccuracies in the measured stem maps.

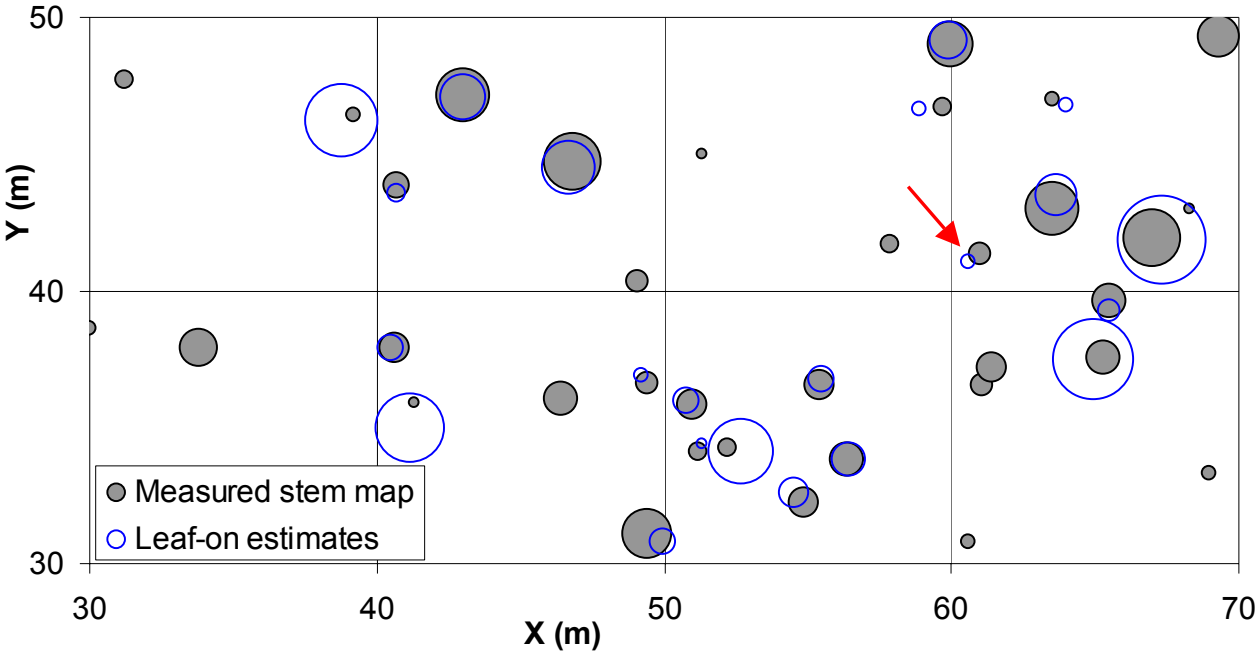

Figure 4.34. Stem map for the interior field plot, created from center estimates for EBSs used in registration of the *leaf-on* scanner data. From the EBSs 22 trees were located. All 35 trees from the survey data with a dbh greater than 10cm are shown.

The positional errors of these stem maps were relatively small, averaging less than 0.5 m as indicated in summary Table 4.17. The stem maps created from the leaf-on and leaf-off scanner data agreed more in both diameter estimates and stem positions with each other than they did with the measured stem map.

Table 4.17. Summary of differences betweens leaf-off stem map and the measured stem map; leaf-on stem map and the measured stem map; and the leaf-off and leaf-on stem maps.

Time of scan acquisition	Number of stems	Mean distance error (m)	Standard deviation of distance errors (m)	mean bias in dbh (m)	Root mean squared dbh error (m)
leaf-off	28	0.43	0.348	-0.048	0.226
leaf-on	22	0.39	0.231	-0.047	0.204
leaf-off/leaf-on comparison	22	0.29	0.125	0.030	0.169

5 Discussion and conclusions

Understanding the fundamental relationships between forest canopy structure, the light environment and tree growth requires detailed assessment of forest canopy structure (Canham et al. 2004, MacFarlane et al 2001). Ground-based laser scanning is a tool whose utility for measuring the distribution of canopy structure has only recently been examined (Lovell et al. 2003, Tanaka et al. 2004). In order to further the use of ground-based laser scanning for forest measurement applications, registration algorithms, and data summary methods like those developed here are necessary. The validity and usability of output from these methods will determine, at least in part, whether terrestrial laser scanning will gain acceptance as a tool for forest measurements.

5.1 Point cloud segmentation

A key step in applying and evaluating the ground-based laser scanner data is registration. The majority of the fine scale registrations used bole section surfaces and centers as control points. An attempt at registration using user guided bole section or tree extraction and matching required a full day to complete a within node registration of three scans. To repeat this process for 45 leaf-on scans and 41 leaf-off scans for both within node and between node registrations would have been prohibitively time consuming. The task of extracting and matching bole sections between point clouds was made more efficient and repeatable with the automated bole section extraction algorithm.

Typical image segmentation applications encounter minimal amounts of nuisance data or noise by focusing the imaging device on only the scene or surface of interest (Blais and Levine 1995, DeKruger et al. 2001, Zhilkin and Alexander 2000). In range images of forested scenes it is often not practical to eliminate noise or nuisance surfaces. The bole section extraction algorithm was derived to overcome this limitation.

The bole section extraction algorithm was developed to facilitate registration and it was effective in this role. The efficiency of the algorithm in extracting surfaces actually representing boles sections and the high number of bole sections (e.g. averages of 28 from leaf-off point

clouds and 26 for leaf-on point clouds) provided adequate common surfaces to serve as control points for all of the related ICP registrations (Table 4.5 and Table 4.8).

The bole section extraction algorithm performed well enough to enable the creation of the stem maps. The stem maps were created from the set of extracted bole sections used in registration and were able to account for as many as 80% percent of the trees present on the interior field plot (Figure 4.33). Had all extracted bole sections been used this percentage would likely have been higher. Optimization of the bole section extraction algorithm to find all trees would make it more valuable for segmenting individual trees from the point clouds. Automatically segmented trees could be used to collect data such as, total tree heights, branch parameters, upper stem diameters and crown measurements, as well as tree positions and dbh (Figure 3.8, Figure 3.9 and Table 3.7).

5.2 Registration

Objective evaluation of the registration algorithm is difficult because the precise orientations and positions of the scanner are unknown. Therefore the optimal $\mathbf{A}$ and $\tilde{\mathbf{b}}$ to align point clouds from different scanner positions, to the field plot, are also unknown. However, it is reasonable to assume that if sets of points from two scans represented the exact same points in the real world, ICP registration performed using those points would be highly accurate, barring registration to local minima (Besl and McKay 1992). Under this assumption the sources of error that would be introduced in registration are due to the inability to accurately locate or match identical points in point clouds to be registered. These types of errors generally inhibit inclusive segmentation.

The coarse registration made dealing with point cloud data more intuitive and minimized the opportunities for inaccurate matching of entire bole sections between scans. The coarse registration resulted in extracted bole sections having coordinates near their actual field plot locations. This simplified the matching of bole sections by minimizing the number of bole sections that could reasonably represent the same tree (Figure 2.5). No instances of mismatched of bole sections were detected.

ICP registrations were performed using three different sets of control surfaces; bole section surfaces, bole section centers and ground surfaces. The ICP registrations using bole section surfaces provided the fewest opportunities to introduce errors due to inaccurate control surface points or inaccurate point matching (Figure 4.8 and Figure 4.9). Because the bole section surface registrations were performed for scans taken from the same vantage point, using the output of the automated extraction algorithm, inclusive segmentation was nearly always guaranteed (Figure 4.8). Also the surface points used for registration were directly from the point cloud and did not represent extrapolations or summaries of the data.

The registrations using stem centers were necessitated by the fact that different sides of bole sections were visible from different scanner locations. Using stem centers for registration introduces errors due to both the inaccurate estimation of the location of the center and the inability to directly match center points between scans (Figure 4.13 and Figure 4.15). Highly accurate center point estimates are possible, to significant heights above ground (Figure 3.6). However, there was bias in these estimates and it appeared that overestimation of diameters increased with increasing height (Figure 3.10). From the available data it was not possible to determine if errors in diameter estimates were reflected in errors in stem center positions. If this type of error existed, registrations using those estimates would result in inaccurate tilting of one point cloud relative to the other (e.g. Figure 4.16). Alignment would be more accurate near the lower, less biased, center estimates and become less accurate with increasing height above ground.

The inability to ensure inclusive segmentation when using stem centers was overcome by interpolating the centers from one scan (Figure 4.14 and Figure 4.15). This linear interpolation decreased the accuracy of registration when stem centers were not actually straight between interpolated points. Using multiple bole sections spread throughout the scanned area can minimize the effect of these errors (Figure 4.14). A larger source of registration error emerges when the bole sections used are all relatively straight and vertical. In these cases there are a number of local minima that can result in the ground level of two scans not being correctly aligned (e.g. Figure 4.15).

The effects of tilting and ground level errors are minimal in XY positions at ground height. Registrations using the matched ground surfaces were intended to minimize tilting and

inaccurate ground level matching. The ground surfaces were estimated by summarizing the point clouds. Again, errors introduced by summary methods would adversely affect the registration. The low levels of occlusion near the forest floor (Figure 4.26) suggest that the ground surface should be accurately represented as long as the filtering algorithms were effective in eliminating non-ground points. The largest causes of inaccurate ground height were trees, resulting in points representing the base of the tree being used as the ground height. However, these errors would often be present in both surfaces and would therefore have little or no negative impact on registration (Figure 4.16 and Figure 4.17). Inclusive segmentation in ground surface registrations was ensured by using cells at common XY-coordinates in both data sets. This selection of cells also meant that ground surface registration would result in little or no translation or rotation in the XY-plane and would mostly address tilting and inaccurate ground level alignment (Figure 4.17).

The registration algorithm developed performed well as evidenced by correspondence between the stem maps created from the scanner data and the Coweeta survey data (Figure 4.33 and Figure 4.34). The ability to match trees from the registered scanner data to their real world counterparts (Figure 4.33, Figure 4.34 and Table 4.17) and the correspondence between the map of PAI and the Coweeta tree survey stem map (Figure 4.27) further support the accuracy of the registration as appropriate for these applications.

5.3 Reclassification of point cloud and occlusion reduction

A significant limitation to the utility of the ground-based laser scanner is occlusion. The use of multiple registered scans from different vantage points significantly reduced occlusion. For the leaf-off data, reclassified using cubes 0.25 m on a side, 0.1 % of the 26,870 m^3 volume of cubes, or 27 m^3, was completely occluded from view (Table 4.15). Some of this occluded volume represents the internal volume of trees and much of the rest of the occlusion was horizontally and vertically dispersed throughout the canopy (Figure 4.26 and Figure 4.27). As expected, leaf-on conditions caused significant increases in occlusion (Table 4.15). Using the larger cube size, of 0.5 m, minimized the effects by increasing the sampling rate of individual cubes (Table 4.15).

The advantage of using registered scans from multiple vantage points was most significant when compared to the reclassified cube data sets where only scans from a single location were used to determine the percent occlusion in each cube (Table 4.14). Using data only from only a single vantage resulted in 8% of the 1 m cubes being fully occluded under leaf-on conditions (Table 4.14). This amount of occlusion along with the fact that occlusion increased higher in the canopy (Figure 4.26) would result in incomplete surveys of canopy surfaces.

The use of various cube sizes to reclassify the registered point cloud data relied on the assumption that for each cube the relative numbers of pass through and intercepted pulses be representative of the entire cube (Table 4.15). This assumption has reduced effect with decreasing cube size and increased sampling of each cube. For the number and resolution of scans used here the 0.5 m cube size represented a compromise between small cube size and high sampling of each cube (Table 4.15). This cube size had relatively low complete occlusion under both leaf-on and leaf-off conditions but had a relatively high sampling rate within each cube. Even if the cubes with the minimum of number pulses aimed at them were 90% occluded they would be sampled with 20 laser pulses (Table 4.15).

While the 0.5 m cube size was appropriate here, there are a number of considerations that could result in the use of different cube size. The key considerations here involved minimizing the number of completely and highly occluded cubes, maintaining a high sampling rate per cube throughout the canopy and providing data at a scale that supported the use of the scanner data to obtain useful, high resolution 3D maps intercepted canopy surfaces. The cube size used here was made possible by the number, placement and resolution of the individual scans as well as the density of occluding surfaces within the forest (Figure 2.3 and Figure 2.6). The density of occluding surfaces is highly variable within and between forested sites. This will need to be considered in designing data collection protocols to achieve summaries at desired resolutions (Lovell et al. 2003).

There are a number of considerations in reclassifying registered point clouds that were beyond the scope of this research that will be valuable to explore going forward. The amount of pulses passing through any cube is known and decreases with increasing distance from the array of scanner locations. This information will allow for the creation of variable cube size 3D canopy surface maps. The sampling rate of cubes also must be considered when there is interest lies in

within and between cube variability. Such information could be incorporated into estimates to predict interception rates for occluded cubes.

The reclassification of registered point clouds from different vantage points into cubes was a valid means to create a 3D map of intercepted surfaces that minimized the effects of occlusion. Summaries of this data can be made across any plane, region, or transect desired (e.g. Figure 4.27 and Figure 4.29). For example, the distribution of intercepted surfaces over cone shaped volumes could be used to determine where the most light is reaching the forest floor, generating maps of the distribution understory light availability. Further, the canopy surfaces in defined volumes near tree positions could be used to evaluate inter-tree light competition. Changes in canopy distribution across elevation or terrain gradients could be evaluated using virtual transects through the reclassified data. The reclassified data provide a means to address many current questions regarding the relationship between canopy distribution and forest development.

5.4 Leaf-on verses leaf-off scans

The leaf-on and leaf-off scans resulted in significantly different levels of occlusion (Table 4.15) but they also provided different information about the distribution of canopy structure (Figure 4.27 and Figure 4.29). Direct comparisons of the spatial distribution of canopy structure from leaf-on and leaf-off data were not possible because the data were never directly registered to each other. This lack of correspondence and the spatially variable distribution of canopy structure (Figure 4.27) meant that minor registration errors resulted in cubes appearing empty under leaf-off conditions and highly foliated under leaf-on conditions or vice-versa. This effect is reflected in the negative LAI values in Figure 4.27.

To evaluate differences in canopy structure and the light environment from leaf-on scans and leaf-off scans a registration of one to the other is recommended. Aligning paired individual scans from leaf-on and leaf-off nodes would be an effective means to facilitate direct comparisons. For example, this would result in an initial registration of leaf-on scan 1 from node (40, 30) to leaf-off scan 1 from node (40, 30). The registration could be accomplished using bole surfaces because the scans were obtained from a common vantage (similar to those depicted in Figure 4.8).

Performing “simultaneous” within node, between node and ground surface registrations using the combined leaf-off and leaf-on single scans would maximize the correspondence between the two data sets. This combining of the data would eliminate the need to perform within and between node registrations for both leaf-off and leaf-on data, significantly reducing the time necessary to register all the data. The increased density of the point clouds being used should make finding matched surfaces easier, especially over the leaf-on scans only, potentially making registrations more accurate (Table 4.5 and Table 4.8). The separate registration of the leaf-on and leaf-off data used here provided a valuable basis for comparison of the performance of the registration algorithm, but for explicit comparisons of the data obtained under both conditions a simultaneous registration is recommended.

5.5 Applications

Applications developed using the scanner data included estimates of individual tree positions and diameters, canopy height models and vertical and horizontal distributions of plant and leaf area index (Figure 3.7, Figure 4.34, Figure 4.24, Figure 4.27 and Figure 4.29). One of the strengths of the scanner is that it provides data that can be used in a wide variety of applications and can be archived and reexamined in light of new research questions (Watt and Donoghue 2005).

For individual tree measurements the scanner data were used for high intensity stem taper measurements as in (Figure 3.7), while also allowing for automated, spatially explicit, stem mapping and related dbh estimates (Figure 4.33 and Figure 4.34). The diameter estimates improved with higher resolution scanning (Figure 3.6). The relatively low point densities representing small trees in the Coweeta data present a challenge to accurate diameter estimation (Figure 4.33 and Figure 4.34).

The completeness and accuracy of the stem maps was limited by the performance of the bole section extraction algorithm. The algorithm was developed to extract boles that could be used in registration, resulting in extracted bole sections that did not explicitly include data at breast height. Also bole section extraction ignored trees that were, through a combination of tree size and distance from the scanner, represented by too few points to be of value in registration. The bole section extraction algorithm was not proficient at differentiating and locating two trees

in close proximity to one another. Refinement of the bole section extraction algorithm to facilitate a more complete survey of the trees and extracting a more complete extent of those trees will aid research involving individual trees using ground-based laser scanner data.

The canopy height models (CHMs, Figure 4.24and Figure 4.25) were not explicitly validated because the actual height of the canopy was not known. The results from quantifying occlusion and the comparison between leaf-on and leaf-off digital terrain models (DTMs) provide insight into the accuracy of those models (Figure 4.22). The differences between leaf-on and leaf-off DTMs were minimal, but did increase with increasing distance from plot center (Figure 4.22). The minor differences suggest that differences in occlusion had little effect on DTM creation and that the density of points representing the ground was high enough to support the 0.25 m cell size used.

This 0.25 m cell size may not have been appropriate for canopy height models, especially under the higher occlusion, leaf-on conditions. Approximately 1% of the 0.25 m cells in the reclassified leaf-on data set (Table 4.15) were fully occluded. With occlusion increasing higher in the canopy (Figure 4.26) it was likely that the top of the canopy was not sampled for all of cells in the CHM. This was likely the cause of the downward bias in mean canopy height between the leaf-off and leaf-on CHMs. The easiest way to address this limitation would be to increase the cell size of the CHMs. The cell size selected for DTMs and CHMs should reflect the sampling density of cubes from the reclassified data set near the relative heights of those models. The DTMs and CHMs were developed as bounds to the reclassified cubic cell data sets so occlusion information was not available when those models were created.

PAI and LAI distributions were developed to exploit the high-resolution 3D nature of ground-based laser scanner data and address a perceived need in current forest research. As such there were no practical methods to provide a spatially explicit validation data set for these models. The relationship between the PAI estimates and tree positions from the Coweeta tree survey support that the positional distribution of the data are valid (Figure 4.28). The PAI and LAI estimates for the entire plot are low compared to observations by Bolstad et al. (2001) at nearby sites. There may be a number of reasons for the low estimates related to the estimator used and characteristics of the laser scanner data (Lovell et al. 2003). The estimator used may be limited by low sampling intensity for cubes high in the canopy (Radtke and Bolstad 2001).

Increasing cube size with height would address this limitation. Lovell et al. (2003) also observed that range dependent adjustments may be necessary when using ground-based laser scanner data to estimate canopy parameters. A full validation of the 3D distribution of PAI and LAI would be best performed using previously validated models that employ spatially explicit canopy distributions (Brunner 1998, MacFarlane et al. 2003). The 3D distributions of PAI and/or LAI could be used to replace the simulated canopy distributions used in such models, (e.g. MacFarlane et al. 2003) with the accuracy of predictions used to assess the canopy representations.

The applications developed using the ground-based laser scanner were created either as an extension of the registration methods or as methods that exploited the high-resolution, 3D nature of the data. The range of applications developed provides support for further exploration and application of the instrument in high-resolution, non-destructive, 3D sampling of forest surfaces.

5.6 Comparison to existing technologies and methods

Currently there are relatively few examples of applications of ground-based laser scanning in forestry research (Hopkinson et al. 2004, Lovell et al. 2003, Thies et al. 2004, Watt and Donoghue 2005). However, the data and summary methods are comparable to airborne remote sensing technologies such as scanning lidar (Lefsky et al 2001, Lovell et al. 2003). Independent applications developed to quantify 3D canopy structure and the resulting light environment also provide a valuable basis for comparison to the applications developed here.

The airborne technologies most similar to the "direct" surface measurements obtained with a ground-based scanner are scanning lidar instruments such as SLICER and LVIS (Lefsky et al. 2001 and Drake et al. 2002). These devices scan at an angle perpendicular to the line flight and gather waveform information that allows for multiple returns to be detected for each emitted laser pulse. These devices have been used to model canopy heights, tree positions, and create allometric relationships between pulse returns and parameters of interest such as plot basal area and forest biomass (Drake et al. 2002, Lefsky et al. 2001, Nelson et al. 1988a, Popescu et al. 2002).

The most significant differences between the ground-based laser scanner and the airborne device are the scale and resolution of data obtained. Maximum resolutions encountered for scanning LIDAR data were an average of 1.5 m between points from a single scan (Popescu et al. 2002). The average distance between points 40 m from the ground-based scanner was 0.11 m at 0.18° angular resolution. Airborne data are typically obtained on large-plot and landscape scales while practical applications of the ground-based scanner have not been explored for plots much larger than the 20 m × 40 m size used here (Hopkinson et al. 2004). The differing resolution and scales of airborne and ground-based devices are complimentary and will support future research in using the instruments in combination to gather data across a range of resolutions and scales (Lovell et al. 2003).

The costs of collecting airborne and ground-based data are not directly comparable. Ground-based data require a large one-time investment with relatively low cost and expertise necessary to deploy the device in the field. Airborne devices are typically not purchased for forest research, but outside contractors are paid to capture and process the data as needed. Typically the firm collecting data handles the tasks of summarizing and registering or geo-referencing the airborne data. The cost of using ground-based instruments decreases with increased use relative to the airborne instruments.

The ground-based data used here required the development of unique registration and segmentation algorithms. The algorithms are comparable to those developed for applications of high-resolution imagery in medical, engineering and surveying applications (Besl and McKay 1992, Blais and Levine 1995, Zhilkin, and Alexander 2000). Typically those applications are focused on segmentation and registrations of target objects that are known or precisely defined. Commercial software products that facilitate image registrations (e.g. Polyworks software suite, InnovMetrics Software Inc., Sainte-Foy, Que.) typically rely on user-guided selection of common points or surfaces in images being registered. The variability of forests and trees, as well as the amount of occlusion by nuisance surfaces, required greater flexibility of the registration and segmentation algorithms. This greater flexibility was at the expense of precision and accuracy in registration.

Another limitation of the registration algorithm developed here is that it was both pair-wise and stepwise. Simultaneous registration of an entire set of scans is often used to minimize

propagating errors and spread errors in registration evenly across the scene (Eggert el al. 1998, Huber and Hebert 2003, Jokinen et al. 1998). However, these simultaneous registrations are often performed for a small number of scans (3-5) and current computing power may limit their applicability for greater numbers of scans. Existing registration methods also typically employ the actual surfaces being registered, or abstractions of those surfaces that provide additional information about the nature of those surfaces (Hoover et al. 1998). The need for inclusive segmentation using scans of natural forested scenes resulted in the use of stem centers and ground surfaces, which significantly reduced the initial surface data (Figure 4.13 and Table 4.9). While increased registration accuracy should be explored in future research the level of accuracy in the registration algorithm derived here was adequate for the intended applications.

Existing methods to characterize canopy structure and distribution range from instantaneous measures using hand held optical sensors to labor-intensive destructive leaf clipping (Parent and Messier 1996, Ford and Newbould 1971). Quantum sensors and hemispherical photography can provide a one-time measure of the canopy and/or its relationship to the light environment that is only minimally spatially explicit (Comeau et al. 1998, Wang et al. 2000). The laser scanners 3D canopy survey resulted in minimal occlusion and provided completely spatially explicit 3D estimates. The laser scanner is non-destructive and more efficient and practical than destructive leaf clipping methods. Clipping methods can require the erection of towers to facilitate access throughout the canopy (Ford and Newbould 1971). Clipping methods do allow for distinctions to be made between foliage and wood surfaces. That issue has yet to be directly addressed using the ground-based laser scanner.

Radtke and Bolstad (2001) and Parker et al. (2004) have developed methods to used non-scanning ground-based lidar devices to measure canopy structure distributions by manually moving upward-directed ranging devices. These applications are limited by the ability to control the movement of the device. Both Parker et al. (2004) and Radtke and Bolstad (2001) noted that the divergence and shape of the emitted beam, as well as thresholds used to determine returned pulses impact measurements.

The MacArthur and Horn (1969) type plant area index (PAI) estimates have a number of limitations as described in previous publications (Chen and Cihlar 1995, Larsen and Kershaw 1996). The chief limitations are assumed random foliage distribution within and between

volumes being estimated, assumed random leaf angles and the need for very large samples to estimate high PAI (Radtke and Bolstad 2001). For the reclassified cubic cell data the assumptions regarding random foliage distribution are limited in their impact because the cube size used in the estimates is relatively small. The need for large samples to estimate high PAI values is also minimized by the size of cubes resulting in few or no single cubes having extremely high estimates of PAI.

The majority of the existing applications of ground-based scanning lasers in forest research focus on measuring individual tree parameters and rely on manual extraction of tree surface points (Hopkinson et al. 2004, Thies et al. 2004, Watt and Donoghue 2005). Hopkinson (et al. 2004) used 5 scans on 35 m × 35 m plots, while other researchers used fewer scans of more limited areas. In work by Hopkinson et al. (2004), Thies et al. (2004), and Watt and Donoghue (2005) registrations, if necessary, were performed using commercial software or outside firms and artificial targets placed within the scanned scenes. Tanaka et al. (2004) and Lovell et al. (2003) were the only applications that focused ground-based scanning efforts on characterizing the canopy and both only used single, unregistered scans.

Stem position and tree diameter measurements were made by Thies et al. (2004), Watt and Donoghue (2005), and Hopkinson et al. (2003). All required manual extraction and inspection of trees from the point clouds. As Thies et al. (2004) point out the value of ground-based laser scanners for individual tree measurements "depends heavily on the level of automatism that can be attained by the software-aided analysis on the scanned plots." Automating of registrations and segmentation processes will also be key to exploiting the data in obtaining more objective and less user dependent, measurements than currently possible (Thies et al. 2004). The bole section extraction algorithm and center estimation procedures presented here represent significant advances in the level of automation possible.

None of the existing applications of ground-based laser scanning made explicit attempts to minimize or quantify occlusion. To make full use of the 3D nature of ground-based laser scanner data evaluations of occlusion are necessary.

5.7 Summary

In order for the costs and time involved in gathering data with a ground-based laser scanner to be justified the data collected should provide information not available using less expensive methods. However, the methods necessary to summarize and apply ground-based laser scanner data in forest research are currently limited. Efforts were made to develop the basic tools necessary to manage and summarize ground-based laser scanner data and create applications that explored its possible end uses.

The results presented here support Hypothesis 1: Tripod mounted laser scanners provide a practical means to make useful measurements of forest features. This hypothesis is supported by the accuracy of individual tree measurements, plot level stem maps with diameter estimates, and the ability to manually and automatically extract trees and bole sections from point cloud data (Figure 3.6, Figure 3.7, Table 3.6, Figure 4.33, Figure 4.34 and Table 4.17). While most of these measurements can be collected using existing methods the fact that they can all be obtained with one measurement device, along with the potential that many other measurements could be made with that device, provide support for continued research into ground-based laser scanning as a tool for assessing forest canopy structure. The results further show that the level of accuracy of these measurements can meet or exceed that of existing methods used to gather these same data.

Hypothesis 2—Registration of laser scanner data obtained from multiple vantage points will minimize the effects of occlusion and provide a complete assessment of the 3D distribution surfaces within the forest—was supported by the minimal occlusion seen in the reclassified point cloud data set. The accuracy of the registration was adequate as evidenced by the accuracy of diameters estimated from registered data (Figure 3.6 and Table 3.5) and the accuracy of stem maps created from the registered data relative to the Coweeta field plot stem map (Table 4.17, Figure 4.33 and Figure 4.34). Point cloud registration was necessary to combine multiple scans and minimize occlusion, especially high in the canopy. The registration algorithm developed here filled this need without requiring special targets within the scan.

A major limitation to the presented research was the need to invest significant time developing methods to register the data. However, once the data were registered the

summarization algorithms and methods for obtaining individual tree measurements and 3D surface interception distributions were accurate, repeatable and efficient.

Hypothesis 3 was—Data gathered with a laser scanner will further current understanding of the relationships between 3D canopy distribution and forest development by providing data not available with current methods (i.e. gap fraction, quantum sensor measurements and simulation-based light-interception models). This hypothesis addressed the ability of the scanner to provide a novel type of data with the potential to address perceived research needs. The high-resolution plot-level terrain models, canopy top surface models, canopy height models, reclassified surface density maps and the spatially explicit PAI and LAI distributions are all examples of this type of data. The PAI and LAI distributions (Figure 4.27 and Figure 4.29) were obtained in a practical non-destructive manner at higher resolutions than currently possible without using simulated data. The reclassification of point clouds required minimal processing once the data were registered. Further, the reclassified data can be manipulated to address many current research questions or used to parameterize and validate spatially explicit models that rely on detailed simulations of canopy elements (Brunner 1998, MacFarlane et al. 2003).

This study was an exploration of the application of a ground-based laser scanner, which led to the parallel development of the data and applications. There are opportunities to optimize the methods and algorithms created here to meet specific needs. The algorithms developed here are useful for registering and summarizing ground-based laser scanner data. Ground-based laser scanning can be used for individual tree measurements and forest canopy measurements. The high resolution, 3D, spatially explicit data provide a means to collect information that cannot otherwise be gathered in a practical, non-destructive way. Future research will build on the experiences and understanding gained here to determine the most appropriate applications for ground-based laser scanning. The methods developed will be further tested and optimized in the service of those applications.

Literature Cited

Beaudet, M. and C. Messier. 2002. Variation in canopy openness and light transmission following selection cutting in northern hardwood stands: an assessment based on hemispherical photographs. *Agricultural and Forest Meteorology*. 110:217-228.

Beraldin, J.A. et al., 2000. Real world modelling through high resolution digital 3D imaging of objects and structures. *ISPRS Journal of Photogrammetry and Remote Sensing*. 55:230-250.

Bergevin, R., M. Soucy, H. Gagnon and D. Laurendeau. 1996. Towards a general multi-view registration technique. *IEEE Transactions on Pattern Analysis and Machine Intelligence*. 18:540-547.

Besl, P. J. and N. D. Mckay. 1992. A Method for Registration of 3-D Shapes. *IEEE Transactions on Pattern Analysis and Machine Intelligence*. 14:239-56.

Blais, G. and M.D. Levine. 1995. Registering multiview range data to create 3D computer objects. *IEEE Transactions on Pattern Analysis and Machine Intelligence*. 17:829-824.

Bolstad, P.V., J.M. Vose and S.G. McNulty. 2001. Forest productivity, leaf area, and terrain in Southern Appalachian deciduous forests. *Forest Science*. 47:419-427.

Brunner, A. 1998. A light model for spatially explicit forest stand models. *Forest Ecology and Management*. 107:19-46.

Canham, C.D. 1988. An index for understory light levels in and around canopy gaps. *Ecology*. 69:1634-1638.

Canham C.D., J.S. Denslow, W.J. Platt, J.R. Runkle, T.A. Spies and P.S. White. 1990. Light regimes beneath closed canopies and tree-fall gaps in temperate and tropical forests. *Canadian Journal of Forest Research*. 20:620-631.

Canham, C.D., A.C. Finzi, S.W. Pacala and D.H. Burbank. 1994. Causes and consequences of resource heterogeneity in forests - interspecific variation in light transmission by canopy trees. *Canadian Journal of Forest Research*. 24:337-349.

Chazdon, R.L. and R.W. Pearcy. 1991. The importance of sunflecks for forest understory plants. *BioScience*. 41:760-766.

Chandrasekhar, S. 1960. Radiative Transfer. Dover Pulications Inc., New York, pp.393.

Chen, J.M. 1996. Optically-based methods for measuring seasonal variation of leaf area index in boreal conifer stands. *Agricultural and Forest Meteorology*. 80:135-163.

Chen, J.M., Black, T.A. and R.S. Adams. 1991. Evaluation of hemispherical photography for determining plant area index and geometry of a forest stand. *Agricultural and Forest Meteorology*. 56:129-143.

Chen, J.M. and J. Cihlar. 1995. Plant canopy gap-size analysis theory for improving optical measurements of leaf- area index. *Applied Optics*. 34:6211-6222.

Chen, J.M., J. Liu, S.G. Leblanc, R. Lacaze and J Roujean. 2003. Multi-angular optical remote sensing for assessing vegetation structure and carbon absorption. *Remote Sensing of Environment*. 84:516-525.

Chen, Y. and G. Medioni. 1992. Object modeling by registration of multiple range images. *Image and Vision Computing*. 10:145-155.

Clark, J. and S. Robson. 2004. Accuracy of measurements made with a Cyrax 2500 laser scanner against surfaces of known colour. *Survey Review*. 37:626-638.

Comeau, P.G., T.F. Braumandl and C. Xie. 1993. Effects of overtopping vegetation on light availability and growth on Engelmann spruce (*Picea engelmannii*) seedlings. *Canadian Journal of Forest Research*. 23:2044-2048.

Comeau, P.G., F. Gendron and T. Letchford. 1998. A comparison of several methods for estimating light under a paper birch mixedwood stand. *Canadian Journal of Forest Research*. 26:1843-1850.

Curless, B., 1999. From range scans to 3D models. *Computer Graphics*. 33(4):38-41.

Dai, X. 1996. Influence of light condition in canopy gaps on forest regeneration: a new gap light index and its application in a boreal forest in east-central Sweden. *Forest Ecology and Management*. 84:187-197.

de Castro, F. and N. Fetcher. 1998. Three dimensional model of the interception of light by a canopy. *Agricultural and Forest Meteorolgy*. 90:215-233.

DeKruger, D., J. Hodge, J. C. Bezdek, J. M. Keller, and P. Gader. 2001. Detecting Mobile Land Targets in Ladar Imagery With Fuzzy Algorithms. *Journal of Intelligent & Fuzzy Systems*. 10:197-213.

Drake, J.B., R.O. Dubayah, D.B. Clark, R.G. Knox, J.B. Blair, M.A. Hofton, R.L. Chazdon, J.F. Weishampel and S.D. Prince. 2002. Estimation of tropical forest structural characteristics using large-footprint lidar. *Remote Sensing of Environment*. 79:305-319.

Eggert, D.W., A.W. Fitzgibbon, and R.B. Fisher. 1998. Simultaneous Registration of Multiple Range Views for Use in Reverse Engineering of Cad Models. *Computer Vision and Image Understanding*. 69:253-72.

Fitzgibbon, A.W., D.W. Eggert, and R.B. Fisher. 1997. High Level Cad Model Acquisition From Range Images. *Computer-Aided Design*. 29:321-30.

Ford, E.D. and P.J. Newbould. 1971. The leaf canopy of a coppiced deciduous woodland: I. Development and structure. *Journal of Ecology*. 59:843–862.

Gardingen, P.R., Jackson, G.E., Hernandez-Daumas, S., Russell, G. and Sharp, L. 1999. Leaf area index estimates obtained for clumped canopies using hemispherical photography. *Agricultural and Forest Meteorology*. 94:243-257.

Gendron, F., C. Messier and P.G. Comeau. 1998. Comparison of various methods for estimating the mean growing season percent photosynthetic photon flux density in forests. *Agricultural and Forest Meteorology*. 92:55-70.

Gersonde, R., J.J. Battles and K.L. O'Hara. 2004. Characterizing the light environment in Sierra Nevada mixed-conifer forests using a spatially explicit light model. *Canadian Journal of Forest Research*. 34:1332-1342.

Hatch, R.C., D.J. Gerrard and J.C. Tappeiner II. 1975. Exposed crown surface area: a mathematical index of individual tree growth potential. *Canadian Journal of Forest Research*. 5:224-228.

Hetzel, G., B. Leibe, P. Levi, and B. Schiele. 2001. 3D object recognition from range images using local feature histograms. In *Proceedings IEEE Computer Society Conference on Computer Vision and Pattern Recognition*. Pages 394-399.

Hoffman, R. and A.H. Jain. 1987. Segmentation and classification of range images. *IEEE Transactions on Pattern Analysis and Machine Intelligence*. 9:608-620.

Holmgren, J., M. Nilsson and H. Olsson. 2003. Estimation of tree height and stem volume on plots using airborne laser scanning. *Forest Science*. 49:419–428.

Hoover, A., D. Goldgof and K.W. Bowyer. 1998. The space envelope: A representation for 3D scenes. *Computer Vision and Image Understanding*. 69:310-329.

Hopkinson, C., L. Chasmer, C. Young-Pow and P. Treitz. 2004. Assessing forest metrics with a ground-based scanning lidar. *Canadian Journal of Forest Research*. 34:573-583.

Hoppe, H., T. DeRose, T. Duchamp, J. McDonald and W. Stuetzle. 1992. Surface reconstruction from unorganized points, SIGGRAPH '92. Computer Graphics. ACM Press, pp. 71-78.

Huber, D. F. and M. Hebert. 2003. Fully Automatic Registration of Multiple 3d Data Sets. *Image and Vision Computing*. 21:637-50.

Jokinen, O. and H. Haggrén. 1998. Statistical analysis of two 3-D registration and modeling strategies. *ISPRS Journal of Photogrametry and Remote Sensing*. 53:320-341.

Kaufman, A., D. Cohen and R. Yagel. 1993. Volume Graphics. *Computer*. 26(7):51-64.

Khalifa, I., M. Moussa and M. Kamel. 2003. Range image segmentation using local approximation of scan lines with application to CAD model acquisition. *Machine Vision and Applications*. 13:263-274.

Kloeppel, B., B. Collins, N. Gardiner, P. Carithers. 2003. GPS Locations gradient plot corners. Study number 1048. *Coweeta LTER GLOBAL Data Search*. (http://cwt33.ecology.uga.edu/summaries/summary1048.html). (Feb. 16, 2005).

Korzukhin, M D., M.T. Ter-Mikaelian and R.G. Wagner. 1996. Process versus empirical models: which approach for forest ecosystem management? *Canadian Journal of Forest Research*. 26:879-887.

Larsen, D.R. and J.A. Kershaw Jr. 1996. Influence of canopy structure assumption on prediction from Beer's law. A comparison of deterministic and stochastic simulations. *Agricultural and Forest Meteorology*. 81:61-77.

Lefsky, M.A., W.B. Cohen and T.A. Spies. 2001. An evaluation of alternate remote sensing products for forest inventory, monitoring, and mapping of Douglas-fir forests in western Oregon. *Canadian Journal of Forest Research*. 31:78-87.

Lefsky, M.A., W.B. Cohen, S.A Acker, T.A. Spies, G.G. Parker nad D. Harding. 1999. Lidar remote sensing of the canopy structure and biophysical properties of Douglas-fir western hemlock forests. *Remote Sensing of Environment*. 70:339-361.

Liu, C.J., 1995. Using portable laser EDM for forest traverse surveys. *Canadian Journal of Forest Research*. 25:753-766.

Lovell, J.L., D.J.B. Jupp, D.S. Culvenor and N.C. Coops. 2003. Using airborne and ground-based ranging lidar to measure canopy structure in Australian forests. *Canadian Journal of Remote Sensing*. 29:607-622.

MacArthur, R.H. and Horn, H.S. 1969. Foliage profile by vertical measurements. *Ecology*. 5:802-804.

MacFarlane, D.W., E.J. Green, A. Brunner and R.L. Amateis. 2003. Modeling loblolly pine canopy dynamics for a light capture model. *Forest Ecology and Management*. 173:145-168.

Martin, J.G., B.D. Kloeppel, T.L. Schaefer, D.L. Kimbler and S.G. McNulty. 1998. Aboveground biomass and nitrogen allocation of ten deciduous southern Appalachian tree species. *Canadian Journal of Forest Research*. 28:1648-1659.

Montieth, J.L. and M.H. Unsworth. 1990. Principles of Environmental Physics: Second Edition. Edward Arnold, New York, 291 pp.

Mullen, L., A. Laux, B. Concannon. E.P. Zege. I.L. Katsev and A.S. Prikahch. 2004. Amplitude-modulated laser imager. *Applied Optics*. 43:3874-3892.

Næsset, E. 1997. Determination of mean tree height of forest stands using airborne laser scanner data. *ISPRS Journal of Photogrammetry and Remote Sensing*. 52:49-56.

Nelson, R.F., W. Krabill and J. Tonelli. 1988a. Estimating forest biomass and volume using airborne laser data. *Remote Sensing of Environment*. 24:247–267.

Nelson, R., R. Swift and W. Krabill. 1988b. Using airborne lasers to estimate forest canopy and stand characteristics. *Journal of Forestry*. 86:31-38.

Nicotra, A.B., R.L. Chazdon and S.V. Iriarte. 1999. Spatial heterogeneity of light and woody seedling regeneration in tropical wet forests. *Ecology*. 80:1908-1926.

Pacala, S.W., C.D. Canham, J.A. Silander and R.K. Kobe. 1994. Sapling growth as a function of resources in a north temperate forest. *Canadian Journal of Forest Research*. 24:2172-2183.

Parent, S. and C. Messier. 1996. A simple and efficient method to estimate microsite light availability under a forest canopy. *Canadian Journal of Forest Research*. 26:151-154.

Parker, G.G., M.M. Davis and S.M. Chapotin. 2002. Canopy light transmittance in Douglas-fir—western hemlock stands. *Tree Physiology*. 22:147-157.

Parker, G.G., D.J. Harding and M.L. Berger. 2004. A portable LIDAR system for rapid determination of forest canopy structure. *Journal of Applied Ecology*. 41:755-767.

Parker, G.G., M.A. Lefsky and D.J. Harding. 2001. Light transmittance in forest canopies determined using airborne laser altimetry and in-canopy quantum measurements. *Remote Sensing of Environment*. 76:298-309.

Peet, F.G., D.J. Morrison and K.W. Pellow. 1997. Using a hand-held electronic laser-based survey instrument for stem mapping. *Canadian Journal of Forest Research*. 27:2104-2108.

Popescu, S.C., R.H. Wynne and R.F. Nelson. 2002. Estimating plot-level tree heights with lidar: local filtering with a canopy-height based variable window size. *Computers and Electronics in Agriculture*. 37:71-95.

Popescu, S.C., R.H. Wynne and J.A. Scrivani. 2004. Fusion of small-footprint lidar and multispectral data to estimate plot-level volume and biomass in deciduous and pine forests in Virginia, USA. *Forest Science*. 50:551-565.

Radtke, P.J. and P.V. Bolstad. 2001. Laser point-quadrat sampling for estimating foliage-height profiles in broad-leaved forests. *Canadian Journal of Forest Research*. 31:410-418.

Skovsgaard, J.P., V.K. Johannsen and J.K. Vanclay. 1998. Accuracy and precision of two laser dendrometers. *Forestry*. 71:131-139.

Smith, N.J., J.M. Chen and T.A. Black. 1993. Effects of clumping on estimates of stand leaf area index using the LI-COR LAI-2000. *Canadian Journal of Forest Research*. 23:1940-1943.

Stadt, K.J., S.M. Landhäusser and J.D. Stewart. 1997. Comment—The effects of direct- beam light on overcast-day estimates of light availability. *Canadian Journal of Forest Research*. 27:272-274.

Sun, W., C. Bradley, Y.F. Zhang and H.T. Loh. 2001. Cloud data modelling employing a unified, non-redundant triangular mesh. *Computer-Aided Design*. 33:183-193.

Tanaka, T., H. Park and S. Hattori. 2004. Measurement of forest canopy structure by a laser plane range-finding method improvement of radiative resolution and examples of its application. *Agricultural and Forest Meteorology*. 125:129-142.

Tanaka, T., J.Yamaguchi and Y. Takeda. 1998. Measurement of forest canopy structure with a laser plane range-finding method-development of a measurement system and applications to real forests. *Agricultural and Forest Meteorology*. 91:149-160.

Thies, M., N. Pfeifer, D. Leaf-offhalder and B.G.H. Gorte. 2004. Three-dimensional reconstruction of stems for assessment of taper, sweep and lean based on laser scanning on standing trees. *Scandinavian Journal of Forest Research*. 19:571-581.

Urban, D.L., G.B. Bonan, T.M. Smith and H.H. Shughart. 1991. Spatial applications of gap models. *Forest Ecology and Management*. 42:96-110.

van Gardingen, P.R., G.E. Jackson, S. Hernandez-Daumas, G. Russell, and L. Sharp. 1999. Leaf area index estimates obtained for clumped canopies using hemispherical photography. *Agricultural and Forest Meteorology*. 94:243-257.

Vose, J.M., N.H. Sullivan, B.D. Clinton and P.V. Bolstad. 1995. Vertical leaf area distribution, light transmittance, and application of the Beer-Lambert law in four mature hardwood stands in the southern Appalachians. *Canadian Journal of Forest Research*. 25:1036-1043.

Wang, G.G., J. Su and J.R. Wang. 2000. Height growth of planted black spruce seedling in response to interspecifc vegetation competition: a comparison of four competition measures at two measuring positions. *Canadian Journal of Forest Research*. 30:573-579.

Warren Wilson, J. 1959. Analysis of the spatial distribution of foliage by two-dimensional point quadrats. *New Phytologist*. 58:92-101.

Warren Wilson, J. 1963. Errors resulting from thickness of point quadrats. *Austrian Journal of Botany*. 11:178-188.

Warren Wilson, J. and J.E. Reeve. 1960. Inclined point quadrats. *New Phytologist*. 59:1-8.

Warren Wilson, J. and J.E. Reeve. 1963. Estimation of foliage denseness and foliage angle by inclined point quadrats. *Austrian Journal of Botany*. 11:95-105.

Watt, P.J. and M. Donoghue. 2005. Measuring forest structure with terrestrial laser scanning. *International Journal of Remote Sensing*. 26:1437-1446.

Weishampel, J.F. and D.L. Urban. 1996. Coupling a spatially-explicit forest gap model with a 3-D solar routine to simulate latitudinal effects. *Ecological Modeling*. 89:101-111.

Wing, M.G., D. Solmie and L. Kellogg. 2004. Comparing digital range finders for forestry applications. *Journal of Forestry*. 102(4):16-20.

Yoshida, T., Y. Yanagisawa and T. Kamitani. 1998. An empirical model for predicting the gap light index in an even-aged oak stand. *Forest Ecology and Management*. 109:85-89.

Zhilkin, P. and M. E. Alexander. 2000. 3d Image Registration Using a Fast Noniterative Algorithm. *Magnetic Resonance Imaging*. 18:1143-50.

Appendix

Table 1. Final registrations to align raw, *leaf-on* point clouds, from individual scans, to the Coweeta field plot coordinate system. **A** and $\tilde{\mathbf{b}}$ were calculated by algebraically combining stepwise registrations. Distances between closest points at convergence of ICP for specified steps are also included.

Node	Scan	**A**	$\tilde{\mathbf{b}}$	Distance between closest points (cm)		
				Within node	Between node	Ground
(30,30)	1	$\begin{bmatrix} -0.0198 & -0.9990 & 0.0401 \\ 0.0030 & 0.0401 & 0.9992 \\ -0.9998 & 0.0199 & 0.0022 \end{bmatrix}$	$\begin{bmatrix} 30.0556 \\ 30.3427 \\ 0.6104 \end{bmatrix}$	-		
(30,30)	2	$\begin{bmatrix} -0.0245 & -0.5526 & -0.8331 \\ 0.0002 & -0.8334 & 0.5527 \\ -0.9997 & 0.0133 & 0.0205 \end{bmatrix}$	$\begin{bmatrix} 29.9393 \\ 30.2846 \\ 0.6022 \end{bmatrix}$	3.54	5.10	13.88
(30,30)	3	$\begin{bmatrix} -0.0146 & -0.4641 & 0.8856 \\ 0.0039 & 0.8857 & 0.4642 \\ -0.9999 & 0.0102 & -0.0111 \end{bmatrix}$	$\begin{bmatrix} 30.1882 \\ 30.2853 \\ 0.6182 \end{bmatrix}$	5.89		
(30,40)	1	$\begin{bmatrix} -0.0294 & -0.9984 & 0.0481 \\ 0.0012 & 0.0481 & 0.9988 \\ -0.9996 & 0.0294 & -0.0002 \end{bmatrix}$	$\begin{bmatrix} 30.0844 \\ 40.3420 \\ 3.7171 \end{bmatrix}$	-		
(30,40)	2	$\begin{bmatrix} -0.0328 & -0.4795 & -0.8769 \\ -0.0006 & -0.8774 & 0.4798 \\ -0.9995 & 0.0163 & 0.0285 \end{bmatrix}$	$\begin{bmatrix} 29.9417 \\ 40.2659 \\ 3.7298 \end{bmatrix}$	5.67	8.26	16.91
(30,40)	3	$\begin{bmatrix} -0.0233 & -0.5116 & 0.8589 \\ -0.0026 & 0.8592 & 0.5117 \\ -0.9997 & 0.0097 & -0.0213 \end{bmatrix}$	$\begin{bmatrix} 30.2215 \\ 40.2568 \\ 3.7130 \end{bmatrix}$	4.08		
(30,50)	1	$\begin{bmatrix} -0.0559 & 0.9982 & 0.02262 \\ 0.01375 & 0.02342 & -0.9996 \\ -0.9983 & -0.0556 & -0.0150 \end{bmatrix}$	$\begin{bmatrix} 30.0157 \\ 50.4068 \\ 9.0600 \end{bmatrix}$	-		
(30,50)	2	$\begin{bmatrix} -0.0505 & 0.5179 & 0.8539 \\ 0.0169 & 0.8553 & -0.5178 \\ -0.9986 & -0.0117 & -0.0519 \end{bmatrix}$	$\begin{bmatrix} 30.1318 \\ 50.4790 \\ 9.0460 \end{bmatrix}$	3.85	13.81	26.75
(30,50)	3	$\begin{bmatrix} -0.0588 & 0.5396 & -0.8399 \\ 0.0190 & -0.8406 & -0.5414 \\ -0.9981 & -0.0478 & 0.0392 \end{bmatrix}$	$\begin{bmatrix} 29.8986 \\ 50.4699 \\ 9.0857 \end{bmatrix}$	5.50		
(40,30)	1	$\begin{bmatrix} -0.0009 & -0.9985 & 0.0542 \\ 0.0023 & 0.0542 & 0.9985 \\ -1.0000 & 0.0010 & 0.0022 \end{bmatrix}$	$\begin{bmatrix} 40.3066 \\ 30.0639 \\ -2.5175 \end{bmatrix}$	-		
(40,30)	2	$\begin{bmatrix} -0.0003 & -0.4721 & -0.8815 \\ 0.0021 & -0.8815 & 0.4721 \\ -1.0000 & -0.0017 & 0.0013 \end{bmatrix}$	$\begin{bmatrix} 40.1650 \\ 29.9922 \\ -2.5017 \end{bmatrix}$	3.78	18.16	25.19
(40,30)	3	$\begin{bmatrix} 0.0050 & -0.4741 & 0.8805 \\ -0.0018 & 0.8805 & 0.4741 \\ -1.0000 & -0.0040 & 0.0040 \end{bmatrix}$	$\begin{bmatrix} 40.4123 \\ 29.9977 \\ -2.5638 \end{bmatrix}$	6.90		

Appendix, Table 1. (*continued*)

Node	Scan	**A**	$\tilde{\mathbf{b}}$	Distance between closest points (cm)		
				Within node	Between node	Ground
(40,40)	1	$\begin{bmatrix} -0.0165 & -0.9992 & 0.0368 \\ -0.0062 & 0.0369 & 0.9993 \\ -0.9998 & 0.0163 & -0.0067 \end{bmatrix}$	$\begin{bmatrix} 40.0479 \\ 40.2412 \\ 1.5523 \end{bmatrix}$	-		
(40,40)	2	$\begin{bmatrix} -0.0257 & -0.4846 & -0.8743 \\ -0.0055 & -0.8745 & 0.4849 \\ -0.9997 & 0.0173 & 0.0198 \end{bmatrix}$	$\begin{bmatrix} 39.9114 \\ 40.1696 \\ 1.5491 \end{bmatrix}$	3.89	19.07	33.05
(40,40)	3	$\begin{bmatrix} -0.0096 & -0.4162 & 0.9092 \\ -0.0126 & 0.9092 & 0.4161 \\ -0.9999 & -0.0075 & -0.0140 \end{bmatrix}$	$\begin{bmatrix} 40.1981 \\ 40.1205 \\ 1.5512 \end{bmatrix}$	3.83		
(40,50)	1	$\begin{bmatrix} -0.0085 & -0.9952 & -0.0967 \\ 0.0197 & -0.0969 & 0.9951 \\ -0.9998 & 0.0065 & 0.0065 \end{bmatrix}$	$\begin{bmatrix} 39.5205 \\ 50.1843 \\ 6.14465 \end{bmatrix}$	-		
(40,50)	2	$\begin{bmatrix} -0.0112 & -0.5279 & -0.8492 \\ 0.0202 & -0.8492 & 0.5277 \\ -0.9997 & -0.0112 & 0.0202 \end{bmatrix}$	$\begin{bmatrix} 39.4011 \\ 50.1380 \\ 6.1407 \end{bmatrix}$	3.41	12.60	28.36
(40,50)	3	$\begin{bmatrix} -0.0044 & -0.4477 & 0.8942 \\ 0.0216 & 0.8939 & 0.4477 \\ -0.9998 & 0.0213 & 0.0058 \end{bmatrix}$	$\begin{bmatrix} 39.6495 \\ 50.1144 \\ 6.1450 \end{bmatrix}$	2.90		
(50,30)	1	$\begin{bmatrix} -0.0185 & -0.9998 & 0.0097 \\ -0.0099 & 0.0099 & 0.9999 \\ -0.9998 & 0.0183 & -0.0100 \end{bmatrix}$	$\begin{bmatrix} 49.5018 \\ 30.5922 \\ -3.3924 \end{bmatrix}$	-		
(50,30)	2	$\begin{bmatrix} -0.0177 & -0.6012 & -0.7989 \\ -0.0133 & -0.7988 & 0.6015 \\ -0.9998 & 0.0212 & 0.0063 \end{bmatrix}$	$\begin{bmatrix} 49.3973 \\ 30.5362 \\ -3.3742 \end{bmatrix}$	3.57	18.34	48.83
(50,30)	3	$\begin{bmatrix} -0.0103 & -0.5251 & 0.8510 \\ -0.0295 & 0.8508 & 0.5246 \\ -0.9995 & -0.0197 & -0.0242 \end{bmatrix}$	$\begin{bmatrix} 49.6983 \\ 30.3682 \\ -3.4220 \end{bmatrix}$	3.93		
(50,40)	1	$\begin{bmatrix} 0.0000 & -1.0000 & 0.0000 \\ 0.0000 & 0.0000 & 1.0000 \\ -1.0000 & 0.0000 & 0.0000 \end{bmatrix}$	$\begin{bmatrix} 50.0000 \\ 40.0000 \\ 0.0000 \end{bmatrix}$	-		
(50,40)	2	$\begin{bmatrix} 0.02335 & -0.4951 & -0.8685 \\ 0.0095 & -0.8686 & 0.4954 \\ -0.9997 & -0.0198 & -0.0156 \end{bmatrix}$	$\begin{bmatrix} 50.0423 \\ 39.9563 \\ 0.0294 \end{bmatrix}$	12.20	-	-
(50,40)	3	$\begin{bmatrix} 0.0030 & -0.4461 & 0.8950 \\ -0.0025 & 0.8950 & 0.4461 \\ 1.0000 & -0.0036 & 0.0016 \end{bmatrix}$	$\begin{bmatrix} 50.1340 \\ 39.9123 \\ 0.0061 \end{bmatrix}$	5.23		
(50,50)	1	$\begin{bmatrix} 0.0209 & 0.9965 & 0.0806 \\ 0.0321 & 0.0799 & -0.9963 \\ -0.9993 & 0.0234 & -0.0303 \end{bmatrix}$	$\begin{bmatrix} 49.2912 \\ 49.5568 \\ 4.1106 \end{bmatrix}$	-		
(50,50)	2	$\begin{bmatrix} 0.0249 & 0.3961 & 0.9179 \\ 0.0299 & 0.9174 & -0.3968 \\ -0.9992 & 0.0373 & 0.0110 \end{bmatrix}$	$\begin{bmatrix} 49.4976 \\ 49.5800 \\ 4.1216 \end{bmatrix}$	2.61	11.74	41.36
(50,50)	3	$\begin{bmatrix} 0.0264 & 0.5417 & -0.8401 \\ 0.0308 & -0.8405 & -0.5410 \\ -0.9992 & -0.0116 & -0.0389 \end{bmatrix}$	$\begin{bmatrix} 49.1542 \\ 49.6316 \\ 4.1148 \end{bmatrix}$	3.75		

Appendix, Table 1. (*continued*)

Node	Scan	**A**	$\tilde{\mathbf{b}}$	Distance between closest points (cm)		
				Within node	Between node	Ground
(60,30)	1	$\begin{bmatrix} 0.0131 & -0.9996 & -0.0262 \\ -0.0109 & -0.0263 & 0.9996 \\ -0.9999 & -0.0128 & -0.0120 \end{bmatrix}$	$\begin{bmatrix} 60.1766 \\ 29.8041 \\ -3.3857 \end{bmatrix}$	-		
(60,30)	2	$\begin{bmatrix} -0.0019 & -0.4721 & -0.8816 \\ -0.0269 & -0.8812 & 0.4719 \\ -0.9996 & 0.0245 & -0.0111 \end{bmatrix}$	$\begin{bmatrix} 60.3598 \\ 29.3282 \\ -3.3391 \end{bmatrix}$	3.38	10.32	16.98
(60,30)	3	$\begin{bmatrix} 0.0171 & -0.5231 & 0.8521 \\ -0.0140 & 0.8520 & 0.5232 \\ -0.9998 & -0.0209 & 0.0073 \end{bmatrix}$	$\begin{bmatrix} 60.3025 \\ 29.7262 \\ -3.3710 \end{bmatrix}$	5.10		
(60,40)	1	$\begin{bmatrix} 0.0160 & -0.9994 & -0.0316 \\ 0.0192 & -0.0313 & 0.9993 \\ -0.9997 & -0.0166 & 0.0187 \end{bmatrix}$	$\begin{bmatrix} 59.9625 \\ 40.6430 \\ -0.2192 \end{bmatrix}$	-		
(60,40)	2	$\begin{bmatrix} 0.0177 & -0.5088 & -0.8607 \\ 0.0139 & -0.8606 & 0.5091 \\ -0.9997 & -0.0210 & -0.0083 \end{bmatrix}$	$\begin{bmatrix} 59.8561 \\ 40.5761 \\ -0.2274 \end{bmatrix}$	4.27	22.47	26.19
(60,40)	3	$\begin{bmatrix} 0.01700 & -0.4895 & 0.8718 \\ 0.0123 & 0.8720 & 0.4894 \\ -0.9998 & 0.0024 & 0.0209 \end{bmatrix}$	$\begin{bmatrix} 60.0541 \\ 40.5608 \\ -0.2244 \end{bmatrix}$	4.73		
(60,50)	1	$\begin{bmatrix} 0.00428 & 1.0000 & 0.0026 \\ 0.0391 & 0.0024 & -0.9992 \\ -0.9992 & 0.0044 & -0.0390 \end{bmatrix}$	$\begin{bmatrix} 59.7294 \\ 50.0233 \\ 3.4424 \end{bmatrix}$	-		
(60,50)	2	$\begin{bmatrix} 0.0062 & 0.5591 & 0.8291 \\ 0.0449 & 0.8281 & -0.5588 \\ -0.9990 & 0.0406 & -0.0200 \end{bmatrix}$	$\begin{bmatrix} 59.8326 \\ 50.1352 \\ 3.4512 \end{bmatrix}$	5.86	6.47	27.98
(60,50)	3	$\begin{bmatrix} 0.0073 & 0.0073 & -0.8645 \\ 0.0390 & -0.8640 & -0.5020 \\ -0.9992 & -0.0301 & -0.0260 \end{bmatrix}$	$\begin{bmatrix} 59.6364 \\ 50.0848 \\ 3.4513 \end{bmatrix}$	3.93		
(70,30)	1	$\begin{bmatrix} 0.0196 & -0.9993 & -0.0333 \\ 0.0106 & -0.0331 & 0.9994 \\ -0.9998 & -0.0200 & 0.0100 \end{bmatrix}$	$\begin{bmatrix} 69.8829 \\ 30.6805 \\ -2.2019 \end{bmatrix}$	-		
(70,30)	2	$\begin{bmatrix} -0.0052 & -0.4544 & -0.8908 \\ 0.0014 & -0.8908 & 0.4544 \\ -1.0000 & 0.0011 & 0.0053 \end{bmatrix}$	$\begin{bmatrix} 69.6392 \\ 30.5519 \\ -2.2810 \end{bmatrix}$	10.99	21.58	24.27
(70,30)	3	$\begin{bmatrix} 0.0134 & -0.5266 & 0.8500 \\ 0.0149 & 0.8501 & 0.5265 \\ -0.9998 & 0.0056 & 0.0192 \end{bmatrix}$	$\begin{bmatrix} 69.9171 \\ 30.6449 \\ -2.2137 \end{bmatrix}$	6.37		
(70,40)	1	$\begin{bmatrix} 0.01799 & -0.9990 & 0.0402 \\ 0.0182 & 0.0405 & 0.9990 \\ -0.9997 & -0.0172 & 0.0189 \end{bmatrix}$	$\begin{bmatrix} 69.8564 \\ 40.7187 \\ -0.0603 \end{bmatrix}$	-		
(70,40)	2	$\begin{bmatrix} 0.0066 & -0.5143 & -0.8576 \\ 0.0135 & -0.8575 & 0.5143 \\ -0.9999 & -0.0149 & 0.0013 \end{bmatrix}$	$\begin{bmatrix} 69.7290 \\ 40.6507 \\ -0.0677 \end{bmatrix}$	3.81	10.27	38.22
(70,40)	3	$\begin{bmatrix} 0.0187 & -0.3056 & 0.9520 \\ 0.0112 & 0.9521 & 0.3054 \\ -0.9998 & 0.0049 & 0.0213 \end{bmatrix}$	$\begin{bmatrix} 70.2699 \\ 40.9983 \\ 0.104682 \end{bmatrix}$	4.21		

Appendix, Table 1. (*continued*)

Node	Scan	**A**	$\tilde{\mathbf{b}}$	Distance between closest points (cm)		
				Within node	Between node	Ground
(70,50)	1	$\begin{bmatrix} 0.0160 & 0.9999 & -0.0012 \\ 0.0327 & -0.0017 & -0.9995 \\ -0.9993 & 0.0160 & -0.0327 \end{bmatrix}$	$\begin{bmatrix} 69.8177 \\ 50.3275 \\ 4.7763 \end{bmatrix}$	-		
(70,50)	2	$\begin{bmatrix} 0.0202 & 0.4592 & 0.8881 \\ 0.0332 & 0.8875 & -0.4597 \\ -0.9992 & 0.0387 & 0.0027 \end{bmatrix}$	$\begin{bmatrix} 69.9585 \\ 50.3743 \\ 4.7796 \end{bmatrix}$	3.37	9.49	32.67
(70,50)	3	$\begin{bmatrix} 0.0055 & 0.4598 & -0.8880 \\ 0.0365 & -0.8875 & -0.4594 \\ -0.9993 & -0.0298 & -0.0216 \end{bmatrix}$	$\begin{bmatrix} 69.6863 \\ 50.4195 \\ 4.7862 \end{bmatrix}$	3.14		

Table 2. Final registrations to align raw, *leaf-off* point clouds, from individual scans, to the Coweeta field plot coordinate system. **A** and $\tilde{\mathbf{b}}$ were calculated by algebraically combining stepwise registrations. Distances between closest points at convergence of ICP for specified steps are also included.

Node	Scan	**A**	$\tilde{\mathbf{b}}$	Distance between closest points (cm)	
				Within node	Between node
(30,30)	1	$\begin{bmatrix} -0.0179 & -0.8713 & -0.4904 \\ -0.0073 & -0.4904 & 0.8715 \\ -0.9998 & 0.0192 & 0.0024 \end{bmatrix}$	$\begin{bmatrix} 30.1812 \\ 30.0499 \\ 0.2137 \end{bmatrix}$	-	16.15
(30,30)	2	$\begin{bmatrix} -0.0059 & -0.6186 & -0.7856 \\ -0.0224 & -0.7854 & 0.6186 \\ -0.9997 & 0.0213 & -0.0092 \end{bmatrix}$	$\begin{bmatrix} 29.7472 \\ 30.2949 \\ 0.3110 \end{bmatrix}$	16.61	
(30,40)	1	$\begin{bmatrix} -0.0101 & -0.9988 & -0.04707 \\ 0.0205 & -0.0473 & 0.9987 \\ -0.9997 & 0.0091 & 0.0209 \end{bmatrix}$	$\begin{bmatrix} 29.9208 \\ 40.2209 \\ 3.2554 \end{bmatrix}$	-	17.08
(30,40)	2	$\begin{bmatrix} -0.0109 & -0.5242 & -0.8515 \\ 0.0231 & -0.8515 & 0.5239 \\ -0.9997 & -0.0140 & 0.0214 \end{bmatrix}$	$\begin{bmatrix} 29.8530 \\ 40.1058 \\ 3.2499 \end{bmatrix}$	4.05	
(30,40)	3	$\begin{bmatrix} -0.0196 & -0.4528 & 0.8914 \\ -0.0005 & 0.8916 & 0.4529 \\ -0.9998 & 0.0084 & -0.0177 \end{bmatrix}$	$\begin{bmatrix} 30.1829 \\ 40.3240 \\ 3.2927 \end{bmatrix}$	5.57	
(30,50)	1	$\begin{bmatrix} 0.0089 & -0.4167 & 0.9090 \\ 0.0148 & 0.9090 & 0.4165 \\ -0.9999 & 0.0097 & 0.0142 \end{bmatrix}$	$\begin{bmatrix} 29.9930 \\ 50.3729 \\ 8.0040 \end{bmatrix}$	-	18.35
(30,50)	2	$\begin{bmatrix} -0.0029 & -0.8724 & 0.4887 \\ 0.0114 & 0.4886 & 0.8724 \\ -0.9999 & 0.0081 & 0.0085 \end{bmatrix}$	$\begin{bmatrix} 29.9324 \\ 50.3979 \\ 8.0071 \end{bmatrix}$	8.15	
(40,30)	1	$\begin{bmatrix} 0.1172 & 0.0587 & -0.9914 \\ -0.0380 & -0.9973 & -0.0635 \\ -0.9924 & 0.0451 & --0.1147 \end{bmatrix}$	$\begin{bmatrix} 40.7917 \\ 29.6717 \\ -2.8414 \end{bmatrix}$	-	38.59
(40,30)	2	$\begin{bmatrix} 0.0831 & 0.8727 & -0.4811 \\ -0.0249 & -0.4808 & -0.8765 \\ -0.9962 & 0.0848 & -0.0182 \end{bmatrix}$	$\begin{bmatrix} 40.7451 \\ 29.8109 \\ -2.8824 \end{bmatrix}$	13.96	
(40,30)	3	$\begin{bmatrix} 0.1008 & -0.8238 & -0.5579 \\ -0.0998 & -0.5663 & 0.8182 \\ -0.9899 & -0.0268 & -0.1393 \end{bmatrix}$	$\begin{bmatrix} 40.7776 \\ 29.2988 \\ -2.6012 \end{bmatrix}$	26.98	
(40,40)	1	$\begin{bmatrix} 0.0123 & 0.5093 & -0.8604 \\ -0.0102 & -0.8604 & -0.5095 \\ -0.9999 & 0.0150 & -0.0054 \end{bmatrix}$	$\begin{bmatrix} 39.6748 \\ 39.9886 \\ 1.1122 \end{bmatrix}$	-	9.48
(40,40)	2	$\begin{bmatrix} -0.0065 & 0.9998 & 0.0187 \\ -0.0003 & 0.0187 & -0.9998 \\ -1.0000 & -0.0065 & 0.0001 \end{bmatrix}$	$\begin{bmatrix} 39.7988 \\ 39.8272 \\ 1.0887 \end{bmatrix}$	7.79	
(40,40)	3	$\begin{bmatrix} -0.0020 & -0.5462 & -0.8377 \\ 0.0025 & -0.8377 & 0.5462 \\ -1.0000 & -0.0010 & 0.0030 \end{bmatrix}$	$\begin{bmatrix} 39.6131 \\ 40.2106 \\ 1.1193 \end{bmatrix}$	7.53	

Appendix, Table 2. (*continued*)

Node	Scan	**A**	$\tilde{\mathbf{b}}$	Distance between closest points (cm): Within node	Distance between closest points (cm): Between node
(40,50)	1	$\begin{bmatrix} -0.0103 & 0.0006 & 0.9999 \\ 0.0294 & 0.9996 & -0.0003 \\ -0.9995 & 0.0294 & -0.0103 \end{bmatrix}$	$\begin{bmatrix} 39.8568 \\ 50.0054 \\ 5.7961 \end{bmatrix}$	-	
(40,50)	2	$\begin{bmatrix} -0.0127 & -0.8584 & 0.5128 \\ 0.0289 & 0.5123 & 0.8583 \\ -0.9995 & 0.0257 & 0.0184 \end{bmatrix}$	$\begin{bmatrix} 39.7591 \\ 50.1340 \\ 5.7957 \end{bmatrix}$	4.92	12.47
(40,50)	3	$\begin{bmatrix} -0.0127 & 0.8775 & 0.4793 \\ 0.0300 & 0.4795 & -0.8770 \\ -0.9995 & 0.0032 & -0.0324 \end{bmatrix}$	$\begin{bmatrix} 39.7710 \\ 49.8804 \\ 5.8184 \end{bmatrix}$	4.23	
(50,30)	1	$\begin{bmatrix} 0.0114 & 0.0071 & -0.9999 \\ 0.0164 & -0.9998 & -0.0069 \\ -0.9998 & -0.0163 & -0.0115 \end{bmatrix}$	$\begin{bmatrix} 49.8870 \\ 30.1375 \\ -3.9980 \end{bmatrix}$	-	
(50,30)	2	$\begin{bmatrix} 0.0105 & 0.8616 & -0.5075 \\ 0.0121 & -0.5076 & -0.8615 \\ -0.9999 & 0.0029 & -0.0158 \end{bmatrix}$	$\begin{bmatrix} 49.9461 \\ 29.9677 \\ -4.0009 \end{bmatrix}$	1.56	15.93
(50,30)	3	$\begin{bmatrix} 0.0219 & -0.8379 & -0.5453 \\ 0.0026 & -0.5454 & 0.8382 \\ -0.9998 & -0.0198 & -0.0097 \end{bmatrix}$	$\begin{bmatrix} 50.0608 \\ 30.1101 \\ -3.9996 \end{bmatrix}$	5.07	
(50,40)	1	$\begin{bmatrix} 0.0000 & -0.6342 & 0.7732 \\ 0.0000 & 0.7732 & 0.6342 \\ -1.0000 & 0.0000 & 0.0000 \end{bmatrix}$	$\begin{bmatrix} 50.0000 \\ 40.0000 \\ 0.0000 \end{bmatrix}$	-	
(50,40)	2	$\begin{bmatrix} -0.0065 & -0.9995 & -0.0294 \\ 0.0102 & -0.0295 & 0.9995 \\ -0.9999 & 0.0062 & 0.0104 \end{bmatrix}$	$\begin{bmatrix} 49.8426 \\ 40.1545 \\ 0.0418 \end{bmatrix}$	6.35	-
(50,40)	3	$\begin{bmatrix} -0.0054 & 0.5228 & 0.8525 \\ -0.0052 & 0.8525 & -0.5228 \\ -1.0000 & -0.0072 & -0.0018 \end{bmatrix}$	$\begin{bmatrix} 49.9724 \\ 39.8747 \\ 0.0243 \end{bmatrix}$	6.58	
(50,50)	1	$\begin{bmatrix} -0.0006 & 0.0050 & 1.0000 \\ 0.02169 & 0.9998 & -0.0049 \\ -0.9998 & 0.0217 & -0.0007 \end{bmatrix}$	$\begin{bmatrix} 49.9504 \\ 49.9826 \\ 3.3800 \end{bmatrix}$	-	
(50,50)	2	$\begin{bmatrix} 0.0020 & -0.8459 & 0.5334 \\ 0.0202 & 0.5333 & 0.8457 \\ -0.9998 & 0.0091 & 0.0181 \end{bmatrix}$	$\begin{bmatrix} 49.9244 \\ 50.0679 \\ 3.3437 \end{bmatrix}$	6.34	8.38
(50,50)	3	$\begin{bmatrix} -0.0002 & 0.8492 & 0.5282 \\ 0.0220 & 0.5280 & -0.8489 \\ -0.9998 & 0.0114 & -0.0188 \end{bmatrix}$	$\begin{bmatrix} 49.8693 \\ 49.8564 \\ 3.3872 \end{bmatrix}$	1.80	
(60,30)	1	$\begin{bmatrix} -0.0126 & -0.0166 & -0.9998 \\ -0.0408 & -0.9990 & 0.0171 \\ -0.9991 & 0.0410 & 0.0119 \end{bmatrix}$	$\begin{bmatrix} 59.7021 \\ 29.7944 \\ -3.6419 \end{bmatrix}$	-	
(60,30)	2	$\begin{bmatrix} -0.0086 & 0.8344 & -0.5511 \\ -0.0421 & -0.5509 & -0.8335 \\ -0.9991 & 0.0160 & 0.0398 \end{bmatrix}$	$\begin{bmatrix} 59.7740 \\ 29.7007 \\ -3.6493 \end{bmatrix}$	4.22	14.95
(60,30)	3	$\begin{bmatrix} -0.0091 & -0.8959 & -0.4441 \\ -0.0354 & -0.4436 & 0.8955 \\ -0.9993 & 0.0239 & -0.0276 \end{bmatrix}$	$\begin{bmatrix} 59.8290 \\ 29.9114 \\ -3.6603 \end{bmatrix}$	3.38	

Appendix, Table 2. (*continued*)

Node	Scan	**A**	$\tilde{\mathbf{b}}$	Distance between closest points (cm): Within node	Distance between closest points (cm): Between node
(60,40)	1	$\begin{bmatrix} 0.0192 & -0.4820 & 0.8760 \\ 0.0246 & 0.8761 & 0.4816 \\ -0.9995 & 0.0123 & 0.0286 \end{bmatrix}$	$\begin{bmatrix} 60.0998 \\ 40.1134 \\ -1.0667 \end{bmatrix}$	-	10.56
(60,40)	2	$\begin{bmatrix} 0.0135 & -0.9969 & -0.0777 \\ 0.0222 & -0.0774 & 0.9968 \\ -0.9997 & -0.0152 & 0.0211 \end{bmatrix}$	$\begin{bmatrix} 59.9381 \\ 40.1273 \\ -1.0804 \end{bmatrix}$	4.47	
(60,40)	3	$\begin{bmatrix} 0.0121 & 0.5413 & 0.8407 \\ 0.0138 & 0.8406 & -0.5414 \\ -0.9998 & 0.0182 & 0.0027 \end{bmatrix}$	$\begin{bmatrix} 60.0211 \\ 39.8646 \\ -1.0953 \end{bmatrix}$	6.38	
(60,50)	1	$\begin{bmatrix} 0.0048 & 0.0356 & 0.9994 \\ 0.0290 & 0.9989 & -0.0357 \\ -0.9996 & 0.0292 & 0.0037 \end{bmatrix}$	$\begin{bmatrix} 59.9045 \\ 50.1938 \\ 2.80684 \end{bmatrix}$	-	6.89
(60,50)	2	$\begin{bmatrix} -0.0023 & -0.8161 & 0.5779 \\ 0.0321 & 0.5775 & 0.8157 \\ -0.9995 & 0.0204 & 0.0249 \end{bmatrix}$	$\begin{bmatrix} 59.8833 \\ 50.3410 \\ 2.8340 \end{bmatrix}$	4.88	
(60,50)	3	$\begin{bmatrix} 0.0025 & 0.8791 & 0.4765 \\ 0.0297 & 0.4762 & -0.8788 \\ -0.9996 & 0.0164 & -0.0249 \end{bmatrix}$	$\begin{bmatrix} 59.6986 \\ 50.1437 \\ 2.8313 \end{bmatrix}$	2.60	
(70,30)	1	$\begin{bmatrix} -0.0032 & 0.4589 & -0.8885 \\ -0.0066 & -0.8885 & -0.4588 \\ -1.0000 & 0.0044 & 0.0059 \end{bmatrix}$	$\begin{bmatrix} 69.7213 \\ 30.1121 \\ -2.4162 \end{bmatrix}$	-	13.35
(70,30)	2	$\begin{bmatrix} 0.0064 & 0.8550 & -0.5187 \\ -0.0047 & -0.5186 & -0.8550 \\ -1.0000 & 0.0079 & 0.0007 \end{bmatrix}$	$\begin{bmatrix} 69.8635 \\ 30.1206 \\ -2.3895 \end{bmatrix}$	7.13	
(70,40)	1	$\begin{bmatrix} 0.0207 & 0.9993 & -0.0307 \\ 0.0093 & -0.0309 & -0.9995 \\ -0.9997 & 0.0204 & -0.0100 \end{bmatrix}$	$\begin{bmatrix} 69.9017 \\ 39.8392 \\ -0.6472 \end{bmatrix}$	-	6.41
(70,40)	2	$\begin{bmatrix} 0.0113 & 0.4939 & 0.8694 \\ 0.0531 & 0.8680 & -0.4938 \\ -0.9985 & 0.0517 & -0.0164 \end{bmatrix}$	$\begin{bmatrix} 70.1188 \\ 39.7687 \\ -0.6031 \end{bmatrix}$	14.41	
(70,40)	3	$\begin{bmatrix} 0.0259 & 0.4441 & -0.8956 \\ 0.0078 & -0.8960 & -0.4440 \\ -0.9996 & 0.0045 & -0.0267 \end{bmatrix}$	$\begin{bmatrix} 69.7928 \\ 39.8772 \\ -0.6315 \end{bmatrix}$	4.82	
(70,50)	1	$\begin{bmatrix} 0.0200 & 0.8654 & 0.5007 \\ -0.0178 & 0.5010 & -0.8653 \\ -0.9996 & 0.0084 & 0.0255 \end{bmatrix}$	$\begin{bmatrix} 69.9711 \\ 49.8939 \\ 3.7544 \end{bmatrix}$	-	10.47
(70,50)	2	$\begin{bmatrix} 0.0271 & 0.5752 & 0.8176 \\ -0.0085 & 0.8180 & -0.5752 \\ -0.9996 & 0.0087 & 0.0270 \end{bmatrix}$	$\begin{bmatrix} 70.0671 \\ 49.9266 \\ 3.8105 \end{bmatrix}$	6.30	

Vita

Jason G. Henning was born September 5, 1976 in Norristown, Pennsylvania. In 1994 he received his Bachelor of Science degree in Natural Resource Management from Cook College at Rutgers, The State University of New Jersey, in New Brunswick, New Jersey. He continued his education at the University of Minnesota where he was awarded a Hugo J. and Helen K. Pawek Fellowship. He obtained a Master of Science degree in Forestry from the University of Minnesota in 2002.

With the support of a Cunningham Fellowship he began work towards a Doctor of Philosophy degree in Forestry at Virginia Polytechnic Institute and State University in Blacksburg, Virginia. In support of his research efforts he obtained a Master of Science degree in Statistics in 2003 from Virginia Polytechnic Institute and State University. In 2005 he was awarded the degree of Doctor of Philosophy in Forestry from Virginia Polytechnic Institute and State University. During his graduate education he served as a research assistant and teaching assistant for various undergraduate courses. His interests include applications of ground-based laser scanning, visualization technologies, hybrid modeling approaches and advanced statistical methods in forestry. The author looks forward to continuing a rewarding and fruitful career in forest biometrics research.